Large-scale Atomistic Simulations of Deformation and Fracture Mechanisms of Nanotwinned Metals

by

Xiaoyan Li

B. Eng. Engineering Mechanics, Xi'an Jiaotong University, 2003

B. Sc. Information and Computing Science, Xi'an Jiaotong University, 2003

M. Eng. Engineering Mechanics, Tsinghua University, 2007

D. Eng. Engineering Mechanics, Tsinghua University, 2007

M. Sc. Applied Mathematics, Brown University, 2010

A dissertation submitted in partial fulfillment of the

requirements for the Degree of Doctor of Philosophy

in the School of Engineering at Brown University

Providence, Rhode Island

May 2012

This dissertation by Xiaoyan Li is accepted in its present form by

the School of Engineering as satisfying the dissertation requirement

for the degree of Doctor of Philosophy.

Date_____ _____

Prof. Huajian Gao, Advisor

Recommended to the Graduate Council

Date_____ _____

Prof. Sharvan Kumar, Reader

Date_____ _____

Prof. Allan F. Bower, Reader

Approved by the Graduate Council

Date_____ _____

Prof. Peter M. Weber

Dean of the Graduate School

Vita

Xiaoyan Li was born on October 31, 1980 in Jiexiu, Shanxi Province, China. He attended Xi'an Jiaotong University in 1999, and received the B. Eng. in Engineering Mechanics and the B. Sc. in Information and Computing Science in 2003. Upon graduation, he was enrolled by Tsinghua University with entrance examination waiver. He was awarded the M. Eng and the D. Eng. in Engineering Mechanics in 2007. Subsequently, he entered the Solid Mechanics program at Brown University. He received the M. Sc. in Applied Mathematics on May 2010. His research focused on atomistic simulations for mechanical properties of nanostructured materials.

His scientific publications include,

Xiaoyan Li, Yujie Wei, Wei Yang, and Huajian Gao. Competing grain-boundary and dislocation mediated mechanicsm in plastic strain recovery in nanocrystalline Aluminum. *Proceedings of the National Academy of Sciences of the United States of America*, **106**, 16108-16113 (2009).

Xiaoyan Li, Yujie Wei, Lei Lu, Ke Lu, and Huajian Gao. Dislocation nucleation governed softening and maximum strength in NT metals. *Nature*, **464**, 877-880 (2010).

Sandeep Kumar, Xiaoyan Li, Aman Haque, and Huajian Gao. Is stress concentration relevant for nanocrystalline metals? *Nano Letters*, **11**, 2510-2516 (2011).

Linli Zhu, Haihui Ruan, Xiaoyan Li, Ming Dao, Huajian Gao, and Jian Lu. Modeling grain size dependent optimal twin spacing for achieving ultimate high strength and related high ductility in nanotwinned metals. *Acta Materialia*, **59**, 5544-5557 (2011).

Acknowledgements

First of all, my deepest appreciation goes to my advisor, Prof. Huajian Gao, for his guidance, support, patience and encouragement over the past four years. He is a brilliant scholar and also a wonderful mentor. He led me into the foremost frontier of solid mechanics and material science, and gave me the opportunity to work on some of the most challenging problems in this field. While working with him, I am filled with admiration for his profound knowledge, creative thinking and deep understanding in fields of mechanics, material science, physics and biology. His influence has been beyond science, and will be throughout my career. It is a great honor for me to be one of his PhD students.

All my research works at Brown were motivated by the experimental studies conducted by several collaborators. I have benefited much from helpful discussion and fruitful collaboration with them. I would like to express my great gratitude to Prof. Ke Lu, Prof. Lei Lu and Prof. Yujie Wei (Chinese Academy of Science) for discussions and collaborations on mechanical behaviors of nanotwinned materials, to Prof. Sharvan Kumar and Dr. Seong-Woong Kim (Brown University) for discussions and collaborations on failure mechanisms in nanotwinned thin films, to Prof. Aman Haque and Dr. Sandeep Kumar (Pennsylvania State University) for discussions and collaborations on flaw insensitivity in nanocrystalline materials, and to Prof. Julia Greer and Dr. Dongchan Jang (California Institute of Technology) for discussions and collaborations on deformation mechanisms of nanotwinned nanopillars.

I would like to thank my dissertation committee members, Prof. Sharvan Kumar and Prof. Allan F. Bower for taking the time to read my thesis and give me many valuable suggestions. Prof. Kumar provided a set of amazing and novel experiments which

inspired my research work on deformation and fracture in nanotwinned metal thin films. He was also a member of my preliminary examination committee. I am very grateful to him for his guidance as well as criticisms. I also benefited from the course “Deformation Behaviors of Materials” taught by him. Prof. Allan Bower is one of the most trusted and respected teachers who I have ever met. I learned a lot from his courses, and have applied the knowledge I acquired from these courses in my research. In addition, I would also like to thank Prof. Lambert B. Freund, Prof. Kyung-Suk Kim, Prof. William Curtin, Prof. Vivek B. Shenoy and Prof. Christian Franck for scientific discussions on various problems related to deformation and failure in nanostructured materials.

Whiles staying at Brown, I have made numerous friends. They not only brought me help and fun in life, but also provided support and encouragement for my study. I will never forget their generosity and hospitality.

I would like to acknowledge financial supports from the National Science Foundation through Brown MRSEC program and through grant CMMI-0758535. Moreover, most of the simulations reported in this dissertation were performed on Cray Kraken XT5 in National Institute for Computational Sciences. I also thank National TeraGrid for providing this powerful supercomputing resource to us.

Finally, I would like to thank my family and my fiancée for their love, encouragement and support. Without their understanding and sacrifice, I would never have completed this research. I love all of them forever.

I dedicate this dissertation to my Parents and my Dear Fiancée.

Contents

List of Tables

List of Figures

Chapter 1 Introduction

1.1. Nanocrystalline and nanotwinned metals

Nanocrystalline (NC) materials are defined as polycrystals with grain sizes in the range of 1-100 nm [1]. When the grain sizes are up to 250-1000 nm, the materials are termed as ultra-fine grained (UFG) polycrystalline materials. For the conventional coarse-grained (CG) polycrystalline materials, the grain sizes are usually in the range of 10-300 μm. Structurally, NC and UFG materials are characterized by a large volume fraction of grain boundaries (GBs), which significantly alter their physical, mechanical, and chemical properties in comparison with CG materials [1]. Specially, NC metals exhibit increased strength/hardness, improved toughness, reduced elastic modulus and ductility, and enhanced diffusivity [2]. These unique mechanical properties of NC metals are attributed to their underlying deformation mechanisms, including slip of full dislocations and partial dislocations [4]-[7], deformation twinning [8]-[13], GB sliding and diffusion [14]-[20], and grain rotation [21]. Figure 1.1 shows a deformation-mechanism map of NC face-centered-cubic (fcc) metals. This map captures the transition in both the deformation mechanism and the related mechanical behavior of NC metals with decreasing grain size, as well as its dependence on the stacking fault (SF) energy, the elastic properties of the material, and the applied stress level [3]. The map is divided into three distinct regions. In Region I with characteristic of larger grain size and/or higher SF energy, the complete extended dislocations nucleate from GBs and then travel through the grain interiors, implying that the perfect dislocation (i.e. undissociated

dislocation) slip prevails. In Region II with smaller grain size and/or lower SF energy, the leading partial dislocations nucleate from GBs and are towed by SFs. Consequently, the grains are transected by SFs which inhibit further dislocation propagation, thus leading to strain hardening. The transition between Regions I and II indicates the switching of deformation mechanisms from full dislocation slip to partial slip, which originates from the length-scale competition between the grain size d and the dislocation separation distance r. Region III characterizes the very small grain-size or low-stress regime where dislocation activities are significantly suppressed, and the plastic deformation is governed by GB-mediated processes, including GB sliding and diffusion, grain rotation. In Regions I and II, the yield strength of NC metals increases with decreasing of grain size due to dislocation pile-up at GBs. Such size-strengthening still follows the well-known Hall-Petch law, $\sigma_y=\sigma_0+kd^{-1/2}$, but the slop k is smaller than the conventional value in CG polycrystalline metals. When the grain size is reduced and falls in Region III, the yield strength will drop with decreasing of grain size. Such size-softening is called as “inverse Hall-Petch behavior”, and is attributed to dominance of GB-mediated processes.

It is known that the strength and ductility of materials are often mutually exclusive, i.e. increasing strength sacrifices the ductility, and vice versa. Because of high strength but poor ductility of NC and UFG metals, in recent years much attention has been paid to developing strategies for simultaneously improving the strength and ductility of UFG and NC materials [2],[22]. So far, materials scientists have proposed several approaches, such as bimodal (or multimodal) grain-size distribution [23],[24], second-phase particle hardening [25]-[27] and introducing nanoscale twins [22],[28],[29]. Remarkably, when the nanoscale twin lamellas are introduced in polycrystalline materials, a high density of

twin boundaries (TBs) is embedded in the grain interiors. These TBs act as coherent internal boundaries which not only enhance mechanical properties but also alter physical properties of materials. Thus, a new kind of hierarchical nanostructured materials – nanotwinned (NT) materials – have been produced by introducing the nanoscale twins.

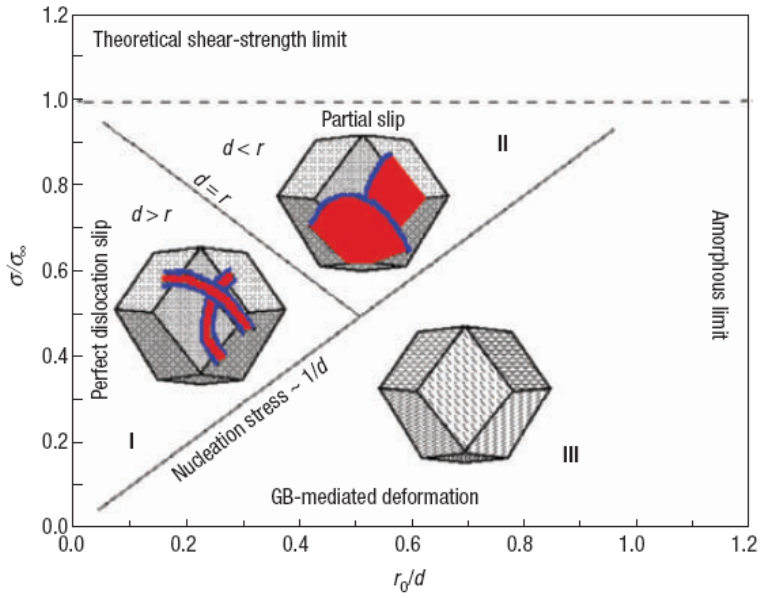

Figure 1.1. Deformation-mechanism map incorporating the role of the SF energy in the deformation behavior [3]. Here σ is the resolved shear stress and d is the mean grain size. r is the dislocation splitting distance, and depends on the parameters σ_∞ and r_0, which are functions of the SF energy, the elastic moduli and the Burgers vector of Shockley partial dislocation.

During the last five years, NT materials have attracted global intense interests from mechanics, materials science and physics communities, owing to their unique microstructures and enhanced mechanical/physical properties. NT materials are characterized with a large number of coherent and nanometer spaced TBs embedded in micron or sub-micron sized grains. Experimental studies have shown that NT metals possess ultra-high strength [28]-[30] and hardness [31]-[33] as well as good tensile ductility [29],[34],[35] and strain hardening [29],[34],[36]. NT bulk metals exhibit

electrical conductivity comparable to that of their conventional CG counterpart but much higher than that of NC metals [28]. Nanotwins cause substantial changes in electronic and optical properties of semi-conductor nanowires [37]-[40]. These properties of NT materials are suggesting promising applications in microelectromechanical systems, micro-/nano-devices, quantum optics, biological sensing and high-performance structural applications.

1.2. Motivation

The NT metals have exhibited an inherent structural hierarchy: a high density of nanoscale twins are incorporated into submicrometer-sized grains, and act as a sub-structure that refines the grain interior. In NT metals, TBs not only blocks dislocation motion, but also sustain large plastic deformation through interfacial migration. Meanwhile, as a second-level structure, the refining twins can store plenty of dislocations, and confine dislocation segment length, which affects the capability of efficient dislocation storage in the first-level structure. Therefore, instead of the traditional strength-ductility trade-off, a “win-win” in strength and ductility can be achieved in NT metals. Moreover, NT metals have been reported to possess enhanced mechanical properties, such as work hardening, strain rate sensitivity, fracture toughness and fatigue resistance, and thereby show great potential for structural applications in nanoscale devices with extraordinary functions, performance and capabilities. However, the current lack of understanding of the underlying mechanisms that control the properties of NT metals, partly because more than one characteristic microstructure is involved in these materials, severely limits our ability to utilize them in nanoscale systems with tailored properties.

Over the past few years, the vast majority of experimental, theoretical and computational studies have been conducted on the underlying deformation mechanisms that govern the mechanical responses of NT metals. However, there are a lot of issues related to deformation and failure of NT metals, which still remain unclear and even mysterious. From the perspectives of both scientific curiosity and technological promises, it has become increasingly important and necessary to develop an in-depth understanding of how the intrinsic microstructure of NT metals (e.g. the sub-grain twin structures) influences their mechanical behaviors and deformation mechanisms.

In this dissertation, we systematically investigate the size dependence of mechanical properties of NT metals, in various forms (bulk, thin films and nanopillars). We try to reveal the underlying microscopic deformation mechanisms responsible for the unique mechanical properties of NT metals, by applying molecular dynamics (MD) simulations with atomic-level spatial and temporal resolution. The research work aims to explore the relationship between microstructure and deformation behaviors of NT metals.

1.3. Outline of the dissertation

In this dissertation, our objective is to investigate the mechanical behaviors of NT fcc metals using atomistic simulations. This dissertation consists of seven chapters and is organized as follows.

Chapter 1 is an overview introduction about NC and NT metals. The motivation and goal of our research are also presented.

In Chapter 2, we review some of the recent studies aimed to elucidate the mechanistic origin of the superior mechanical properties of NT metals, in various forms such as equiaxed- or columnar- grained bulk samples, thin films, nanowires and nanopillars. The

intrinsic microstructures and underlying deformation mechanisms which govern the mechanical responses of NT metals are summarized, with emphasis on the intricate interplay between dislocations and TBs and the size effects associated with TB spacing.

Chapter 3 presents the methodology in MD simulations. We introduce the interatomic potentials, ensembles, integration and parallel computing algorithms, loading method, stress computation and visualization techniques commonly used in MD simulations. Advantage and limitations of MD simulation are addressed. High performance computing and the relevant application associated with supercomputers are briefly introduced.

In Chapter 4, we apply large-scale MD simulations to study the twin size effect on yield strength of two kinds of NT bulk Cu: one is the equiaxed-grained material, and another is the columnar-grained material. For the equiaxed-grained NT Cu, we focus on the microscopic mechanisms behind size-softening. For the columnar-grained NT Cu, the influence of TB orientation (with respect to loading direction) on deformation behaviors is our main concern.

In Chapter 5, we introduce results of in-situ tensile experiments in the transmission electron microscope (TEM) on UFG free-standing Cu thin films containing nanoscale twins. Secondly, we perform MD simulation to complement the experiments and provide atomistic insights to experimental observations. In this chapter, we focus on the fracture mode and the relevant mechanisms in NT Cu thin films.

In Chapter 6, in-situ tension experiments on NT Cu nanopillars with orthogonal and slanted TBs are firstly introduced. Subsequently, MD simulations are performed on the samples with the same diameter and TB orientation as those used in the experiments. Linking the experimental observations and simulation results, we make an attempt to

capture the distinct deformation mechanisms from difference in TB orientation and reveal the role of TB orientation in plasticity of NT metallic nanopillars.

Chapter 7 concludes the entire dissertation with major scientific findings and future directions of the study.

Chapter 2 Mechanics of Nanotwinned Metals

2.1. Fundamental concepts

In this section, we will address two fundamental concepts in fcc metals: one is TB, and another is deformation twinning and its opposite process -- detwinning.

2.1.1. Twin boundary

TB is a special type of GB, and is a highly symmetrical interface. The domains on both sides of TB are called as “twin” and “matrix”. The lattice structures in both domains keep high symmetry with respect to TB. Relative to general GB, the coherent TB has ordered structure and low interfacial energy. The second column of Table 2.1 lists TB energies of some selected metals which have been produced as NT counterparts.

Table 2.1. TB and SF energies of selected metals and alloys

Materials	γ_{TB} (mJ/m^2)	γ_{SF} (mJ/m^2)
Ag	8	16
Au	15	32
Cu	24	45
Ni	43	125
Al	75	166
Pd	97	180
CuAl	5-20	7-41
TiAl	<60	67-97

Crystallographically, TB in fcc is described as one of Σ3 coincidence-site-lattice boundaries with a <011> misorientation axis, which belongs to a group of tilt GBs. For fcc metals, a Σ3 GB can be obtained by rotating one monocrystal (the matrix domain) with respect to another (the twin domain) by an angle of 70.53° around a <011> axis [41]. The geometry of Σ3 GB is characterized by a number of mutually perpendicular low

index lattice planes for both neighboring grains: {111}, {112} and {011} [41]. As depicted in Fig. 2.1, a CTB is parallel to a {111} plane; a symmetrical incoherent TB (SITB) is perpendicular to a {111} plane but parallel to a {112} plane; between CTB and SITB are asymmetrical GBs (AGB) that can be identified by the inclination angle of the GB plane with respect to {111}. Figure 2.2 shows the atomic configuration of a CTB in fcc metals. It can be seen that CTB is a highly symmetrical interface separating matrix and twin domains, so that atoms on both sides of the CTB are in perfect mirror symmetry. More details about the geometries of TBs in fcc, body-centered-cubic (bcc), and hexagonal-close-packed (hcp) metals can be found in the literature [8].

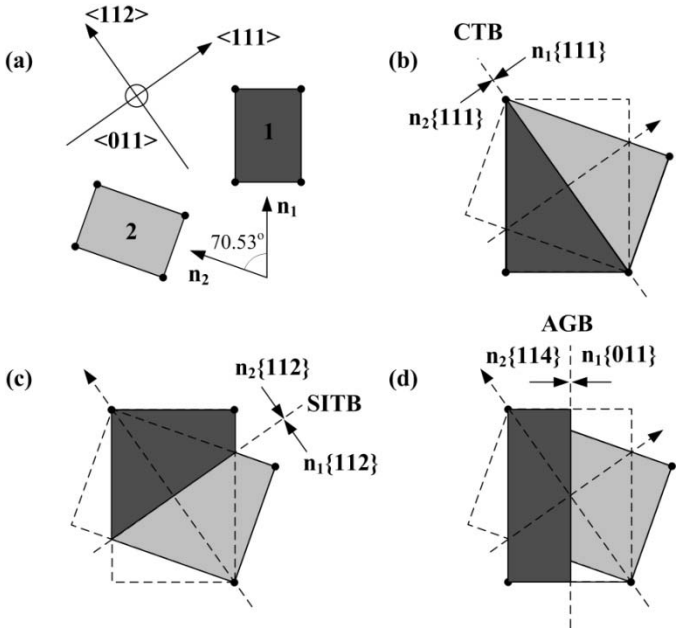

Figure 2.1. Geometry of bicrystals with a Σ3<011> GB [41]. (a) Σ3 misorientation for fcc elementary cells 1 and 2. (b) CTB. (c) SITB. (d) AGB with an inclination angle of 35.26°.

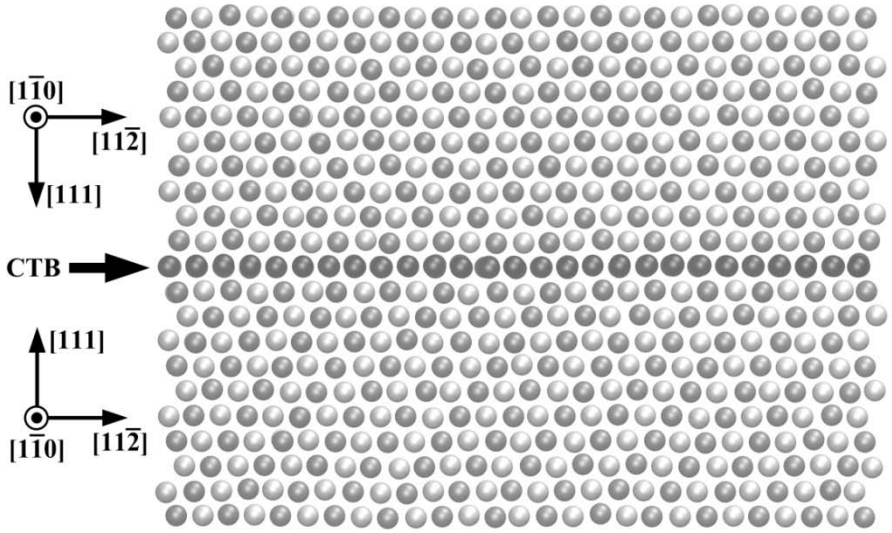

Figure 2.2. Illustration of a CTB in fcc metals. White and grey atoms are on adjacent {110} planes, respectively.

A special twin structure, the fivefold twin, has also been found in small particles/clusters and thin films [42], and has been recently observed in NC fcc metals and alloys [43]-[47]. The fivefold twin structure consists of five tetrahedral subunits joined together on adjacent bounding faces, all of which are CTBs. Recent experimental observations [46] and atomistic simulations [48],[49], have revealed that the fivefold twin might have originated from sequential twinning involving multiple emissions of partial dislocations from GBs. Figure 2.3 shows a typical TEM image of five-fold twin in NC Cu.

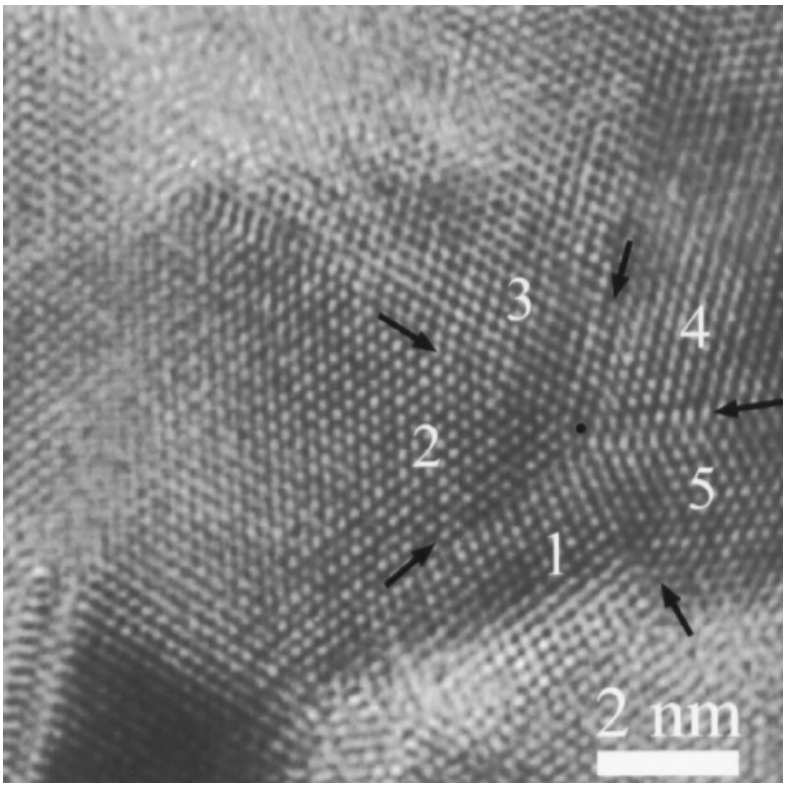

Figure 2.3. A typical image of a fivefold twin [44]. The TBs are indicated by black arrows, and each twin domain is marked with 1 to 5, respectively. The twin center is highlighted with a black dot.

2.1.2. Deformation twinning and detwinning

Deformation twinning is an important plastic deformation mechanism in metals and alloys, and it can sufficiently carry the shear strain, especially at low temperature and high strain rate. Conventionally, deformation twinning in fcc metals is caused by successive gliding of Shockley partial dislocations on the slip plane. These partials are called as “twinning dislocations (TD)”. The twinning tendency of an fcc metal is mainly determined by its SF energy (see Table 2.1), i.e. deformation twinning easily occurs in fcc metals with low SF energies. Studies about deformation twinning in various metals and alloys have been well documented in two important review articles [8],[13].

It is known that for CG metals and alloys, smaller grain size impedes deformation twinning, irrespective of their crystal structure [13]. However, when the grain size of polycrystalline metals is refined to nanometer regions, deformation twinning has been frequently observed even in materials with medium to high SF energies such as Cu and Ni [13]. Recent experimental observations on NC Ni [50] and Cu [51],[52] showed an "inverse grain-size effect", i.e., twinning propensity decreases as grain size reduces. These grain-size effects in CG and NC metals are still not understood, and the investigation to their physical nature is an ongoing issue. But it is recognized now that twinning is one of the major plastic deformation mechanisms in NC materials [13]. So far, five mechanisms related to formation of deformation twins have been found in NC metals [13]: (1) emission of successive partial dislocations from GBs; (2) dynamic overlapping of SF ribbons; (3) splitting and migration of GB; (4) sequential twinning; and (5) dislocation rebound. The first three can generate single twin, while the last two can produce multiple-fold twin.

Detwinning is an opposite process to twinning. Recently, such process was often observed during plastic deformation of NT metals. Generally, detwinning is due to the successive slip of partial dislocations on pre-existing TB, and it leads to TB migration and further narrowing of twin, and even disappearance of twin. Recent in-situ nanoindentation of epitaxial NT Cu film with columnar grains [53] revealed that the detwinning process can be accomplished via the collective glide of multiple twinning dislocations that form an incoherent TB (ITB). The relevant process is illustrated in Fig. 2.4. It was also found in this study that detwinning can easily occur for thin twins, and the driving force is mainly attributed to variation of the excess energy of a CTB, and the

migration velocity depends on SF energy [53]. These findings imply that detwinning becomes dominant during plastic deformation of metals with growth twins of the order of a few nanometers thick [53].

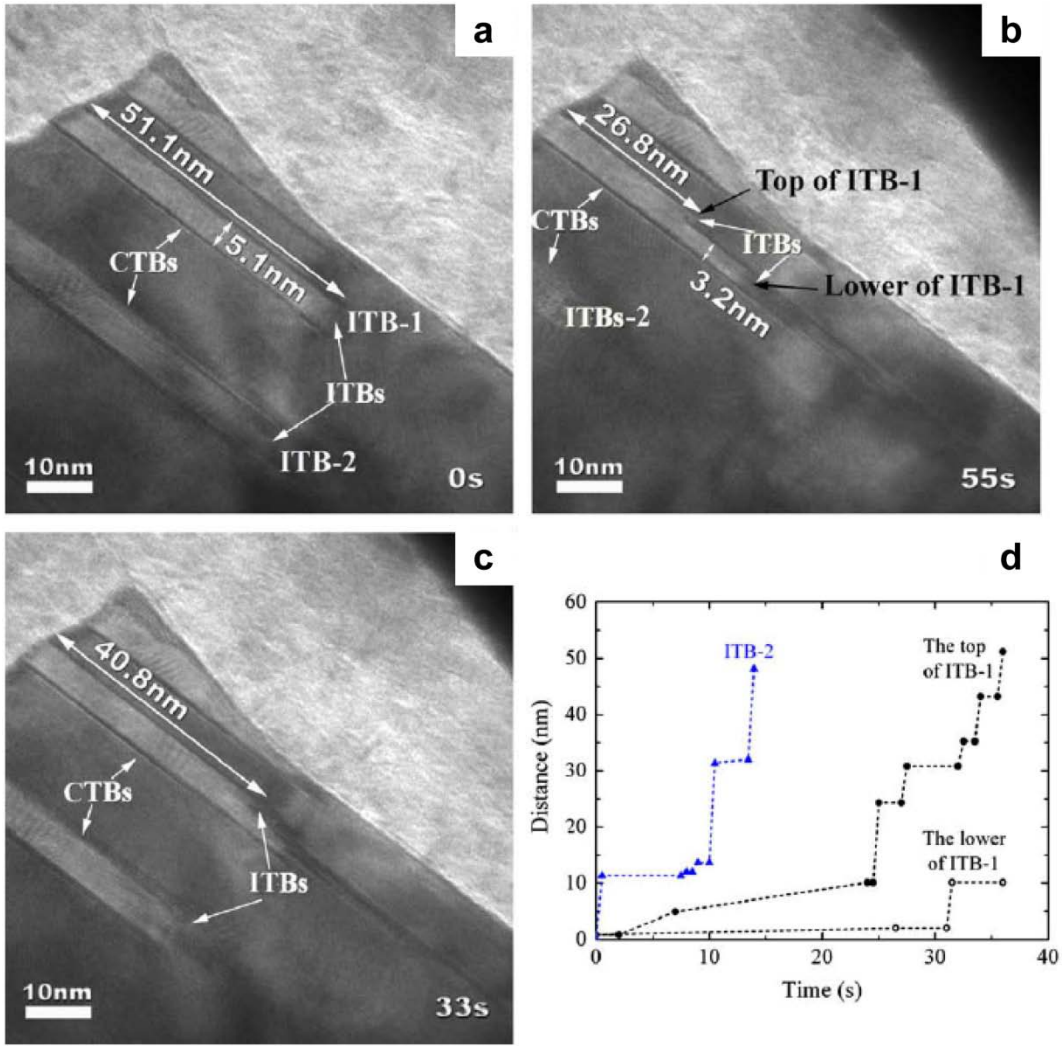

Figure 2.4. Detwinning process observed in nanoindentation of epitaxial NT Cu film with columnar grains [53].Three snapshots of in situ TEM micrographs of Σ3 {112} ITBs before indentation (a), at 33 s (b) and at 55 s (c). (d) The migration distance as a function of time. The time in (d) is relative to 28.5 s at which the migration is clearly observed.

2.2. Synthesis of nanotwinned metals

In the mid-1970s, Mertz et al. [54],[55] fabricated fine-grained Cu and Ni foils via sputter deposition and introduced a high density of twins inside columnar grains; however, the TB spacing in such specimens is randomly distributed. During the last decade, Lu et al. [28],[29] were able to synthesize UFG Cu samples with sub-grain twin lamellae by means of electro-deposition, with TB spacing controlled down to tens of nanometers by changing deposition rates. Zhang and coworker [31]-[33] produced epitaxial NT Cu and Ag thin films with thickness on the order of ~1 micron using sputter deposition. Idrissi et al. [36] synthesized NT Pd ultrathin and ultrafine films via chemical evaporation at high temperature, with thicknesses ranging from 80 nm to 200 nm, and average grain size around 30 nm. More recently, a variety of NT metallic nanowires (such as Ag [56], Au [57], and Cu [58]) have been successfully produced by electro-deposition or electro-chemical synthesis. In these NT nanowires, highly dense twins normal to the growth axis were introduced with TB spacing as small as 10 nm and even less. Progress has also been made on the fabrication of NT metallic nanopillars. Greer et al. [59],[60] achieved the synthesis of NT Cu nanopillars by precisely controlling the conditions under which Cu is electroplated into patterned polymethylmethacrylate templates. The diameters of these NT pillars range from 50 nm to 500 nm, with TB spacing below 5 nm. Remarkably, they could also control the orientation of TBs to create single-crystalline nanopillars with TBs inclined to the growth direction.

Currently, most twinned materials have been synthesized via the formation of growth twins. A recent study showed that twinned CuAl alloys can be produced by annealing commercial alloys [61]. It was observed that a large number of micron sized twins were

formed during the annealing process and the fraction of annealing twins increased as the Al content rises. It has also been reported that nanoscale twin/matrix lamellae could be introduced via dynamic plastic deformation (DPD) into Cu-4.5 wt% Al alloys with an average grain size of about 200 μm [62]. In the course of DPD treatment, deformation twinning occurred at strain levels ~0.15 within many grains with preferred orientations. The formation of annealing and deformation twins is due to very low TB and SF energies of CuAl alloys (see Table 2.1), which has resulted in a dependence of annealing twins on the Al content. To date, NT metals and alloys have been synthesized in the manner of growth, deformation and annealing twinning.

2.3. Microstructures of nanotwinned metals

2.3.1. Microstructures of nanotwinned bulk metals

The polycrystalline NT fcc metals exhibit an inherent structural hierarchy: a high density of nanoscale twins are embedded in micron- or submicron-sized grains and act as a sub-structure that refines the grain interior. Such hierarchical structures play an important role in determining properties and functions of NT metals. TBs not only obstruct the motion of dislocations but can also accommodate large plastic deformation via interfacial migration. Meanwhile, as a second-level structure, the refining twins can store plenty of dislocations and confine the length of dislocation segments, which substantially affects the capability of efficient dislocation storage in the first-level structure.

Due to various differences in synthesis methods, there have been two distinct grain structures in NT metals: one is the equiaxed-grained structure where TBs are inclined to

GBs, while another is the columnar grained structure where TBs are nearly perpendicular to GBs along the columnar axis, as shown in the TEM images in Figs. 2.5a and 2.5b, respectively. In NT metals with equiaxed grains, most GBs are of a high-angle type with mixed features of tilting and twisting. In NT metals with columnar grains, the GBs are primarily of the twisting type. It can be expected that these different microstructures would have significant effects on their respective mechanical behaviors.

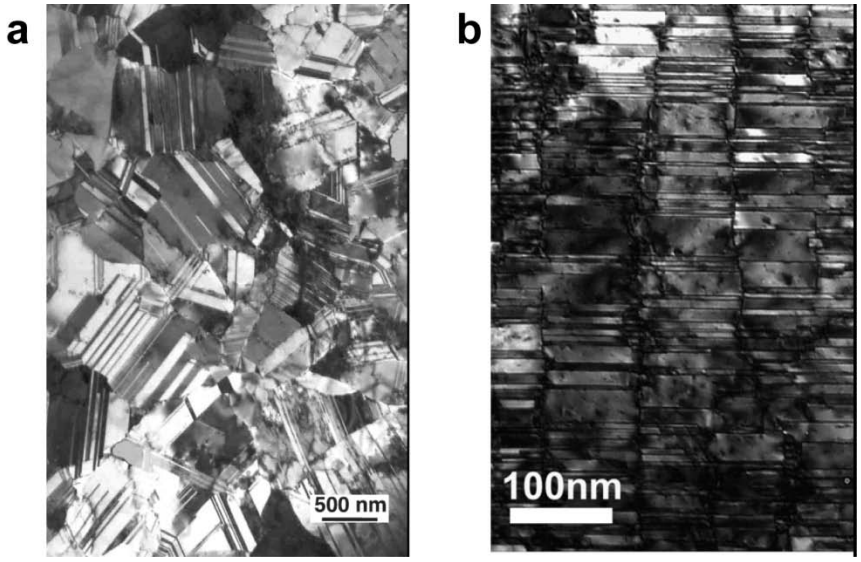

Figure 2.5. Microstructures of NT metals. (a) A bright-field TEM image of NT bulk Cu with equiaxed grains [28]. (b) Cross-section TEM image of NT Ag film with columnar grains [33].

2.3.2. Microstructures of nanotwinned nanowires and nanopillars

In NT metallic nanowires, TBs still remain normal to the <111>-oriented growth direction, like NT semiconductor nanowires. However, it appears that there are no ordered micro-facets on free surfaces of NT metallic nanowires, presumably because these free surfaces have developed oxide layers during/after synthesis/processing. It was recently found that the regular arrangement of TBs can significantly improve the mechanical strength of NT metallic nanowires without altering their electrical properties

[57],[58]. NT metallic nanowires are of great interest for applications in micro- and nano-electromechanical systems where excellent mechanical and electrical properties are simultaneously required.

2.4. Mechanical properties of nanotwinned metals

2.4.1. Yield strength

Mechanical properties of NT metals have been characterized by uniaxial tension/compression tests and micro- or nano-indentation. Most existing data were obtained for fcc metals (e.g. Cu, Au, Ag, Ni and Pd). It has been found experimentally that the yield strength of NT metals depends strongly on the intrinsic and extrinsic length-scales of the material. For NT polycrystals, the yield strength depends on two characteristic size scales, i.e. TB spacing and grain size. For NT single crystals, the sample dimension (e.g. diameter of nanowires/nanopillars) and TB spacing become two crucial factors to determine the strength. Figures 2.6a and 2.6b show the typical stress-strain curves from a bulk sample of NT Cu under uniaxial tension [1] and NT Cu nanopillars under uniaxial compression [60], respectively. NT metals exhibit higher yield strength than their TB-free counterparts. As shown in Fig. 2.6a, the strength of NT Cu bulk samples can reach 1 GPa, which is more than double that of the NC Cu and one order of magnitude higher than that of CG Cu samples. Recent experiments [60] also reported that the compressive strength of NT Cu pillars with diameter of 500 nm can reach three times that of single-crystalline pillars with the same diameter.

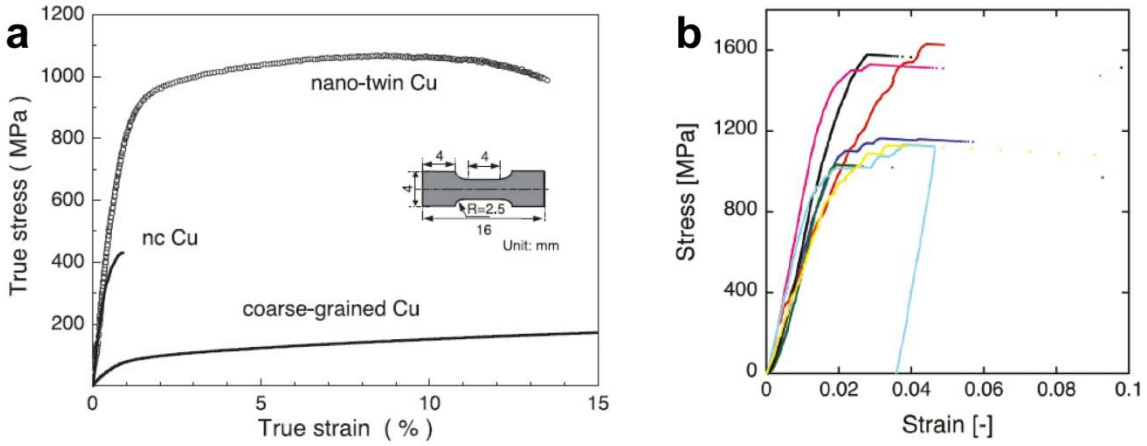

Figure 2.6. Stress-strain curves of NT metals. (a) A typical tensile stress-strain curve for as-deposited NT Cu (with average grain size d of 500 nm and TB spacing λ of 15nm) in comparison with that for a CG polycrystalline Cu (d>100 μm) and NC Cu (d~30 nm) [28]. (b) Selected true stress-strain curves for NT Cu nanopillars [60] (with diameter of 500 nm and TB spacing λ of 8.8 nm). Different curves represent fluctuations among different tests on similar samples.

For NT polycrystalline metals with TB spacing beyond a critical value, the yield strength increases as the TB spacing decrease, following the well-known Hall-Petch relation

$$\sigma_y = \sigma_0 + k\lambda^{-1/2} \tag{2.1}$$

where σ_y is the yield strength, λ is the TB spacing or twin thickness, k is a material constant, and σ_0 is a friction stress. The data from experimental studies on twin size dependence of yield strength in NT Cu polycrystals, as summarized in Fig. 2.7a, agree well with the Hall-Petch law. Notably, two sets of data were obtained from nano-indentations of NT Cu thin films with columnar grains [31],[32], with yield strength taken to be approximately one-third of the hardness. The strengthening behavior

indicated in Fig. 2.7a provides a strong evidence of TBs blocking dislocation motion, as will be discussed again in Chapter 4.

So far, there are no systematical experimental studies on the effects of twin size on the strength of NT metallic nanowires and nanopillars, partly because of the technical difficulties in processing NT low-dimensional metals and manipulating them in tensile or compressive tests. A number of MD simulations [63]-[74] have been performed to investigate twin size effects in metallic nanowires and nanopillars with TBs perpendicular to the growth axis. Figure 2.7b shows some recent data from MD simulations of NT Au nanowires and nanopillars. There is a clear increase in the yield strength of NT single crystals as the TB spacing is reduced. However, such strengthening does not follow the conventional Hall-Petch relation with one length variable, in that the strength here relies also on the extrinsic dimension, i.e. the sample diameter. MD simulations revealed that the strengthening in NT nanowires arises from complicated interactions between dislocations and TBs. Deng and Sansoz [68] found that the yield strength of NT Au nanowires and nanopillars is proportional to the inverse of the TB spacing, i.e.

$$\sigma_y = \sigma_0 + f(d)/\lambda \tag{2.2}$$

as shown in Fig. 2.7b. In Eq. (2), σ_0 represent the yield strength in the absence of TBs, and $f(d)$ is a function of sample diameter d. This function represents the constraint of sample dimension on the curved dislocation loops emitted from free surfaces [68].

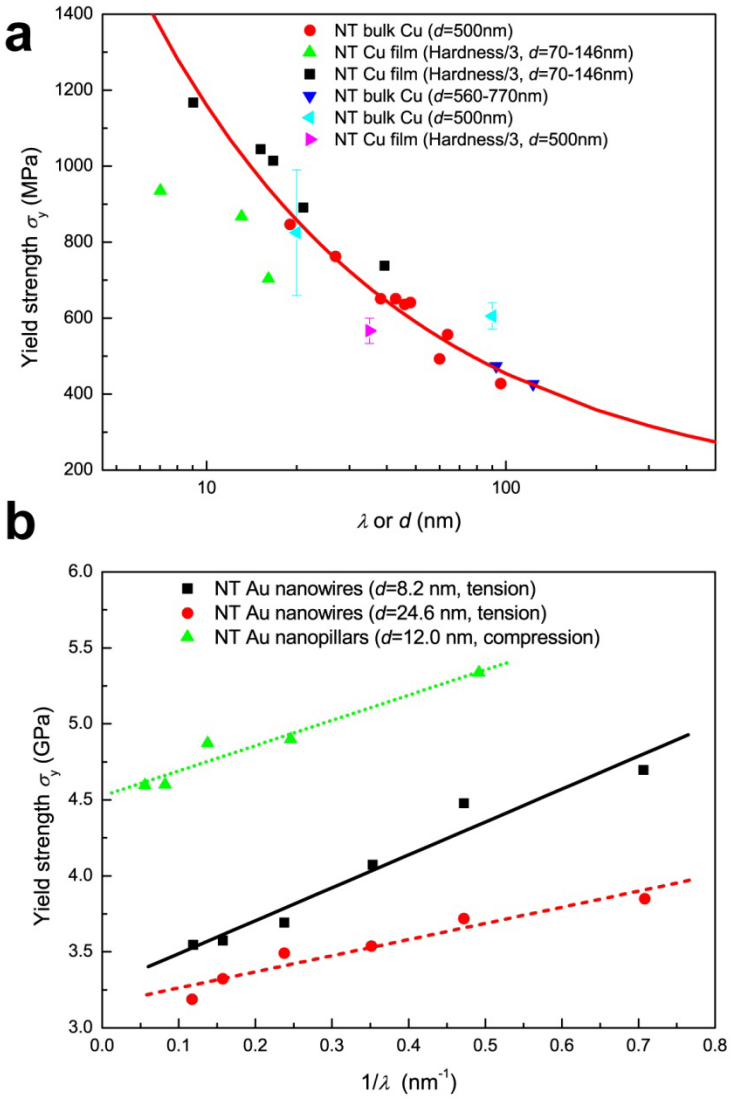

Figure 2.7. Yield strength of NT metals as a function of TB spacing. (a) Yield strength of NT polycrystalline Cu. Data are from experiments (uniaxial tension [29],[54],[55] or nanoindentation [31],[32]). Solid line represents the Hall-Petch relation. (b) Yield strength of NT Au nanowires and nanopillars. Data are from CMD simulations of NT Au nanowires [65] and nanopillars [73] where TBs are normal to the growth direction.

When the TB spacing falls below a critical value, the yield strength of NT metals decreases as the TB spacing is further reduced, reminiscent of the (somewhat controversial) “inverse Hall-Petch effect” in NC metals. Such softening phenomenon was

observed for the first time during uniaxial tensile testing [29] of NT Cu with equiaxed grains, and subsequently in MD simulations of equiaxed-grained NT Cu [75] and Pd [76]. To account for the observed strength softening, there have been extensive experimental, theoretical and computational studies showing that the softening is induced by TBs migration via easy-slip of twinning partial dislocations along the TBs, resulting in narrowing of twin domains. We will address this softening issue in details in Chapter 4.

2.4.2. Ductility

Ductility is usually defined as the limit of strain for a material to sustain homogenous plastic deformation before localized deformation occurs in the form of shear banding or necking. Recent decades have witnessed numerous UFG and NC metals with ultrahigh strengths. However, as the grain size is reduced to sub-micron and nanometer ranges, the achieved ultrahigh strength is typically accompanied by a great reduction in ductility compared to the conventional CG metals. A survey of published papers indicated that most NC metals exhibit a tensile elongation to failure below ~10% [77]. Early studies attributed the limited ductility of NC metals to some kind of flaws from processing and tensile instability [1].

Recent advancements of NT metals [28],[29],[34] demonstrated that the introduction of a high density of nanoscale twins into UFG metals not only leads to substantial improvements in yield strength, but also imparts good ductility. An early study [34] reported that NT Cu with average grain size 200-300 nm has an elongation to failure ~30% at 77 K, which is close to the tensile ductility (40%-60%) of CG Cu. More recent investigations [29] of NT Cu with mean grain size ~500 nm showed a pronounced rise in tensile ductility with decreasing TB spacing at room temperature, in contrast to the

reduced ductility with grain refinement in NC metals, as illustrated in Fig. 2.8. In NC metals, dislocations are nucleated from GBs and travel through the small grains to sustain plastic flow, but they can be quickly absorbed by the opposite GBs, which lower the dislocation density and prevent the accumulation of large strains. In the absence of very active GB-mediated deformation mechanisms, the ductility of NC metals would decrease as the grain size is reduced. In NT metals, in contrast, the nanoscale twin lamellae provide ample room for dislocation nucleation and storage to sustain large plastic strains during deformation, resulting in a continuous rise in ductility with narrowing twins.

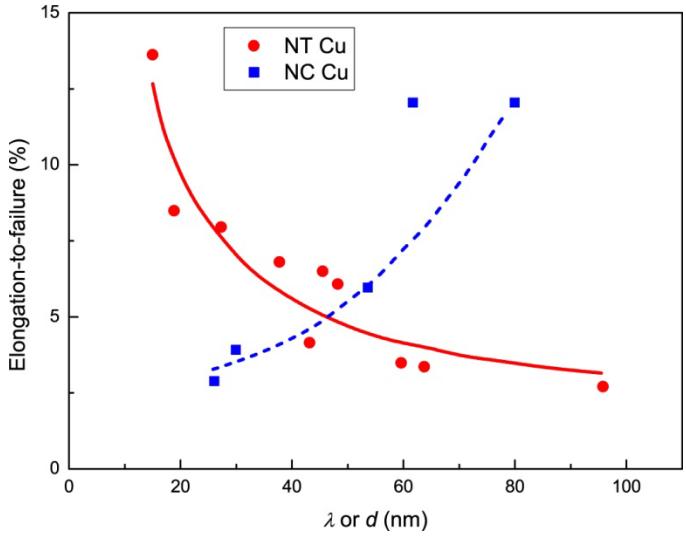

Figure 2.8. Elongation-to-failure as a function of mean TB spacing for NT Cu with average grain size of 500 nm, in comparison with the grain size dependence of Elongation-to-failure for NC Cu. The solid and dashed lines serve only as visual guides. Figure replotted from [22].

2.4.3. Strain hardening

For metals undergoing homogeneous plastic deformation, usually the stress-strain behavior can be approximated as a power law,

$$\sigma = K_1 + K_2 \varepsilon^n \tag{2.3}$$

where K_1 represents the initial yield stress, K_2 is the strengthening coefficient, and the exponent n characterizes work hardening. Most CG metals have n value between 0.1 and 0.5. Figure 2.9 shows a comparison of size effects on the strain hardening exponent n between NT Cu and its twin-free counterparts [29]. As the grain size decreases, the strain hardening coefficient of regular Cu decreases, especially for NC metals, until it becomes nearly undetectable when the grain size goes down to tens of nanometers. However, for NT bulk Cu, the strain hardening monotonically increases with the reduction in TB spacing. The low strain hardening behavior of NC metals can be attributed to the saturation of effective dislocation density during plastic deformation, which is caused by dynamic recovery or dislocation annihilation in small grains [1]. While the detailed mechanism of strain hardening in NT metals is still being debated, it may be attributed to the extraordinary ability of CTBs to store high density of geometrically necessary dislocations during deformation.

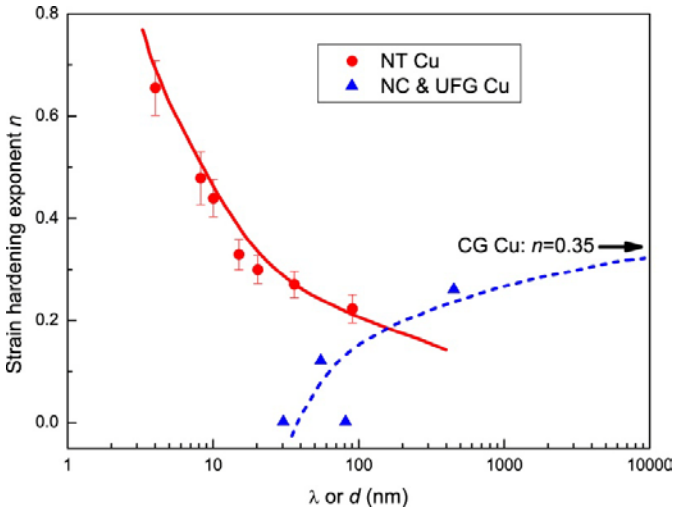

Figure 2.9. Strain hardening exponent n as a function of mean TB spacing for NT Cu with average grain size of 500 nm, in comparison with the grain size dependence of strain hardening exponent of UFG and NC Cu. The solid and dashed lines serve only as visual guides. Figure replotted from [29].

2.4.4. Strain-rate sensitivity

It is well known that the mechanical responses of metals can strongly depend on the applied strain rate. The strain-rate sensitivity is usually characterized by a non-dimensional exponent *m* defined as

$$m = \frac{1}{\sigma}\frac{\partial \sigma}{\partial \ln \dot{\varepsilon}} \tag{2.4}$$

where σ is the flow/yield stress and $\dot{\varepsilon}$ is the strain rate. For ductile metals under uniaxial tension or compression, the strain-rate sensitivity can also be related to the so-called activation volume *V* [78]

$$V = \sqrt{3} k_B T \frac{\partial \ln \dot{\varepsilon}}{\partial \sigma} \tag{2.5}$$

where k_B is the Boltzmann constant and *T* is the absolute temperature. The activation volume represents the rate of decrease of the activation enthalpy with respect to flow stress at constant temperature [78]. Combining Eqs. (2.4) and (2.5) indicates

$$m = \frac{\sqrt{3} k_B T}{\sigma V} \tag{2.6}$$

The strain-rate sensitivity index *m* and the activation volume *V* are often used to evaluate the sensitivity of flow stress to loading rate and to probe/identify the active deformation mechanisms. Typical values of *m* and *V* for CG, NC and NT bulk Cu are summarized in Table 2.2. Figure 2.10 shows a comparison of strain-rate sensitivity between NC and NT bulk Cu [79]. When the average grain size is fixed, NT bulk Cu has higher strain-rate sensitivity in comparison with its twin-free counterpart. Recently, a systematical investigation [78] of rate sensitivity of NT bulk Cu via nano-indentation revealed that the

interaction between CTBs and dislocation is responsible for elevated strain-rate sensitivity of NT bulk Cu.

Table 2.2. Typical values of *m* and *V* for CG, NC and NT bulk Cu (*b* is the magnitude of Burgers vector of dislocation)

Material	Strain-rate sensitivity *m*	Activation volume *V*
CG Cu (forest hardening, *d*>1000nm)	0-0.007	100-1000 b^3 [1]
NC Cu (*d*>10nm)	0.025-0.06 [1]	10-200 b^3
Creep tests for NC Cu (GB-diffusion-mediated process)	0.5-1	1-10 b^3 [1]
NT Cu (*d*=500nm)	0.025-0.036 [78]	12-22 b^3 [78]

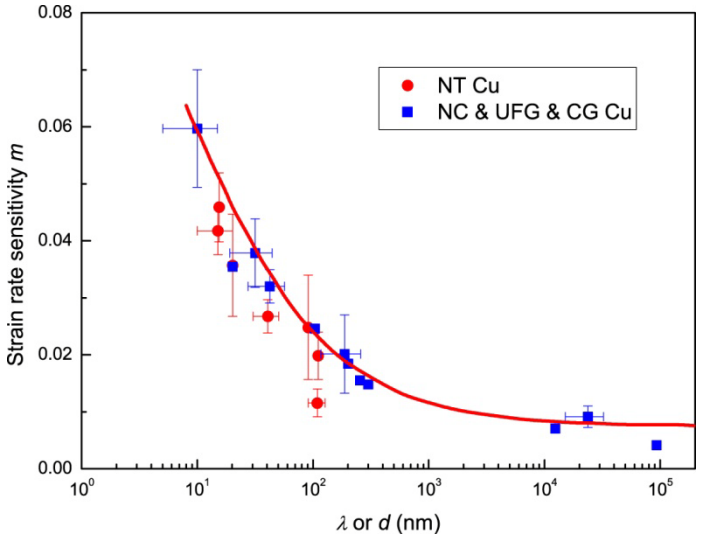

Figure 2.10. Strain rate sensitivity as a function of TB spacing for NT Cu, in comparison with that of polycrystalline Cu as a function of grain size. The solid line serves as a visual guide. Figure replotted from [79].

2.4.5. Fracture toughness and fatigue properties

To date, there have been only a few reports on the fracture and fatigue properties of NT metals. Qin et al. [80],[81] measured the fracture toughness of NT bulk Cu processed by DPD using three-point bending tests. They found that the fracture toughness increased with increases in volume fraction of nanoscale twins, and that NT samples exhibit

dimpled fracture surfaces. It was also shown that the size and shape of dimples are closely correlated with the fraction of nanoscale twins. These phenomena may be attributed to the structural anisotropy of nanoscale deformation twins that are very slender in shape. The twin lamellar structures were found to be effective in energy absorption and arresting crack propagation during fracture [81]. Singh et al. [82] performed tensile fatigue tests on pre-cracked NT bulk Cu prepared by electrodeposition, and determined fracture toughness using load-displacement curves. It was concluded that decreasing TB spacing (i.e. increasing volume fraction of twins) leads to improved fracture toughness. Table 2.3 summarized the fracture toughness of NT, UFG and CG bulk Cu measured in recent experiments.

Table 2.3. Fracture toughness of NT, UFG and CG bulk Cu

Specimen	**Mean grain size d (nm)**	**Mean TB spacing λ (nm)**	**Fracture toughness K_{IC} (MPa·m$^{1/2}$)**	**Test method**
NT Cu	-	47	17.0	3 point bending [81]
NT Cu	60	49	24.4	3 point bending [81]
NT Cu	55	46	27.3	3 point bending [81]
CG Cu	-	-	9.4	3 point bending [81]
NT Cu	450	85	17.5	fatigue tension [82]
NT Cu	450	32	22.3	fatigue tension [82]
UFG Cu	450	-	14.9	fatigue tension [82]

Shute et al. [83] examined the effects of 35 nm-thick twins on fatigue crack growth under cyclic loading in columnar-grained NT bulk Cu processed by magnetron sputter deposition. They compared the S-N curves (stress amplitude versus cycles-to-failure) of NT Cu with those of UFG and CG Cu (see Fig. 2.11a). It can be seen that both NT and UFG Cu showed a markedly improved fatigue life compared to CG Cu, even in the high-cycle regime. However, it was quite unexpected that the S-N curves for NT Cu is quite similar to those of UFG Cu, as these two materials have drastically different

microstructures and characteristic features on fracture surfaces. They argued that this similarity might be a coincidence, the interpretation being that cracks in both materials initiated from the intersections of certain soft domains with surfaces [83]. Dao and coworkers [82] investigated the fatigue properties of NT and UFG bulk Cu with equiaxed grains (with mean grain size of ~450 nm) synthesized via pulsed electrodeposition, and provided a quantitative comparison of fatigue crack growth rate log(d*a*/d*N*) versus logΔK, as shown in Fig. 2.11b. It was found that the higher the twin density, the smaller the fracture crack growth rate at any given value of ΔK. This result is at variance with that obtained by Shute et al, which might be due to microstructural differences (such as grain configuration and GB misorientation) of the specimen from different processing methods. This issue needs to be further clarified in order to facilitate the design of optimum microstructures of NT metals with enhanced fatigue properties.

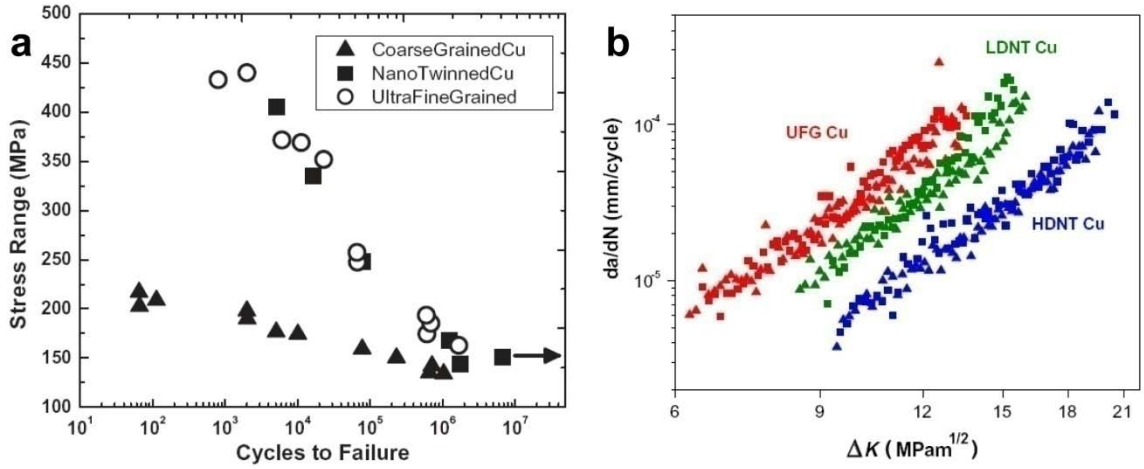

Figure 2.11. Fatigue properties of NT Cu. (a) S-N curves of NT (TB spacing 35 nm), UFG and CG Cu [83]. (b) Variation of d*a*/dN vs. logΔK for UFG, low-twin-density NT (LDNT; TB spacing about 85 nm), and high-twin-density NT (HDNT; TB spacing about 32 nm) Cu with fixe grain size of about 450 nm [82].

2.5. Numerical modeling of nanotwinned metals

With rapid developments in high-performance computation, numerical modeling is becoming a reliable/indispensable tool of scientific investigation, with an increasingly important role in complementing theory and experiment. Over the past five years, finite element (FE) and classic molecular dynamics (CMD) simulations have been extensively used to model NT metals.

2.5.1. Finite element modeling

In simulating plastic deformation in NT polycrystalline metals via continuum FE, important progresses have been made on (1) adopting crystal plasticity constitutive models containing an intrinsic length scale and (2) treating TB as a strengthening zone of finite thickness.

The post-mortem transmission electron microscopy (TEM) observations showed plenty of dislocations remaining on or piling up against TBs. Motivated by such observations, Suresh and co-workers [84] proposed a TB affected zone (TBAZ) model to capture the effects of TBs on plastic deformation of NT Cu. It is assumed that dislocation-based activities in the vicinity of TBs are the dominant plastic deformation mechanism [84]. In this model, TBAZs spanning 14-20 lattice parameters (5.1-7.2 nm) across TBs are endowed a special slip geometry that involves soft (shear parallel to TB) and hard (shear cross TB) modes of deformation. Combining the TBAZ model and rate-dependent crystal plasticity, Suresh and co-workers implemented two-dimensional FE simulations of NT Cu under uniaxial tension, and obtained results in agreement with the experimental results of Lu et al. [29]. Jerusalem et al. [85] extended the TBAZ model to three dimensions and elaborated the orientation-dependent dislocation blockage and

absorption at TBs by modifying the relevant model parameters. Their simulations captured some of the three-dimensional features of plastic deformation in NT Cu, and provided insights into the relevant failure mechanisms.

To model the strain hardening of TBs, Shen et al. [86] introduced a constitutive equation in which the flow stress to operate deformation in twins is expressed as a power-law function of the TB spacing. At the same time, they adopted crystal plasticity with grain size dependent flow stress to model the plastic deformation of grain interior. Their simulations coupled both grain and twin size effects, with results showing the concentration of deformation near TBs. Wu et al. [87] used cohesive elements to model sliding and separation of TBs and regular GBs, and introduced a conventional theory of mechanism-based strain gradient plasticity for the grain interior. It is noted that TBs have an intrinsic length scale determined by the cohesive constitutive relation used in the model.

2.5.2. Molecular dynamics simulations

Due to the atomic-level resolutions, CMD simulations have become the most broadly used method to study deformation and failure mechanisms in nanostructured materials. During the last five years, a number of CMD simulations have been performed to study mechanical responses of NT metals subjected to different external loadings, such as NT bulk metals under uniaxial tension [75],[76],[88]-[95] or nano-indentation [96]-[99], NT nanowires under uniaxial tension [63]-[72], and NT nanopillars under compression [73],[74]. At the same time, CMD simulations have been used to explore the underlying microscopic mechanisms of plastic deformation in NT metals, focusing on the interaction between dislocations and TBs [53],[100]-[108]. Some results from these atomistic studies

will be successively highlighted in “Introduction” sections in Chapters 4-6 in comparison with relevant experimental observations.

So far, most CMD simulations [88]-[91] of NT bulk metals have used exclusively columnar and quasi-three-dimensional (Q3D) simulation geometries based on periodic boundaries conditions. Such geometries cause severe reductions in the available slip systems of fcc metals (only three slip systems activated in Q3D geometry), as well as the degrees of freedom for GB configurations, which might suppress some important mechanisms (such as nucleation and interaction of dislocation loops) or promote artificial phenomena [76],[94]. In this sense, fully three-dimensional simulations may be necessary for CMD simulations of the deformation mechanisms in NT metals.

2.6. Interaction between dislocation and twin boundary

CTBs are known to have a profound influence on the mechanical behaviors of metals, especially yielding and work-hardening, because they can act as orientation-dependent barriers to obstruct dislocation motion and to arrest dislocations. Although the interaction between dislocation and CTB has been studied for over half a century [8],[13],[109]-[112], the detailed reactions of dislocations at CTB are still not fully understood. The recent studies of NT metals have generated renewed interests in the dislocation-TB interaction in fcc metals. Since the density of TBs increases with decreasing twin thickness, such interactions become increasingly frequent and thus more important in NT metals. Furthermore, understanding dislocation-TB interaction is significantly helpful to investigate the mechanistic effect of NT metals.

When a dislocation approaches a CTB with orientation inclined to the slip direction, there exist in general three types of reactions between the incident dislocation and the

CTB: (1) full absorption of dislocation by CTB; (2) decomposition of dislocation into a residual dislocation remaining on CTB and a transmission dislocation crossing CTB into the adjacent domain; (3) transfer of dislocation through CTB via cross-slip or other reaction mechanisms. The occurrence of these reactions strongly depends on the characteristics of the incident dislocation and the applied stress. Figure 2.12 shows the atomic configurations of absorption and direct transmission, when a $<1\bar{1}0>$ screw dislocation encounters the (111) plane under the anti-shear stress [100]. In Fig. 2.12a, the two partials first constrict to a full screw dislocation, which is then fully absorbed by TB. However, in Fig. 2.12b, the leading partial penetrates through TB without waiting for the trailing partial, leaving a sessile stair-rod dislocation on the TB.

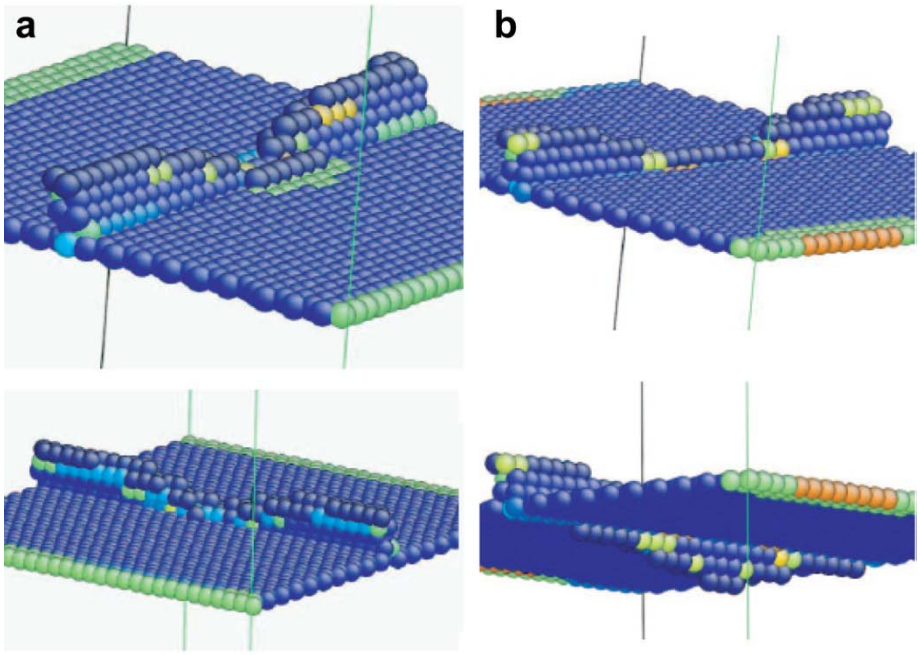

Figure 2.12. Atomic configurations of a full screw dislocation reacting with TB [100]. (a) Full absorption. (b) Direct transmission.

For fcc metals, the dislocation-TB interaction can be easily understood with the assistance of double Thompson tetrahedron, as shown in Fig. 2.13. From in situ TEM

tensile experiments on NT Cu, Wang and Sui [113] observed extended dislocations passing through a CTB, leaving partial dislocations on the CTB. In the process of dislocation transmission through a CTB, the incident dislocation experiences shrinkage, combination and re-dissociation, which can be described by the following reactions,

$$DA \rightarrow D\gamma + \gamma A$$

$$D\gamma + \gamma A \rightarrow DA$$

$$DA \rightarrow BD' + \delta C \rightarrow B\gamma' + \gamma' D' + \delta C \quad \text{(partial } \delta C \text{ remains on TB)}$$

These reactions indicate that an extended dislocation would pass through a CTB through an indirect process with residual dislocations on the CTB.

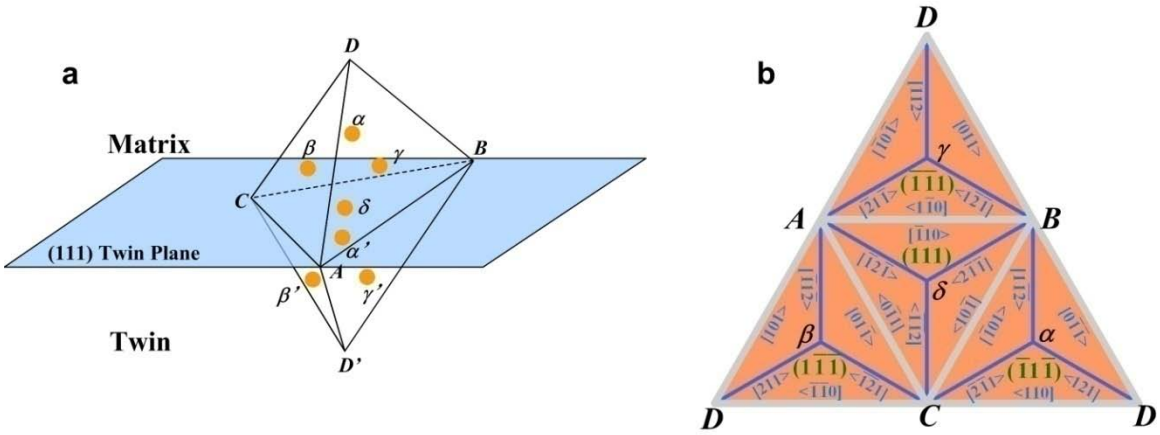

Figure 2.13. Double Thompson tetrahedron representation. (a) Perspective illustration. (b) Plane illustration with Burgers vectors denotation.

Using atomistic simulations, Jin et al. [105],[106] investigated the interaction between isolated screw and non-screw dislocations and a CTB in fcc metals, and quantitatively measured the critical stress for the dislocation to overcome the energy barrier of CTB. For example, for Cu the critical shear stress of screw dislocation is about 465-510 MPa, while for non-screw dislocations, it needs to be larger than 1.2 GPa. Chassagne et al. [108] performed simulations similar to Jin's work on screw dislocation-

TB reaction, and found that the reaction stress is associated with a parameter $\gamma_{SF}/\mu b_p$ (where μ is the shear modulus and b_p is the Burger vector of Shockley partial), which is close to 400 MPa for Cu. Recent in situ TEM straining experiments on Cu [108] showed screw dislocations crossing a CTB after substantial dislocation pile-ups had been established on the incident side. This observation implies that dislocations transmission through TBs may be the result of a collective process, where the local stress can be substantially magnified by dislocation pile-up [108].

Zhu et al. [114] systematically summarized dislocation-TB reactions in fcc metals, and calculated the energy barriers for all the reactions based on the elastic theory of dislocation. Ezaz et al. [107] analyzed the energetic of dislocation-TB reactions using generalized planar SF energy curves calculated from atomistic simulations. Table 2.4 gives a summary of all the possible dislocation-TB reactions in fcc metals [114].

Table 2.4. Summary of dislocation-TB reactions and their energy barriers in fcc metals (Twin plane is ABC plane) [114]

Reaction description	**Equation**	**Isotropic energy barriers**
30° partial, **Bα**		
Cross-slip onto TB	**Bα→Bδ+δα**	E+2.0F
Stair-rod dislocation dissociation	**δα→δB+Bα**	3.5E+5.5F
Transmit across TB	**Bα→Bα′+α′α**	2.7E+4.1F
90° partial, **Dα**		
Cross-slip onto TB	**Dα→Aδ**	0
Transmit across TB	**Dα→δα+δα′+α′D′**	2.0E+4.0F
	Dα→δα+δβ′+β′D′	2.0E+4.0F
	Dα→δα+δγ′+γ′D′	2.0E+4.0F
	Dα→4/9Aδ+α′D′	0.6E+1.4F
	Dα→2/9δB+β′D′	0.1E+0.2F
	Dα→2/9δC+γ′D′	0.1E+0.2F

Cross-slip of perfect screw dislocation, **BC** No dislocation reaction needed		0
Perfect 60° dislocation		
Cross-slip onto TB	**BD→BC+CD**	6.0*E*+7.2*F*
Transmit across TB	**BD→2Bδ+D′B**	4.5*E*+7.5*F*
	BD→δC+D′A	3.0*E*+3.9*F*
	BD→δA+D′C	3.0*E*+3.9*F*
30° leading partial cross-slip onto TB and trailing 90° partial transmit across TB	**D′δ→D′α′ + α′ δ**	2.0*E*-0.3*F*
30° leading partial transmit across TB first and the 90° trailing partial transmit cross TB second	**Dα+αα′→2α′δ+ αD′δ**	4.0*E*
90° leading partial and 30° trailing partial transmit across TB sequentially	**Bα+αδ+ α′δ→Bα′+ 2α′δ**	3.4*E*+2.7*F*
	Bα+αδ+ β′δ→Bα′+ α′δ+ β′δ	2.8*E*+3.7*F*
	Bα+αδ+ γ′δ→Bα′+ α′δ+ γ′δ	2.8*E*+3.7*F*

where $E=\frac{\mu a^2}{72\pi(1-\nu)}\ln\frac{\sqrt{2}d}{a}$, $F=\frac{\mu a^2}{72\pi(1-\nu)}$, μ is the shear modulus, ν the Poisson ratio, a the lattice constant and d the grain size.

Other than their roles as dislocation barriers and traps, CTBs can also act as dislocation sources after they lose coherency during plastic deformation. In the process of in situ TEM tensile experiments on electro-deposited NT Cu, Wang et al. [115] observed atomic steps at TBs associated with the dissociation of perfect dislocations into sessile Frank partial dislocations on TBs. Such steps can serve as dislocation sources to relieve stress concentration. Similar phenomenon has also been observed from straining experiments on UFG Cu with low density of TBs [116],[117].

Remarkably, most recent in-situ nanoindentation studies [118] revealed a novel dislocation multiplication mechanism in which the reaction between a CTB and a full dislocation creates a continuous source to emit twinning dislocations. On the basis of dislocation theory, it is suggested that such mechanism should involve two dissociation processes. One is the dissociation of a full dislocation at a CTB into a Frank partial disconnection and a twinning dislocation, and the second is the emission of a second twinning dislocation from the Frank defect accompanied by a translational shift of the latter. This multiplication mechanism is schematically illustrated in Fig. 2.14.

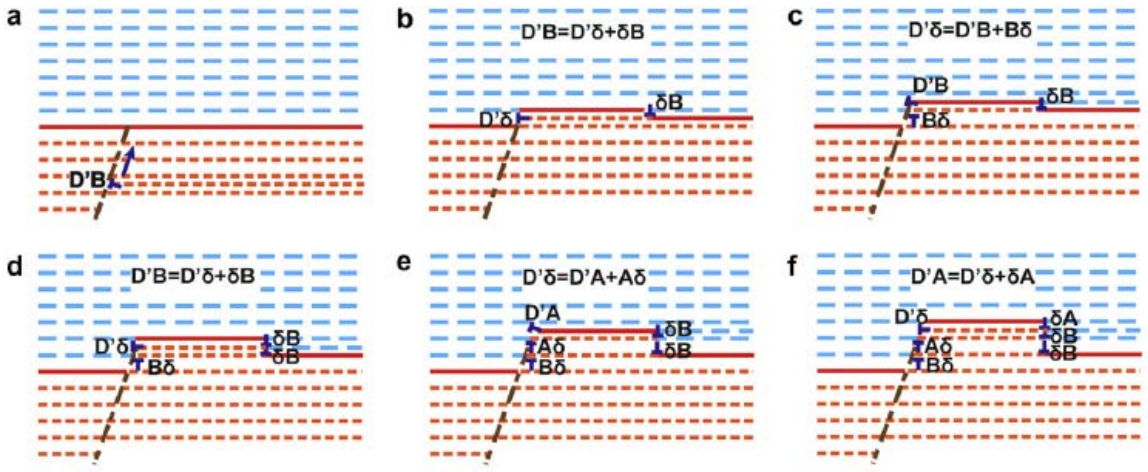

Figure 2.14. Schematic illustration of the dislocation multiplication mechanism through the interaction of a mixed dislocation **D′B** with the TB [118].

Chapter 3 Methodology in Atomistic Modeling

3.1. Molecular dynamics method

Molecular dynamics (MD) is a computational simulation of physical movements of atoms and molecules [119]. The atoms and molecules are allowed to interact with each other for a period of time, giving a view of the motion of the atoms [119]. In general, the trajectories of atoms and molecules are determined by numerically solving the certain equations of motion, where the interatomic force and potential energy are defined via the force fields in molecular mechanics [119]. According to difference in calculating potential energy and interaction, MD method is just divided into classical MD (CMD) and *ab-initio* MD (AIMD). In CMD, the interatomic force can be determined by the empirical potentials based on the Born-Oppenheimer approximation. For AIMD, quantum mechanical methods are used to calculate the potential energy of a system on the fly, so the electronic behavior is obtained from first principles. Since electrons are treated in AIMD, the computational cost of AIMD is much more expensive than that of CMD. Currently, AIMD is only limited to few hundreds of atoms and tens of picoseconds (ps). A popular method in AIMD is Car-Parrinello molecular dynamics (CPMD) [120], which was created by Roberto Car and Michele Parrinello in the 1980s. CPMD combines electronic structure calculations (based on density functional theory) and MD simulations of atomic configuration. Remarkably, it can be applied to the realistic simulations of condensed matter at finite temperature.

In the framework of CMD, for a system containing N atoms, the equations of motion of each atom are obtained based on the Newton's second law,

$$m_i \ddot{\mathbf{r}}_i = \mathbf{f}_i \tag{3.1}$$

where m_i is the mass of the ith atom, $\mathbf{r}_i$ is the Cartesian coordinates, and $\mathbf{f}_i$ is the interaction force between ith atom and other atoms, and "·" represent the derivative with respect to the time. The force is determined by

$$\mathbf{f}_i = -\frac{\partial U}{\partial \mathbf{r}_i} \tag{3.2}$$

where U represent the potential energy of system. In CMD simulation, the typical process is to numerically integrate Eq. (3.1) via iteration. Figure 3.1 shows a typical flow chart in CMD simulations. For convergence, the time step must be less than the inverse of maximum vibration frequency of atoms. For the atomic system, the maximum vibration frequency is about 10^{15} /s. Therefore, the typical time step of CMD is around 1 femtoseconds (fs).

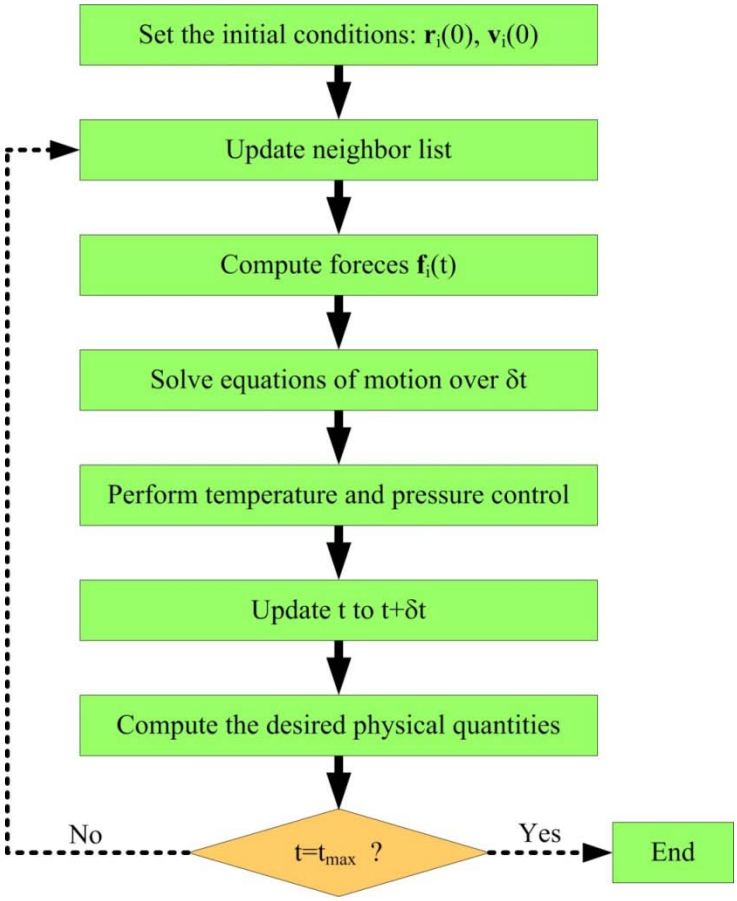

Figure 3.1. Flow chart of CMD simulations.

Due to the atomic-level spatial and temporal resolution, CMD simulations have been the most broadly used strategy to study deformation and failure of nanostructured materials during the last decade. Specially, CMD simulations were applied to investigate plastic deformation of NC metals [121]. There are two specific examples that show the value of CMD simulations in studying NC metals. One is that it predicted the occurrence of deformation twinning in NC Al prior to the experiments [9], and another is that it suggests the transition from dislocation-based mechanism to GB-mediated process as grain size decreases [17]. With the rapid development of supercomputer and advancement in computational technology, CMD simulations are playing an increasingly important role in investigation of nanostructured materials.

3.2. Empirical interatomic potentials

When CMD are used to simulate the system of atoms, the reliability of CMD simulations is fully determined by the accuracy of interatomic potentials. Therefore, the interatomic potential is considered as the foundation of CMD. In this section, we describe some of the most common empirical potentials.

3.2.1. Pair potentials

Pair potentials are the simplest choice for describing atomic interactions. The pair potentials frequently used in CMD simulation for metallic systems include Lennard-Jones (LJ) potential and Morse potential. The most common LJ potential is expressed as

$$U_{LJ} = 4\varepsilon\left[\left(\frac{\sigma}{r}\right)^{12} - \left(\frac{\sigma}{r}\right)^{6}\right] \tag{3.3}$$

where ε is the depth of the potential well, σ is the finite distance at which the interatomic potential is zero, and r is the distance between atoms. The r^{-12} term describes Pauli repulsion at short ranges due to overlapping electron orbitals, while the r^{-6} term represents the attraction at long ranges.

Another common pair potential is Morse potential, which is defined as

$$U_M = D_e\left\{1-\exp\left[-a\left(r-r_e\right)\right]\right\}^2 \tag{3.4}$$

where D_e is the well depth, r_e is the equilibrium bond distance (i.e. the near neighbor lattice spacing), and a is a parameter to control the "width" of potential. In process of force calculation, the cost of Morse potential is higher than that of LJ potential due to the exponential term. However, relative to LJ potential, Morse potential is more realistic for many materials.

3.2.2. Many-body potentials

Pair-wise potential is just a kind of two-body potentials. For metallic system, the pair potentials have been found to have the following shortcomings [122]:

(1) For most cubic metals, the ratio of the elastic constant, C_{12} to C_{44} is far from unity, where the pair potentials lead to Cauchy relation, i.e. $C_{12}=C_{44}$;

(2) Pair potentials give a prediction of unrelaxed vacancy formation energy around cohesive energy, which is completely incorrect;

(3) Pair potentials fail to predict an inward relaxation of metallic surface;

(4) Pair potentials overestimate the melting point by 20% of experimental measurements;

(5) Pair potential with a functional form having only one optimum at the diatomic equilibrium distance cannot be fitted properly to the phonon frequencies.

Therefore, many-body potentials are required to accurately describe metallic bonding. The idea behind multi-body potentials is to incorporate the influence of local environment on interatomic interaction. The common many-body potentials for metals include embedded-atom-method (EAM) potentials [123],[124], Fininis-Sinclair potentials [125], Sutton-Chen potentials [126], and Murrell-Mottram potentials [127].

The EAM potential for metals is typically given in the form

$$U = \frac{1}{2}\sum_{ij} V\left(r_{ij}\right) + \sum_{i} F\left(\overline{\rho}_i\right) \tag{3.5}$$

where $V\left(r_{ij}\right)$ is a short-range pair potential as a function of distance r_{ij} between atoms i and j, and F is the embedding energy as a function of the host electron density $\overline{\rho}_i$ induced at site i by all other atoms in the system. The electron density $\overline{\rho}_i$ is given by

$$\bar{\rho}_i = \sum_{j \neq i} \rho\left(r_{ij}\right) \tag{3.6}$$

where $\rho\left(r_{ij}\right)$ is the electron density function.

In this dissertation, we use the EAM interatomic potential developed by Mishin et al. [124] to calculate the interatomic force. This empirical potential is very reliable, because it accurately reproduces the basic equilibrium properties of Cu, such as elastic constants, phonon-dispersion curves, vacancy formation and migration energies, SF energies, and specific interfacial energies, and also provides energies and stability of nonequilibrium structures. Specially, for pure Cu, this potential estimates TB and SF energies of 22.2 and 44.4 mJ/m^2, respectively, which agree very well with *ab-initio* calculations and experimental measurements.

3.3. Multiple time step algorithm

Over the past decades, researchers have paid much attention to extending the time scale of CMD simulations, in order to speed up the integration of CMD. Tuckerman et. al. [128] proposed a multiple time step integration method called the reversible reference system propagator algorithm (rRESPA). This method can run at much faster speeds than other standard algorithms, such as Verlet and Leapfrog. The rRESPA method has been successfully implemented in various complex systems [129]-[136] with a speedup factor of 4 to 15. Furthermore, the rRESPA method can be carried out to accelerate simulations for systems with different time scales [137]. A brief introduction to the rRESPA method is given as follows.

The rRESPA method implements a force split based on the interaction distances of interatomic forces, and then divide the Liouville operator *L* into two parts,

$$iL = \dot{\mathbf{r}}\frac{\partial}{\partial \mathbf{r}} + \mathbf{F}_f(\mathbf{r})\frac{\partial}{\partial \mathbf{p}} + \mathbf{F}_s(\mathbf{r})\frac{\partial}{\partial \mathbf{p}} = iL_f + \mathbf{F}_s(\mathbf{r})\frac{\partial}{\partial \mathbf{p}} \tag{3.7}$$

where **r**, **F** and **p** are coordinate, force and conjugated momentum in the system, respectively. In this algorithm, the fast force $\mathbf{F}_f$ is computed after each time step δt, and the slow force $\mathbf{F}_s$ is determined every n time steps $\Delta t = n\delta t$. Using the symmetrical Totter factorization, one can obtain the following dynamic trajectory within a unit time step,

$$\mathbf{r}(\Delta t) = \mathbf{r}_f\left\{\Delta t; \mathbf{r}(0), \dot{\mathbf{r}}(0) + \frac{\Delta t}{2m}\mathbf{F}_s\left[\mathbf{r}(0)\right]\right\} \tag{3.8}$$

$$\dot{\mathbf{r}}(\Delta t) = \dot{\mathbf{r}}_f\left\{\Delta t; \mathbf{r}(0), \dot{\mathbf{r}}(0) + \frac{\Delta t}{2m}\mathbf{F}_s\left[\mathbf{r}(0)\right]\right\} + \frac{\Delta t}{2m}\mathbf{F}_s\left[\mathbf{r}(\Delta t)\right] \tag{3.9}$$

where $\mathbf{r}_f\{\ldots;\ldots,\ldots\}$ and $\dot{\mathbf{r}}_f\{\ldots;\ldots,\ldots\}$ represents the solutions of the fast force subject to the initial conditions $\left\{\mathbf{r}(0), \dot{\mathbf{r}}(0) + \Delta t\mathbf{F}_s\left[\mathbf{r}(0)\right]/2m\right\}$, and m is the atomic mass. The implementation of rRESPA consists of iterations in terms of the above integration schemes. Such iterations can reduce the computing time spent in evaluating interatomic forces, and accelerate the integration of the equations of motion. Notably, the propagator $G(t)=\exp(iLt)$ is a unitary operator, i.e., $G(-t)=G^{-1}(t)$, which ensures that rRESPA method is exactly time reversible. In this dissertation, we use this advanced algorithm as integrator of CMD simulation.

3.4. Ensembles

CMD simulations are based on the statistical mechanics. Three ensembles are commonly defined in CMD simulations: (1) microcanonical ensemble (NVE), (2) canonical ensemble (NVT), and (3) isothermal-isobaric ensemble (NPT).

In the microcanonical ensemble, the system is isolated from changes in number (N), volume (V) and energy (E) [138]. Therefore, the total energy in such ensemble is always conserved when N keeps conserved.

In canonical ensemble, the number (N), volume (V) and temperature (T) are conserved. The energy of endothermic and exothermic processes is exchanged with a thermostat bath [138]. In NVT, popular techniques to control temperature include velocity rescaling, Berendsen thermostat [139], Nose-Hoover thermostat [140],[141] and Lagevin dynamics [142].

In isothermal-isobaric ensemble, the number (N), volume (V) and pressure (P) are conserved. In addition to thermostat, a barostat bath is needed to adjust pressure. The common techniques to control pressure include Berendsen barostat [139], Anderse barostat [143] and Parrinello-Rahman barostat [144].

Here we briefly introduce the Nose-Hoover thermostat and the Berendsen barostat. In the Nose-Hoover thermostat, the equations of motion are modified as [142]

$$\ddot{\mathbf{r}}_i = \frac{\mathbf{f}_i}{m_i} - \xi \dot{\mathbf{r}}_i \tag{3.10}$$

$$\dot{\xi} = \frac{1}{\tau^2}\left[\sum_i \frac{m_i \dot{\mathbf{r}}_i^2}{g k_B T} - 1\right] \tag{3.11}$$

where g is the total number of degrees of freedom, τ is a free parameter representing the strength of the coupling of the system to the thermostat, and ξ is the friction coefficient. In this thermostat, the Helmholtz free energy of atoms and thermostat is conserved.

In the Berendsen barostat, the system pressure is set toward a desired value by changing the dimensions of the simulation cell size during the simulation. The scaling factor (for each dimension) is

$$\mu = \left[1 - \frac{\beta \delta t}{\tau_P} \left(P_0 - P(t) \right) \right]^{1/3} \tag{3.12}$$

where P_0 is the desired value of pressure, τ_P is the coupling time constant for the pressure scaling, δt is the time step, and β is the isothermal compressibility of the system. The scaling is done for all components of the atom positions as well as the simulation cell dimensions.

3.5. Parallel computing algorithms

When CMD simulations are implemented on a distributed memory computer (i.e. in parallel manner), how to assign atoms (total number is *N*) to difference processors (total number is *P*) is a key operation. Generally, there are two strategies with this operation: (1) atom decomposition [145],[146], (2) force decomposition [147],[148], and (3) domain decomposition [149],[150].

Atom decomposition is trivial, i.e. averagely assign all of atoms to processors, each processor holds *N*/*P* atoms. The replicated-data strategy and the systolic method are well developed for atom decomposition. Such scheme can lead to good loading balance, but the global communication between processor is needed at each time step. Therefore, this scheme becomes inefficient for large numbers of processors. The atom decomposition scales as $O(N^2/P)$ for time, $O(N/P)$ of storage per node and $O(N)$ for communication per node.

Force decomposition is based on the assignment of blocks of force matrix to processors using a certain ordering of processors and blocks. Although no inter-processor communication is needed in this scheme since all possible interactions are assigned to processors, this scheme requires very complex algorithms.

Domain decomposition assigns a sub-region (containing a certain number of atoms) of computational domain to each processor. The entire domain is divided into 3D cells, and each processor is responsible for calculating the total force on atoms in its sub-domain. Such scheme just maps the physical space to array of processors, and so only local communication between processors is required, when the cutoff radius is used. The scaling of this scheme is $O(N^2/P)$ for time, $O(N/P)$ of storage per node and $O((N/P)^{2/3})$ for communication per node.

In our developed parallel program, we use the domain decomposition algorithm. The local communication between neighboring processors is achieved via MPI library.

3.6. Loading methods

In CMD simulations, four loading methods are often used to apply the strain or stress on the simulated system. The first method is imposing the given displacement on atoms at the ends along the required loading direction every certain time steps. The second one is applying the uniform strain on all of atoms via rescaling the coordinates of atoms every certain time steps [151]. The third one is imposing the constant velocity on atoms at the ends along the required loading direction in each time step. The fourth one is applying constant stress along the required loading direction via pressure control. In first two methods, free relaxation is implemented on atoms without constraints between two loadings. Such operation is just to avoid the influence of stress wave introduced by the

current loading step, and enable the system close to equilibrium state at the beginning of next loading step. For the fourth method, periodic boundary condition must be imposed in the required loading direction.

3.7. Force and stress computation

In CMD simulation, the most intensive part of computation is calculation the interatomic force by Eq. (3.2). In the force calculation, the central operation is finding all atom pairs. This operation can be achieved via the linked-list cell algorithm [152]. This algorithm works by subdividing the simulation domain into cells with an edge length greater than or equal to the cut-off radius of the interaction to be computed. The atoms are sorted into these cells and the interactions are computed between atoms in the same or neighboring cells. This algorithm is very efficient, and the total computation cost just scales as $O(N)$ for N atoms

In CMD simulations, we compute atomic stress using the Virial stress theorem [153]. This theorem defines the Virial stress as

$$\sigma_{i,kl} = \frac{1}{V_i}\left(-\frac{p_{i,k}\, p_{i,l}}{m_i} + \frac{1}{2}\sum_{j \neq i} \frac{\partial U}{\partial r_{ij}} \frac{r_{ij,k}\, r_{ij,l}}{r_{ij}} \right) \tag{3.13}$$

where $\sigma_{i,kl}$ is the kl component of stress tensor of atom i, V_i is the Voronoi volume of atom i, $p_{i,k}$ is the k component of momentum of atom i, m_i is the mass of atom i, $r_{ij,k}$ is the k component of interatomic distance $r_{ij} = r_i - r_j$ between atoms i and j. The Virial stress needs to be averaged over space and time to converge to the Cauchy stress tensor.

3.8. Visualization techniques

In CMD simulations for deformation of metals, post-processing of the atomic information requires various techniques and computational tools to effectively visualize defects formed during the deformation process. Several approaches have been used to visualize defects (primarily dislocation), including centrosymmetry [154], local crystalline order (recalled as common neighbor analysis) [155],[156], slip vector [157], energy [158] or coordination number [159]. In this dissertation, we mainly use the local crystalline order method to identify the defect.

According to the local crystalline order and coordination number, we paint atoms with various characters in different colors. Atoms with fcc order are colored in gray, atoms with hcp order are in red, atoms with non-fcc and non-hcp order but coordinate number of 12 are in green, atoms with non-fcc and non-hcp order but coordinate number of 10 or 11 are in blue, and other atoms are in yellow. Therefore, gray atoms are in fcc lattice structures, green ones are generally in dislocation cores or GBs, blue one are near the vacancies, and yellow ones represent full disorder atoms. A single red layer represents a TB, two adjacent red layers indicates an intrinsic SF and two red layers separated by a gray layer stands for an extrinsic SF.

3.9. Advantages and limitations of classic molecular dynamics simulations

When CMD simulation is applied to study deformation of NC or NT metals, it can provide atomic details and insights to help us understand the microscopic deformation mechanisms, because it has the atomic-level spatial and temporal resolution in nature. In

experiments on deformation of materials, due to limitation of instruments or visualization techniques, it is difficult and sometimes impossible to observe the microstructural evolution inside of materials. However, CMD simulation is able to detect the process and the structures inaccessible to experiments.

So far, CMD simulation is only capable to provide the qualitative comparison with the experiments, there is still a big gap in the quantitive comparison. The reason is the inherent limitations in spatial and temporal scales. Currently, CMD simulations can only deal with nanoscale matter (typically containing tens of millions of atoms) subject to nearly instantaneous (up to a few nanoseconds) loading and deformation. To overcome this limitation of CMD, many researchers attempted to establish and develop multiscale methods by coupling mesoscopic or continuum level methods. However, most of multiscale methods currently are only limited to certain field. On the other hand, the rapid development of supercomputer and advancement in computational technology provide a possible path to improve the length-scale and time-scale of CMD simulations, which will reduce the gap between CMD simulation and the real experiments.

3.10. High performance computing and supercomputers

High-performance computing (HPC) uses supercomputers and computer clusters to solve advanced computation problems [160]. HPC integrates systems administration (including network and security knowledge) and parallel programming into a multidisciplinary field that combines digital electronics, computer architecture, system software, programming languages, algorithms and computational techniques [160]. HPC technologies are the tools and systems used to implement and create high performance

computing systems [160]. Recently, HPC systems have shifted from supercomputing to computing clusters and grids.

A supercomputer is a computer at the frontline of current processing capacity, particularly speed of calculation [160]. Supercomputers are used for highly calculation-intensive tasks such as problems including quantum physics, weather forecasting, climate research, molecular modeling (computing the structures and properties of chemical compounds, biological macromolecules, polymers, and crystals), and physical simulations (such as simulation of airplanes in wind tunnels, simulation of the detonation of nuclear weapons, and research into nuclear fusion) [160].

In general, the speed of a supercomputer is measured in "FLOPS", i.e. floating point operations per second, commonly used with an SI prefix such as tera- (10^{12}) or peta- (10^{15}). Figure 3.2 shows the development of computing performance over twenty years. In November 2008, IBM installed the first petaflog supercomputer (called as Roadrunner) in the world. In November 2011, Japan's "K Computer" ranked the first place in Top500 supercomputer over the world. It consists of 705,024 cores, and its average computing capacity is up to 10.51 petaflops, and the peak capacity reaches 11.28 petaflops.

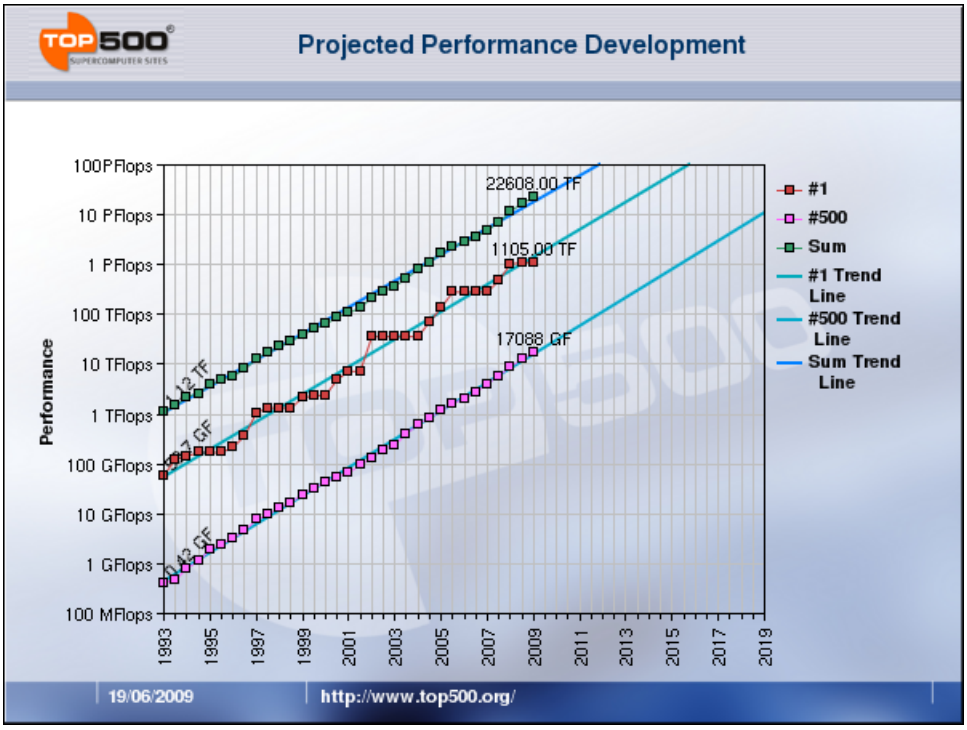

Figure 3.2. Development of computing performance over twenty years (from http://www.top500.org).

3.11. Supercomputer resource

For implementation the massive parallel CMD simulations, TeraGrid awarded us a generous grant (No. MSS090046) with 2,700,000 Service Units (SUs, 1 TeraGrid SU is equivalent to one CPU-hour on a Phase-1 DTF cluster) on Kraken Cray XT5 system at National Institute for Computational Science (NICS).

TeraGrid is an integrated and persistent computational resource by working in partnership with eleven Resource Sites around the country. Currently, TeraGrid resources include more than a petaflop (10^{15} flop) of computing capability and more than 30 petabytes of online and archival data storage, with rapid access and retrieval over high-performance networks. TeraGrid is the world's largest, most comprehensive distributed cyber-infrastructure for open scientific research.

Kraken Cray XT5 system is a super-cluster with 8,256 compute nodes. Each node has two 2.6 GHz six-core AMD Opteron processors (Istanbul) and 16 GB of memory. The peak calculation capability of the system is up to 1,030 teraflops, hence Kraken Cray XT5 system ranks the 3th place in the present Top500 supercomputers. This system has a high-performance network connection. Compute nodes run Cray Linux Environment 2.2. Each node is connected to a Cray SeaStar router through HyperTransport, and the SeaStars are all interconnected in a 3-D-torus topology.

Chapter 4 Deformation Mechanisms in Polycrystalline Nanotwinned Bulk Copper

4.1. Introduction

As described in Chapter 2, in comparison with twin-free NC or UFG metals, NT bulk metals exhibit an unusual combination of ultrahigh strength, good tensile ductility, enhanced strain hardening, high strain-rate sensitivity, remarkable fracture toughness and fatigue resistance. At present, the underlying deformation mechanisms responsible for these greatly enhanced mechanical properties are the subject of intense experimental, theoretical and computational studies that aimed at understanding the specific deformation behaviors in NT metals and at providing guidance for material processing and structural optimization.

Using atomistic reaction pathway calculations (i.e. via free-end nudged elastic band method to determine the minimum energy paths), Zhu et al. [100] revealed that the mechanistic origin of high rate sensitivity and good tensile ductility in NT metals lies in the slip transfer reactions between dislocations and CTB. They also pointed out that the slip transfer reactions mediated by TBs dominate plastic deformation as the rate-controlling mechanisms [100], consequently resulting in small activation volume in NT metals. Concomitantly, it was found that in the slip transfer reactions, small activation volume arises because only a small group of atoms are involved during the cross-slip process [161]. In CMD simulations of NT Cu, Zheng et al. [103] observed complete

transmission of screw dislocations through TBs via cross-slip, along with incomplete transmission of non-screw dislocations and transmission-induced jog formation. These mechanisms are operative in maintaining the high strength and good ductility of NT metals. Wu et al. [102] reported two new dislocation reactions with CTB from atomistic simulations: the first one involves a 60° dislocation interacting with CTB, creating a {001}<110> Lomer dislocation, which, in turn, dissociated into Shockley, stair-rod and Frank partials; the second one has a 30° partial slipping transfer slip through CTB, generating three new Shockley partials. The former reaction leaves immobile dislocations on TBs, which can effectively pin or block further dislocation motion, while the latter reaction induces high population of mobile dislocations on TBs, which facilitate further plastic flow.

In this chapter, we investigate the strengthening and softening mechanisms responsible for the observed twin size effects of NT bulk Cu with equiaxed grains. At the same time, we also explore the orientation effect on deformation mechanisms of NT bulk Cu with the columnar grains.

4.2. Deformation in polycrystalline nanotwinned copper with equiaxed grains

4.2.1. Experimental studies

Recently synthesized NT bulk Cu with equiaxed grains has achieved a strength increase by a factor of 7 to 10 relative to conventional coarse-grained polycrystalline Cu, as well as considerable ductility and high electrical conductivity [28],[29]. More interestingly, the strength of such NT Cu first increases as the TB spacing λ decreases,

reaching a maximal strength at λ=15 nm, then decreases as λ is further reduced [29], as shown in Fig. 4.1a. The trend of increasing strength in NT UFG Cu with decreasing λ can be relatively well explained by the Hall-Petch effect since the twin planes can serve as barriers to dislocations gliding on inclined slip planes (see Fig. 4.1b). However, the strength softening with further decreasing of λ from 15 nm to 4 nm is intriguing. For twin-free NC metals, MD simulations [16],[17] have shown a strength softening mechanism as grain size is reduced to about 10 nm in Cu, which has been attributed to a transition from dislocation mediated plastic deformation to GB associated mechanisms such as GB sliding, GB diffusion, and grain rotation [14]-[21]. In NT UFG Cu, the observed strength softening cannot be attributed to GB associated mechanisms for the following reasons: (1) twin planes are coherent in nature, and shearing along them is as difficult as most other atomic planes; and (2) grain sizes and GB properties for samples with different twin thicknesses are similar [28],[29]. While it has been speculated that the softening in NT Cu might be caused by pre-existing dislocations potentially acting as easy dislocation sources in samples with smaller λ [29], it remains difficult to reveal the detailed interactions between dislocations and twin planes from post-mortem microstructure observations.

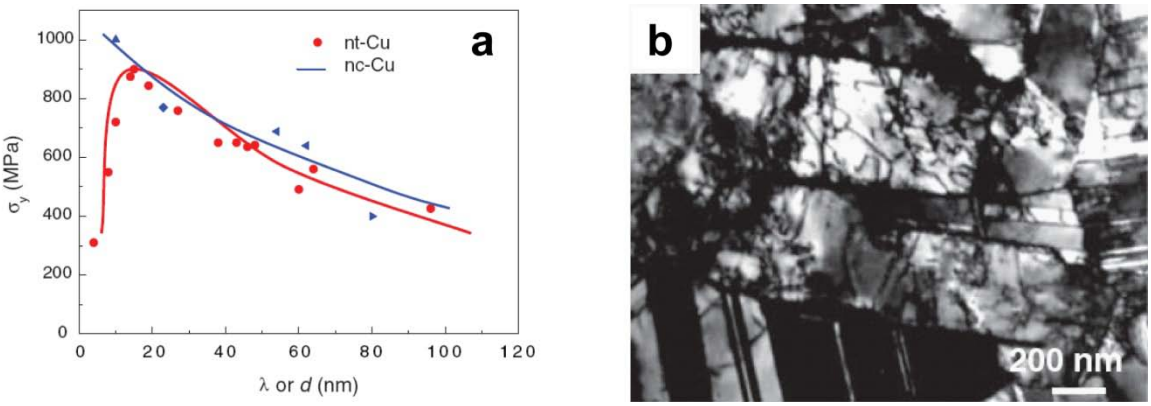

Figure 4.1. Results from experiments on NT Cu with equiaxed grains [29]. (a) Yield strength as a function of TB spacing λ for NT Cu, in comparison with that of NC Cu as a function of grain size d. (b) A typical bright TEM image of the deformed NT Cu showing the tanglement and TB obstruction of dislocations.

In the next section, we use massively parallel atomistic simulations to investigate the effect of twin thickness on the deformation mechanisms in NT equiaxed-grained Cu. The simulations will show that the strength softening in NT Cu is in fact governed by dislocation nucleation at GB-TB intersections. Such dislocation nucleation controlled strength is rarely observed because dislocations can easily multiply given sufficient space. A possible exception is the strengthening mechanism of micro- and nanopillars, which has been attributed to increasing difficulty for dislocation nucleation and multiplication as the structure dimension is reduced [162]-[165].

4.2.2. Atomistic simulations

The simulations are performed on 3-dimensional polycrystalline samples containing 27 randomly orientated Voronoi grains of nearly-equiaxed shape. In each grain, twins are inserted by mirroring a portion of the matrix with respect to a twin plane. The same Voronoi grain structure is scaled to obtain samples with different grain sizes and TB spacing. Crystallographic orientations of all grains are retained as TB spacing and/or

grain size change. The samples with d=10 nm and d=20 nm have dimensions of 30×30×30 and 60×60×60 nm^3, containing about 2,300,000 and 18,500,000 atoms, respectively. For d=10nm, six samples with initial uniform twins of spacing λ=0.63 nm, 0.83 nm, 1.25 nm, 1.67 nm, 2.92 nm, and 3.75 nm are simulated. For d=20 nm, five samples with λ=0.83 nm, 1.25 nm, 2.08 nm, 2.50 nm, and 6.25 nm are simulated.

The EAM potential [124] for Cu is adopted. All simulations are performed at room temperature using Nose-Hoover thermostat [140]. The multiple time step algorithm [128] is used with shorter and longer time steps of 2 fs and 6 fs, respectively. Periodic boundary conditions are imposed in all three directions. The sample is relaxed for 500 ps before straining. During uniaxial tension, a 15% strain is applied to each sample in 750 ps at a constant strain rate of 2×10^8 /s. The simulations consumed a total computation time of 22.8 CPU years (corresponding to 3×10^{18} Flops) in Kraken Cray XT5 system at the National Institute for Computational Sciences. The local crystalline order method [156] is used to identify defects during deformation.

Stress versus strain curves for two different grain sizes d=10 nm, 20 nm, and various values of the TB spacing are shown in Fig. 4.2a. It can be seen in Fig. 4.2b that the average flow stress first increases with decreasing TB spacing λ, reaching a maximum at a critical TB spacing, and then drops progressively with further decreasing of λ, in qualitative agreement with experimental observations [29].

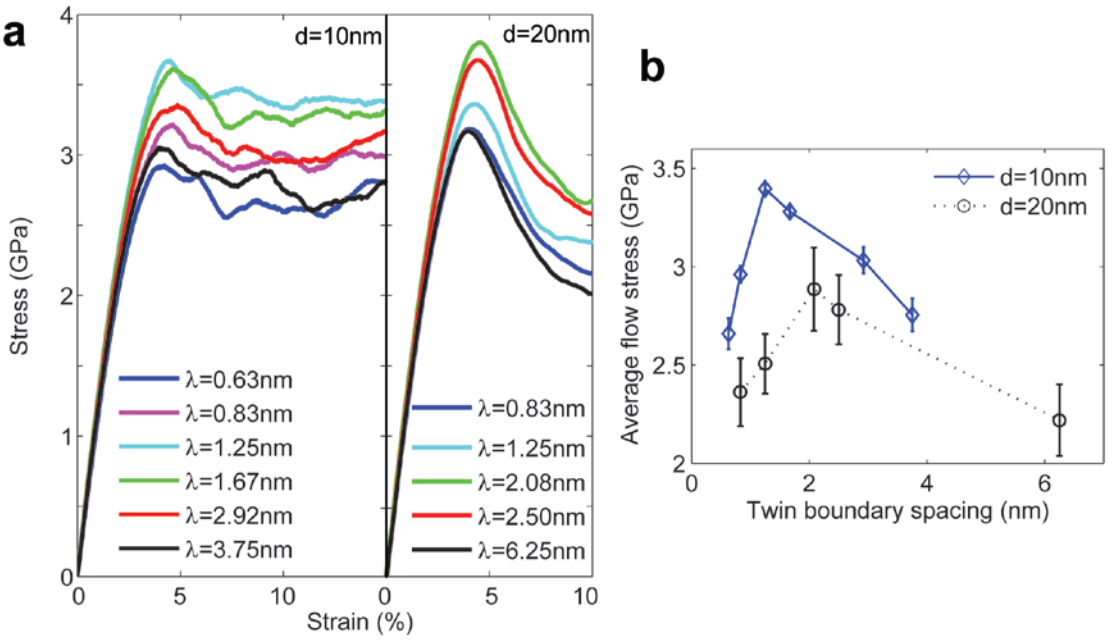

Figure 4.2. Stress-strain relations and flow stress from MD simulations of NT Cu. (a) Simulated stress-stain curves for NT Cu with different values of TB spacing for two grain sizes d=10 nm (left) and d=20 nm (right). (b) Averaged flow stress from an engineering strain of 6% to 15% for d=10 nm and 6% to 10% for d=20 nm. The flow stress first rises as the TB spacing decreases, reaching a maximum at a critical TB spacing, and then drops as twins are further narrowed.

Deformation patterns of two samples with different TB spacing but the same grain size d=20 nm are shown in Fig. 4.3. The result for the sample with λ=1.25 nm at 10% strain is shown in Fig. 4.3a where plastic deformation is dominated by TB migration: partial dislocations are observed to nucleate at GBs and glide along the twin planes, resulting in a change of TB spacing. Dislocations intersecting with twin planes are rarely seen here. The observed TB migration induced by the motion of leading partial dislocations is consistent with previous investigation [6],[8],[166]. In the sample with λ=6.25 nm, shown in Fig. 4.3b, plenty of dislocations intersecting twin planes are observed. In the latter case, plastic deformation is dominated by partial dislocations

emitted from GBs cutting into the neighbouring twin planes, and TB migration plays a much lesser role in accommodating plastic deformation. Typical dislocation structures in the interior of a grain are shown in Fig. 4.4. Figure 4.4a shows several partial dislocations nucleated from GBs and moving parallel to TBs in the λ=1.25 nm sample at 4% strain. As the sample is further loaded to 7% strain (see Fig. 4.4b), most dislocation lines are parallel to, and rarely seen to intersect with, the twin planes. In contrast, for the sample with the same grain size but larger TB spacing λ=6.25 nm at 5.4% strain, dislocations are commonly seen to nucleate from GBs and intersect TBs (Fig. 4.4c). In the samples with grain size d=10 nm, we found the same transition in deformation mechanism as the TB spacing is reduced. The evolution of the number of hcp atoms associated with SFs shown in Fig. 4.5 also confirms that there exists a transition in deformation mechanism at a critical TB spacing.

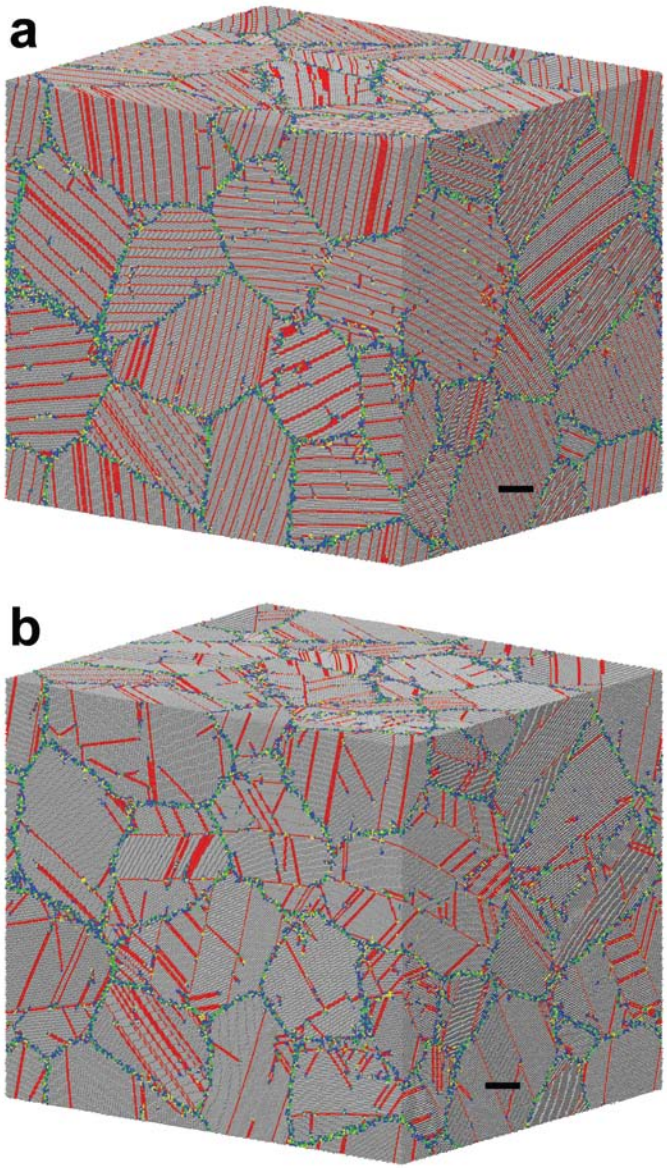

Figure 4.3. Simulated deformation patterns in NT samples with grain size d=20 nm at 10% strain (scale bar: 5 nm). (a) Sample with TB spacing λ=1.25 nm and (b) λ=6.25 nm. In (a), plastic deformation is dominated by partial dislocations gliding parallel to twin planes, while dislocations cutting across twin planes is the controlling deformation mechanism in (b).

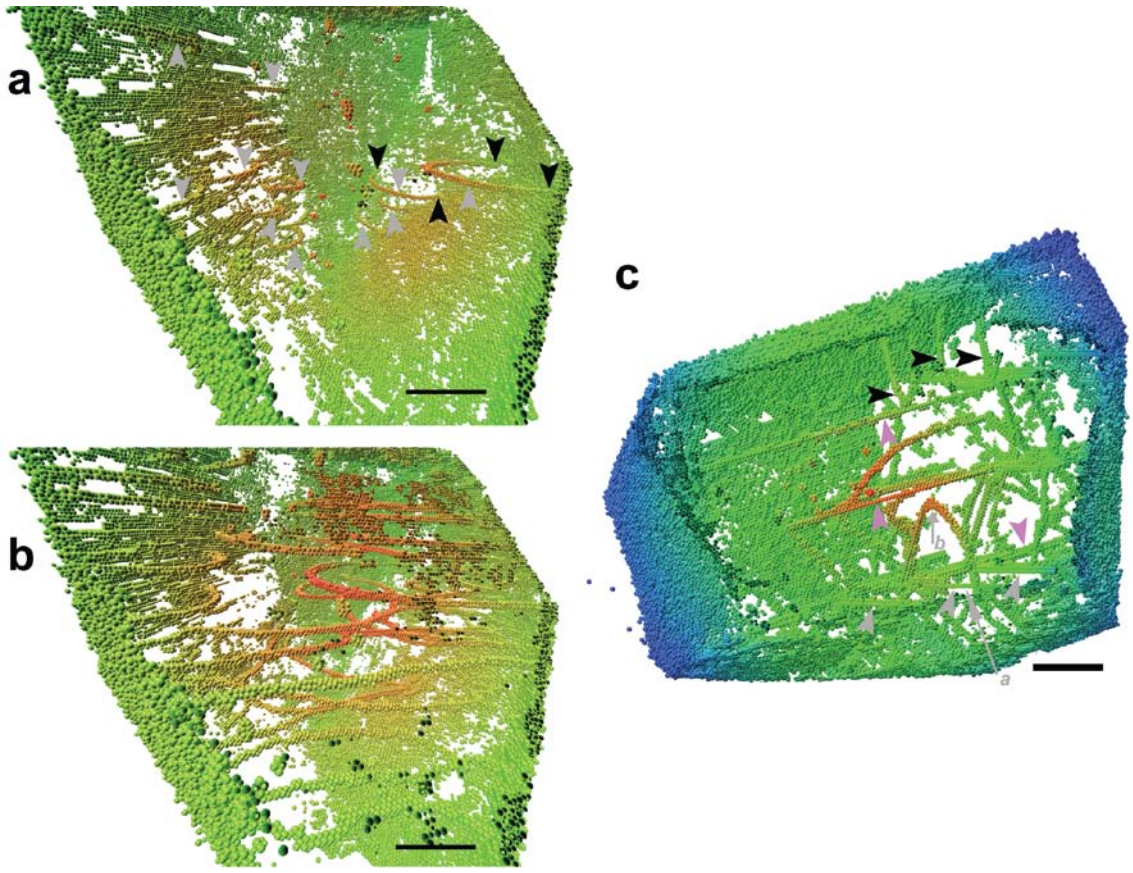

Figure 4.4. Dislocation structures in d=20 nm sample (scale bar: 5 nm). Coloring is based on distance of atoms to grain center. (a) In λ=1.25 nm sample at 4% strain, dislocations (gray and black arrows) are seen to nucleate from GBs and move parallel to TBs. (b) In λ=1.25 nm sample at 7% strain, dislocations remain parallel to TBs. (c) In λ=6.25 nm sample at 5.4% strain, dislocations intersect (black and gray arrows) or lie parallel (purple arrows) to TBs. One dislocation is seen to cut through a TB, leaving behind a residual partial label ‘a’ on the TB and a transmission dislocation ‘b’.

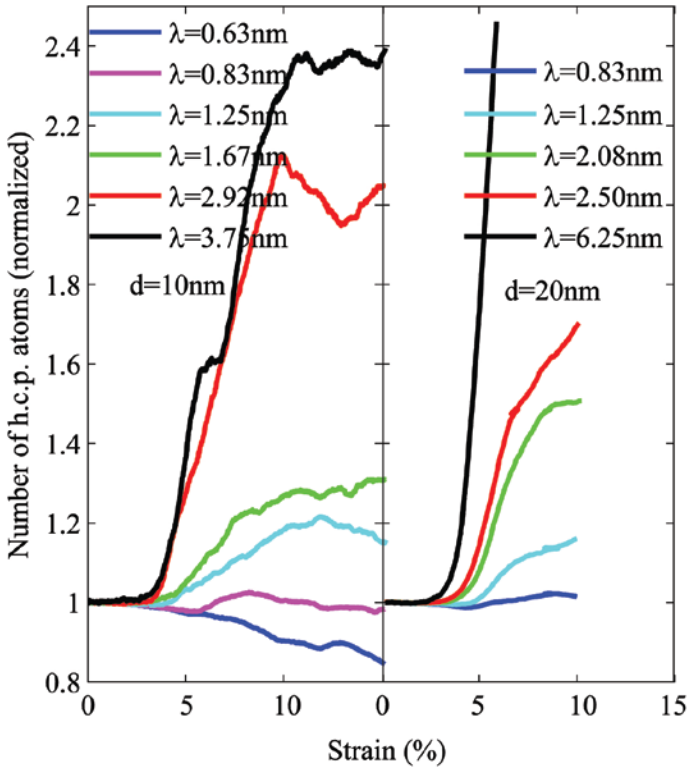

Figure 4.5. Variation of the number of hcp atoms as a function of strain in 3-dimensional MD simulations. The number of hcp atoms for each case is normalized by their respective hcp atoms at 0% strain. Decreasing number of hcp atoms corresponds to TB annihilation. Small variation indicates partial TB migration. Increasing hcp atoms is related to the nucleation (from GBs) of dislocations on inclined slip planes and the associated SFs intersecting with TBs.

Figures 4.6 capture the atomic view of one grain in NT samples with grain size *d*=20 nm under 10% strain. It is seen that dislocations glide along TBs for smaller TB spacing, while dislocations intersect with TB for larger TB spacing. Such dislocation mechanism transition results in the transition of yield strength in NT Cu from hardening to softening. In simulations on samples with larger TB spacing, a lot of dislocations interact with each other, leading to the formation of dislocation junctions which play an essential role in the strain hardening of deforming crystals [167]. However, the simulations of samples with smaller TB spacing show that partial dislocations nucleate from GB-TB intersections, and

then glide along parallel TBs. The successive emission of partial dislocations will broaden/narrow the twin regions, and also induce TB migration. Such deformation mechanism is responsible for the observed strength softening in NT samples. It has been shown in the literature that the stress required to move dislocations parallel to the TB is on the order of 10 MPa [168], which is negligible compared to the magnitude of stress shown in Fig. 4.2a. Therefore, once dislocations are nucleated, they could glide easily along TBs. If the critical stress to drive parallel dislocation motion is so small, what prevented this mechanism from dominating deformation at all TB spacing? Our simulations show that, below the critical twin thickness, plastic flow is controlled by the nucleation rate of dislocations parallel to the TBs, while at large TB spacing, there are insufficient operative sources for parallel dislocation motion, even if their motion is easy. At large TB spacing, it becomes favorable to nucleate dislocations on multiple slip systems even if such dislocations must pay the price of pursuing more difficult paths that include cutting across TBs after nucleation.

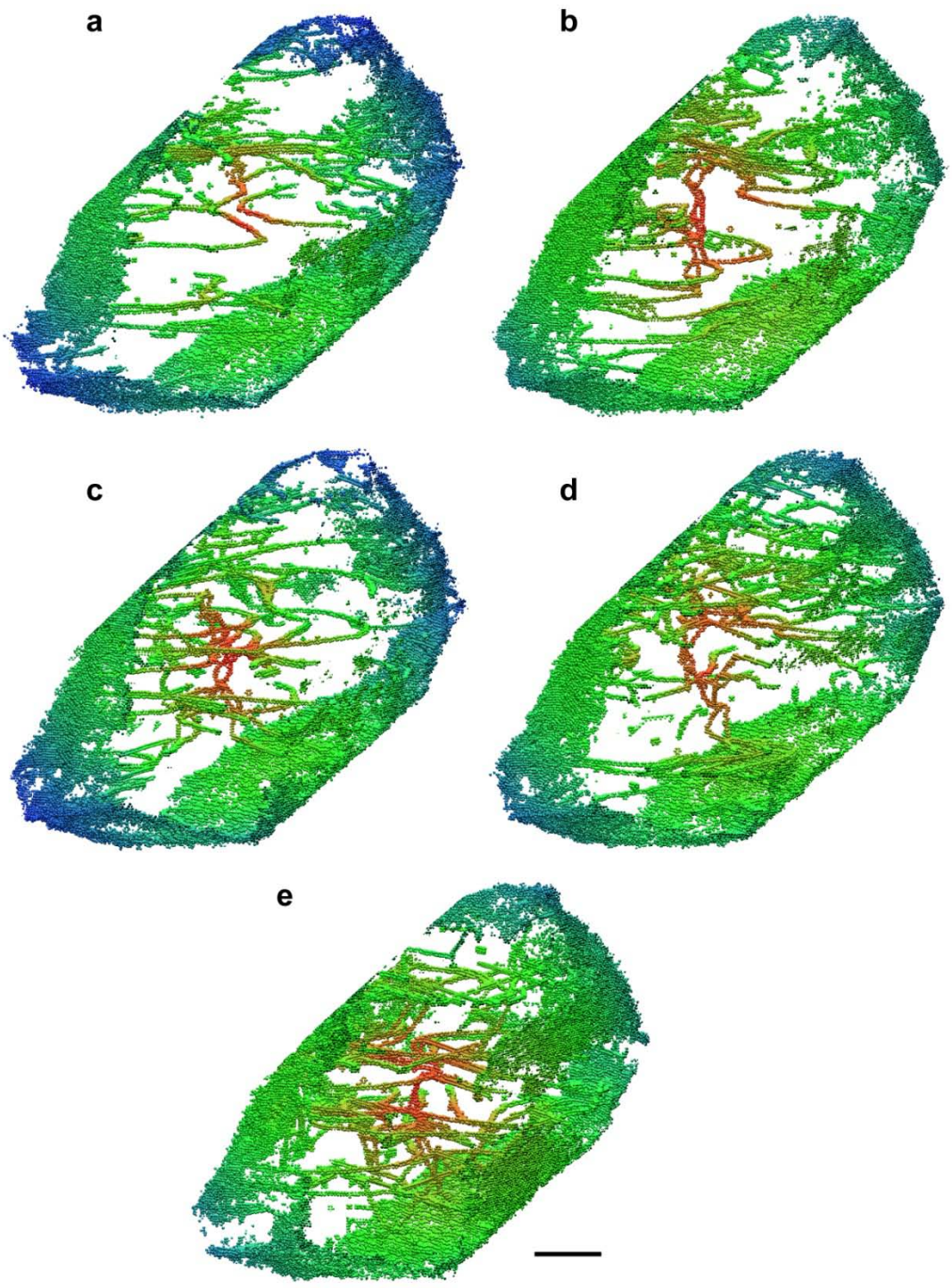

Figure 4.6. Atomic view of a representative grain in NT samples with grain size d=20 nm under 10% strain. (a) λ=0.83 nm. (b) λ=1.25 nm. (c) λ=2.08 nm. (d) λ=2.50 nm. (e) λ=6.25 nm. The coloring is based on the distance of atoms to the center of the grain. The scale bar in (e) is 5 nm.

Figure 4.7 shows direct evidence that dislocations are nucleated from twin-GB junctions in the sample with grain size d=20 nm and TB spacing λ=1.25 nm. Figures 4.7a and b show the curved dislocation structures in NT grain which is the same as that in Fig. 4.4. These figures clearly show that dislocations are nucleated at the intersection between GBs and TBs, and then glide along the TBs. Figures 4.7c and d capture the top views of the cross-sections keyed in Fig. 4.7a.

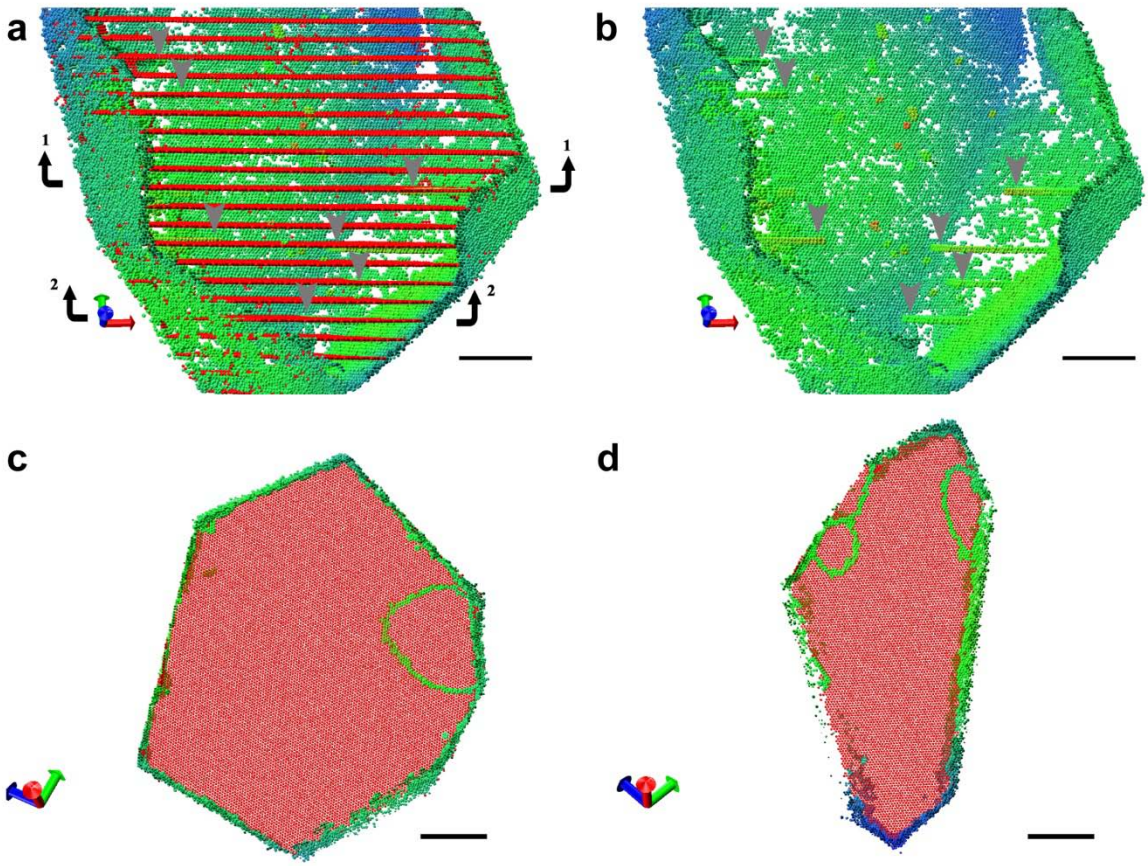

Figure 4.7. Dislocation nucleation in a representative grain in NT Cu with d=20 nm and λ=1.25 nm. Atomic views of dislocation structures (pointed by gray arrows). (a) TBs are painted in red. (b) TBs are invisible. (c) and (d) show top views of the cross-section marked by 1 and 2 in (a), respectively. The scale bars are 5 nm.

To confirm that the same strength softening phenomenon also exists in Q3D simulations, we have also performed simulations with columnar grain structures. Samples

with average grain size d=70 nm and TB spacing λ=2 nm, 5 nm, 10 nm, 15 nm, 20 nm, and 25 nm are considered. The same transition from motion of discrete dislocations intersecting with twin planes to that of partial dislocations parallel to the twin planes is observed as the TB spacing is reduced, see Fig. 4.8.

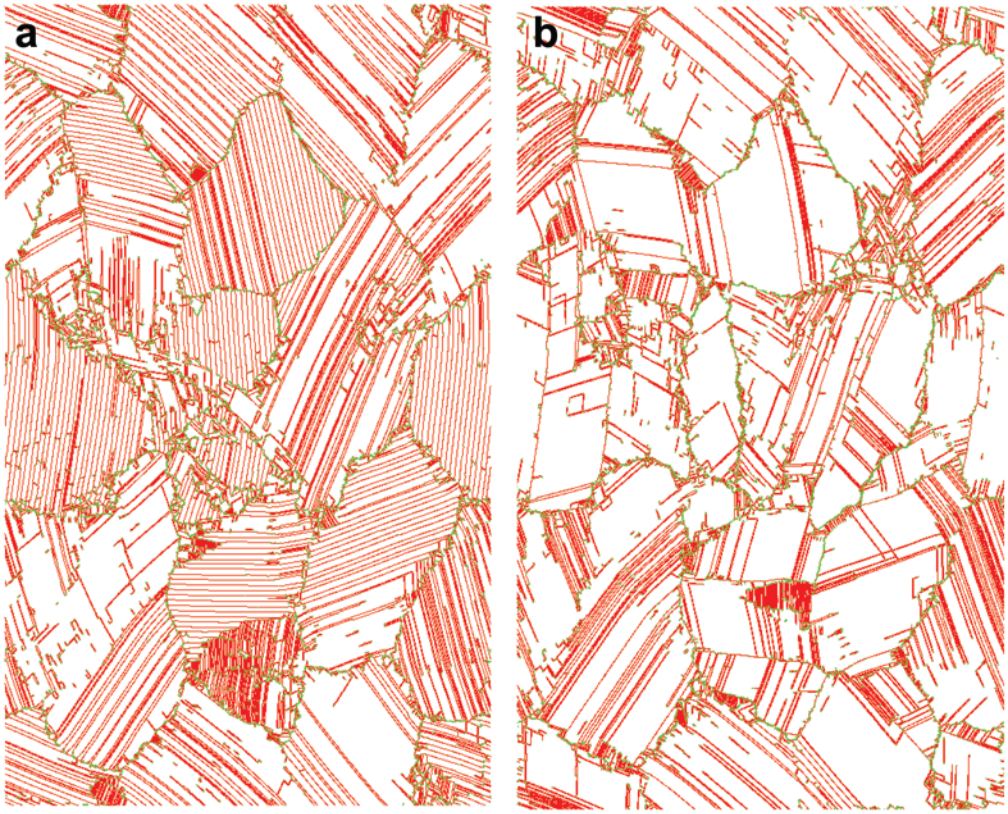

Figure 4.8. Deformation patterns from Q3D simulations for NT samples with different TB-spacing at 15% strain (scale bar: 5 nm). (a) λ=2 nm. (b) λ=25 nm.

Interestingly, it is noted that the transition happens at different values of TB spacing in samples with different grain sizes, and the corresponding maximal strengths of the material are also distinct. We will next investigate theoretically why dislocation nucleation at GB-TB intersections would lead to the softening of material below a critical TB spacing.

The strength of crystalline metals is controlled by both initial defects (mainly dislocations) and the capability of the material to nucleate new defects to carry plastic deformation. In NT Cu, plastic strains by pre-existing dislocations may be estimated as $\varepsilon=\rho_0 bd/M$ [29]. Taking the initial dislocation density $\rho_0 \sim 10^{14}$ m^{-2} in samples with λ=4 nm, the magnitude of the Burgers vector for Shockley partial dislocations in Cu b=0.147 nm, grain size d=500 nm, and M=6 to be twice the Taylor factor due to the directionality of partial dislocations, we obtain roughly a 0.1% of plastic strain by initial dislocations if those dislocations seen under transmission electron microscopy are mobile in nature. The pre-existing dislocations could consequently influence the 0.2% yield strength and hence play a significant role in the experimentally observed strength softening as the TB spacing decreases. MD simulations of nanoindentation testing [96] also enforce the conjecture that pre-existing defects in twin structures could cause strength softening. In our large-scale MD simulations, however, the samples are initially dislocation-free and subsequently exhibit a rapid increase in dislocation density to $\sim 10^{16}$ m^{-2} during plastic deformation (see Fig. 4.9). Such rapid increasing of dislocation density is comparable to the experimental observation that dislocation density increased from $\sim 10^{14}$ m^{-2} to $\sim 10^{16}$ m^{-2} as strain is increased to about 20% in the NT Cu sample with λ=4 nm [29].

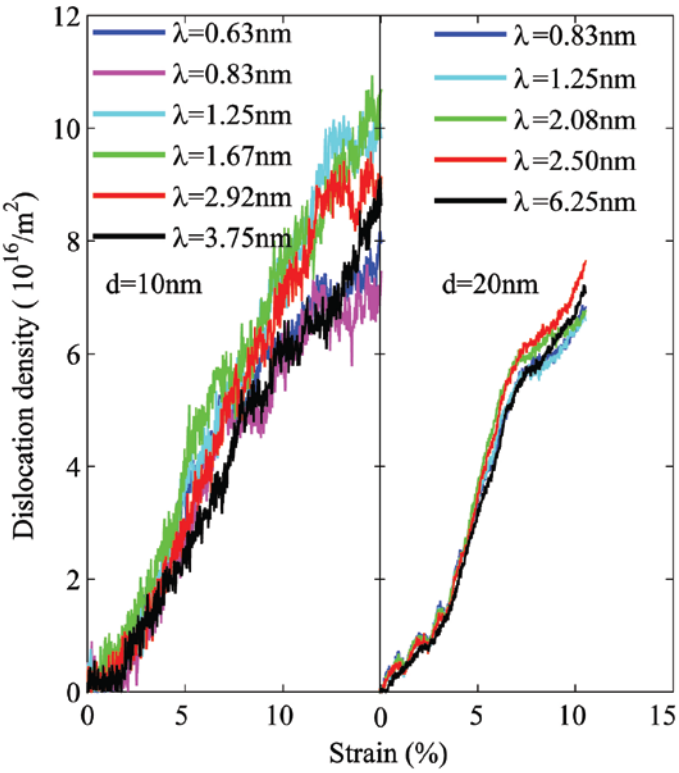

Figure 4.9. Dislocation density versus strain in different samples with mean grain size of *d*=10 nm and 20 nm.

The present simulations have provided a number of key insights into the mechanism of strength softening in NT Cu: (1) an initially dislocation-free NT metal exhibits strength softening below a critical twin thickness; (2) in the strength softening regime, dislocation nucleation occurs primarily at the GB-twin intersections; (3) there exists significant stress concentration at the GB-twin intersection, which is demonstrated by FE analysis shown in Fig. 4.10.

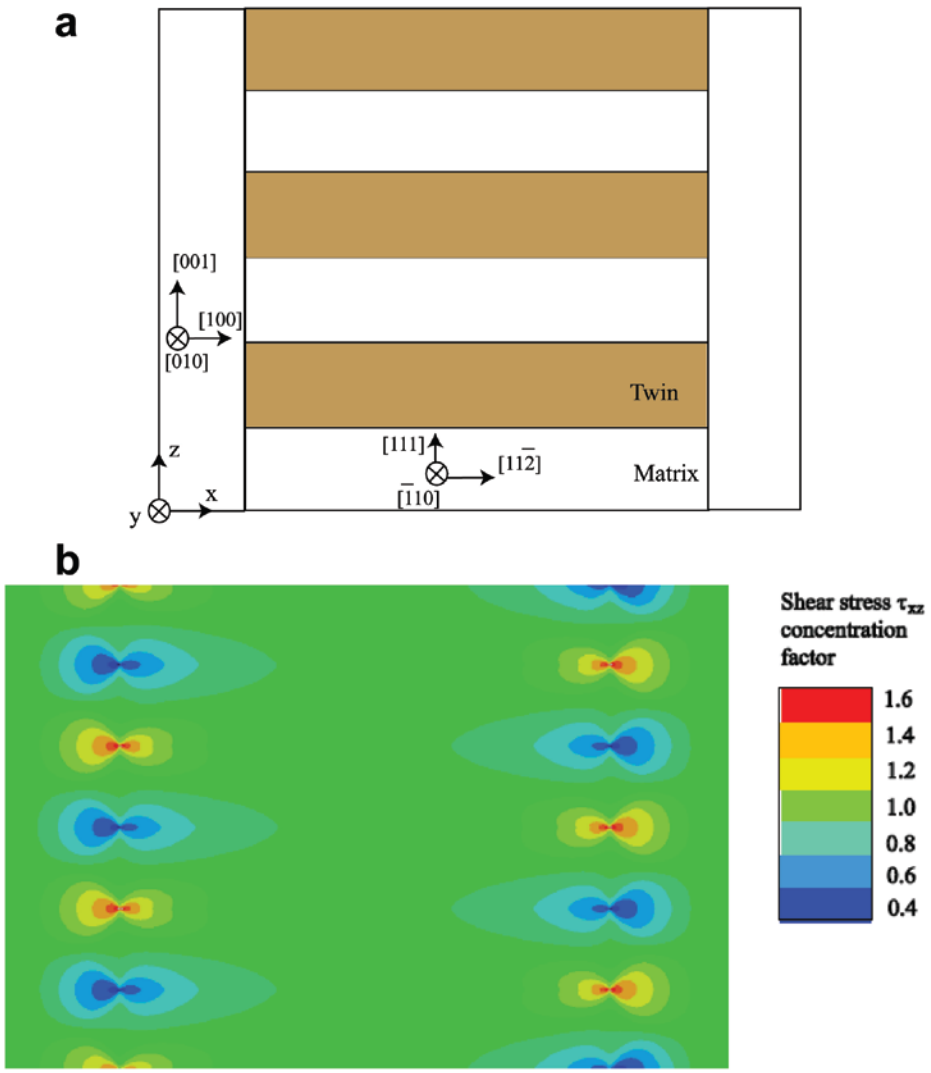

Figure 4.10. FE analysis of stress concentration at the junction of twin planes and GBs by anisotropic elasticity in Cu. (a) Schematic illustration of one simulated cell. Alternative matrix and twin layers are bounded by a crystal with different orientation. The sample is subjected to shear stain ε_{xz}. Periodic boundary condition is used. (b) Shear stress contour τ_{xz}. Stress concentration is clearly seen at the junction of TBs and GBs.

4.2.3. Kinetic model of dislocation nucleation

Due to the stress concentration at the intersection between twin planes and GBs (see Fig. 4.10), and also from our MD simulation results that the majority of emission of dislocations came from intersecting lines by twin planes and GBs (see Figs. 4.4a, 4.4b

and 4.7a-d), we can assume that these intersection lines serve as possible sources. The number of sources per matrix-twin pair N_{sg} and the associated volumetric source density ρ_{sg} are

$$N_{sg} = \alpha \frac{d}{b}, \qquad \rho_{sg} = \frac{\alpha}{b\lambda d}, \tag{4.1}$$

where b is the magnitude of the Burgers vector for Shockley partial dislocations, and α is an efficiency constant indicating the fraction of atoms that could be counted as effective emission sites, with $\alpha = 1$ being the upper bound. Since each emission in the matrix-twin pair will give rise to a plastic strain of b/λ, the macroscopic strain rate $\dot{\varepsilon}$ is thus given as

$$\dot{\varepsilon} = N_{sg}\, p_{act}\, \beta \frac{b}{\lambda} = \alpha\beta \frac{d}{\lambda} \nu_D \exp\left(-\frac{\Delta U}{k_B T}\right) \exp\left(\frac{S\tau V^*}{k_B T}\right) \tag{4.2}$$

where p_{act} is the probability that a given source is activated within a unit time, which is proportional to the Debye frequency ν_D, and a function of the activation energy ΔU, the applied shear stress τ and activation volume V^*, S is a factor representing local stress concentration and geometry, β is a geometrical factor accounting for the Taylor factor and the contribution from all possible emission system, k_B and T the Boltzmann constant and temperature. Since both α and β are on the order of unity, we take $\alpha\beta = 1$ for simplicity. The dependence of flow stress on both twin thickness and grain size is

$$\tau = \frac{k_B T}{S V^*} \ln\left[\frac{\lambda}{d}\frac{\dot{\varepsilon}}{\nu_D} \exp\left(\frac{\Delta U}{k_B T}\right)\right] \tag{4.3}$$

The above equation can be reorganized as

$$\tau = \frac{\Delta U}{SV^*} - \frac{k_B T}{SV^*} \ln\left(\frac{d}{\lambda}\frac{\nu_D}{\dot{\varepsilon}}\right) \tag{4.4}$$

The first term in the right hand side of Eq. (4.4) can be regarded as the athermal shear resistance and the second term is due to thermal softening. If multiplying the Taylor factor on both sides of Eq. (4.4), we obtain the normal stress under uniaxial tension of polycrystalline NT metals.

We also explain here how the parameters in Eq. (4.4) are determined. The Debye frequency is given as

$$\nu_D = \left(\frac{3N}{4\pi V}\right)^{1/3} v_s \tag{4.5}$$

where N/V is the number density in Cu, and v_s is the sound speed in Cu, which is about 4760m/s. We obtain $\nu_D = 1.3\times10^{13}/s$. In fitting with MD simulation results and experimental data based on Eq. (4.4), as shown in Fig. 4.11, we have used a fixed number $k_B T / SV^* \approx 200\,\text{MPa}$ with only one adjustable parameter ΔU . It is found that an activation energy of $\Delta U \approx 18.3 k_B T \approx 0.46\,\text{eV}$ allows to fit the MD simulation data [75] for both *d*=10nm and *d*=20nm, and $\Delta U \approx 40.4 k_B T \approx 1.0\,\text{eV}$ leads to a good match with experimental data [29]. The lower activation energy in our MD simulations is consistent with previous findings [169] that dislocation activation energy is lower at higher stress levels. The corresponding athermal shear resistances from MD samples and experiments are about 3.66 GPa and 8.08 GPa, respectively. Both are close to the ideal shear strength estimated as ~*G*/10, *G*=48 GPa being the shear modulus of Cu. The higher athermal shear resistance in experiments than that in MD simulations may result from the more severe stress concentration and higher GB energy in the MD samples, in comparison to the more

relaxed and lower energy GBs after twin formation in the electro-deposited experimental samples. Note that the coefficient S in Eq. (4.4), should be approximately equal to K_t/M, where K_t is the local stress concentration factor of about 1.5 (see Fig. 4.10) and $M=6$ is twice the Taylor factor due to the directionality of leading partial dislocations. With $k_BT/SV^* \approx 200\,\text{MPa}$, we have assumed an activation volume of $V^* = 2.4\Omega_0$, Ω_0 being the atomic volume of Cu, which falls in the range estimated in the literature [170]. Also, we note that the real jumping frequency for dislocation emission should be lower than ν_D because dislocation emission usually involves the collective jumping frequency of several atoms in the activation volume V^*. Since a minor change in ΔU will give rise to huge difference in the bracketed term in Eq. (4.4), the change in ν_D is expected to have little influence to our fitting parameters given above.

Figure 4.11 shows a comparison of the yield strength of NT UFG Cu from experimental data, the model predictions based on Eq. (4.4) and our MD simulation results. The softening behavior seen in the MD simulations below a critical TB spacing is well captured by the model. For a given grain size *d*, the junction by the τ versus λ curve from Eq. (4.4) and the Hall-Petch relation indicates where onset of strength softening occurs in a NT metal, provided that the Hall-Petch relation remains valid for TB spacing as small as several nanometers. As shown in Fig. 4.11, both simulations and the theory consistently show that dislocation nucleation governs the softening in NT metals, and that the onset of softening depends on the grain size: the smaller the grain size, the smaller the critical TB spacing, and the higher the maximal strength of the material. For samples with grain size *d*=20 nm and λ≈2-4 nm, we predict a tensile yield strength around 2 GPa in NT Cu.

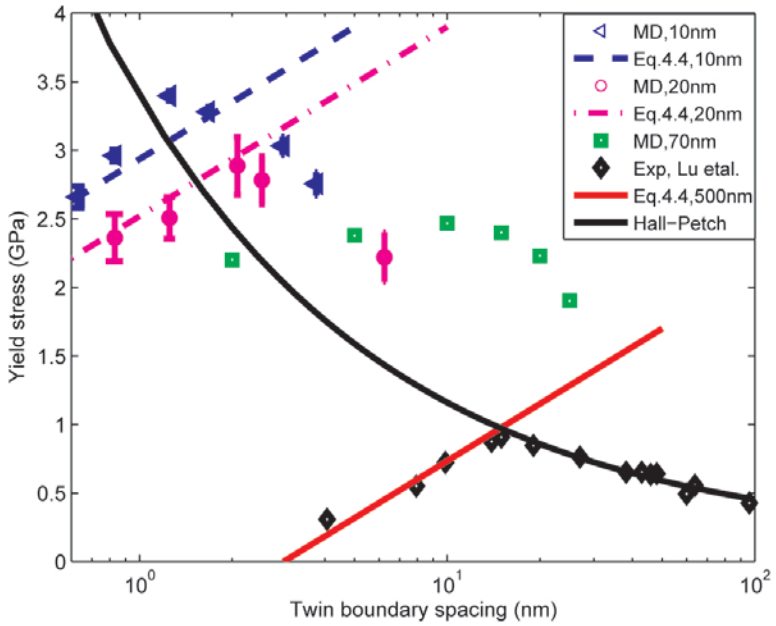

Figure 4.11. Yield stress of NT Cu as a function of TB spacing at different grain sizes. Experimental data [29] in the strength increasing region is fitted to the Hall-Petch equation $\sigma_y=\sigma_0+k\lambda^{-1/2}$, where σ_0=127.8 MPa, k=3266 MPa·nm$^{-1/2}$ and λ is TB spacing in nm. Simulation results for yield stress (taken as the averaged flow stresses at strains larger than 6%) for d=10 nm, 20 nm (at strain rate of 2×10^8 /s and temperature of 300 K), and experimental data for d=500 nm (at strain rate of 6×10^{-3} /s and temperature of 300 K), are shown together with the corresponding fitted curves from Eq. (4.4). The Q3D simulation results for d=70 nm (at strain rate of 2×10^8 /s and temperature of 300 K) are shown but not fitted since Eq. (4.4) is based on dislocation nucleation in 3D NT metals.

4.2.4. Recent extension of kinetic model

Recently, Wei [172] expressed thermally-activated dislocation nucleation frequency in more accurate manners, and extended the above kinetic model to the following equation,

$$\frac{\tau}{\phi}=\tau_0-\frac{k_BT}{V^*}\ln\left(\frac{\beta\pi}{2}\frac{\nu_D}{\dot{\varepsilon}}\frac{d}{\lambda}\sqrt{\frac{\Omega_0}{V^*}}\right) \tag{4.6}$$

where τ is the critical resolved shear stress, τ_0 is the friction stress, ϕ is a factor related to the stress concentration and crystallographic texture, β is a geometric coefficient, and Ω_0 is the atomic volume. Combining Eqs. (4.6) and (2.4), Wei also obtained the strain-rate sensitivity as a function of mean grain size and TB spacing,

$$\frac{1}{m} = \frac{\tau_0 V^*}{k_B T} - \ln\left(\frac{\beta\pi}{2}\frac{\nu_D}{\dot{\gamma}}\frac{d}{\lambda}\sqrt{\frac{\Omega_0}{V^*}}\right) \tag{4.7}$$

where $\dot{\gamma}$ is shear strain rate. This expression shows qualitative agreement with experimental observations that the rate sensitivity m increases as the TB spacing λ decreases.

Considering detwinning as collective motion of twinning partials [53], Wei [172],[173] treated nanoscale twins as Eshelby's inclusions with a eigenstrain e^T, regarded detwinning as a phase transformation of inclusions, and derived an energetic model as follows

$$\tau = \tau_0 + \frac{\alpha\pi}{8}\frac{2-\nu}{1-\nu}\frac{\lambda}{d}\mu e^T - \frac{2\gamma_{\mathrm{TB}}}{\lambda e^T} \tag{4.8}$$

where α is a constant between 0 and 1, μ is the shear modulus, ν is the Poisson ratio, and γ_{TB} is the TB energy. The second term on the right hand side of Eq. (4.8) represents the driving stress related to the elastic energy of nanoscale twins (equivalent as inclusions), and the third term corresponds to the change in interfacial energy. The predictions from Eq. (4.8) are in good agreement with the experiment results.

Most recently, the scaling law (Eq. (4.4)) has been also involved in a discrete twin crystal plasticity constitutive model [171] to describe the contribution of dislocation nucleation, so that the FE simulations based on this model success in predicting softening

trend and strengthening-softening transition, which are consistent with the experimental results [29].

4.3. Deformation in polycrystalline nanotwinned copper with columnar grains

4.3.1. Experimental studies

The research group of Prof. Ke Lu and Lei Lu [174],[175] recently prepared high-purity NT columnar-grained Cu by means of direct current electrodeposition from an electrolyte of $CuSO_4$. Figure 4.12a shows the plan-view scanning electron microscopy (SEM) images of the as-deposited sample, where numerous polycrystals separated by clear and sharp GBs can be observed. The grain sizes exhibit a distribution from 1 to 6 μm with an average grain size of ~3 μm (see Fig. 4.13a). The cross-section SEM observations in Fig. 4.12b show that these grains are columnar in shape and further subdivided into high density parallel nanoscale twin lamellae with most TBs parallel to the deposition plane. Statistics of twin thickness λ based on the transmission electron microscopy images reveals an average twin thickness of ~30 nm (see Fig. 4.13b). The electron backscatter diffraction analysis indicates that the as-deposited NT Cu sample has a strong {111} out-of-plane texture, as shown in the inverse pole figure of the growth directions of the grains (see the inset of Fig. 4.12a).

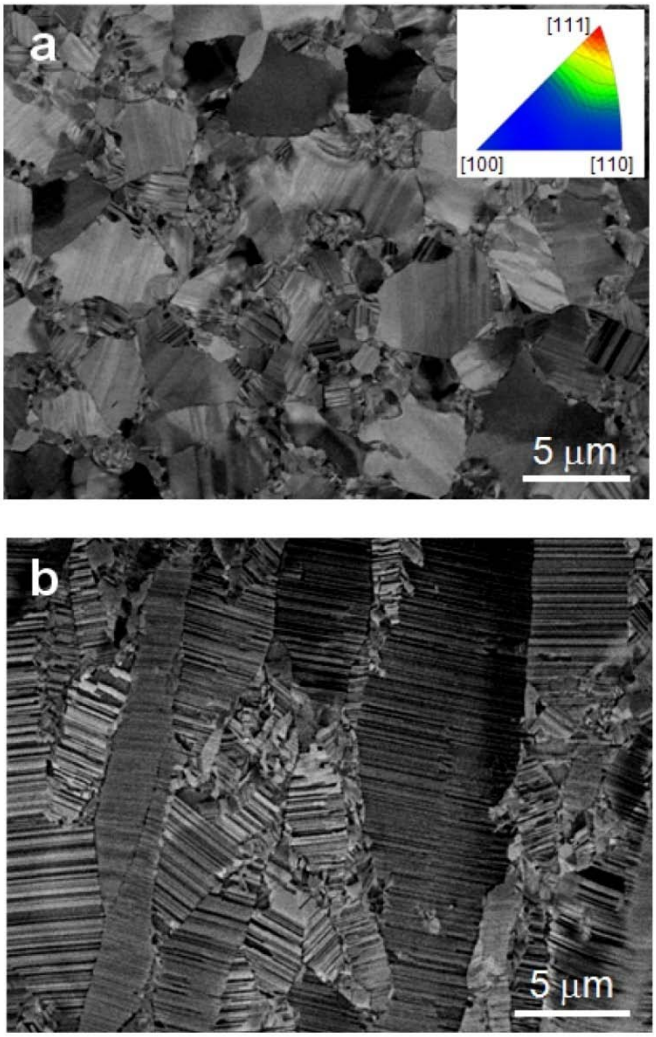

Figure 4.12. SEM images of the as-deposited Cu sample. (a) Plane view. (b) Cross-section view. The images reveal that the sample is composed of micro-sized columnar gains with high density of nanoscale twins. Most TBs are parallel to the deposition plane. The inset in (a) shows the inverse pole figure of growth directions (GD) of the grains based on EBSD measurement, which shows the significant {111} out-of-plane texture. (Courtesy of Prof. Lei Lu and Dr. Zesheng You)

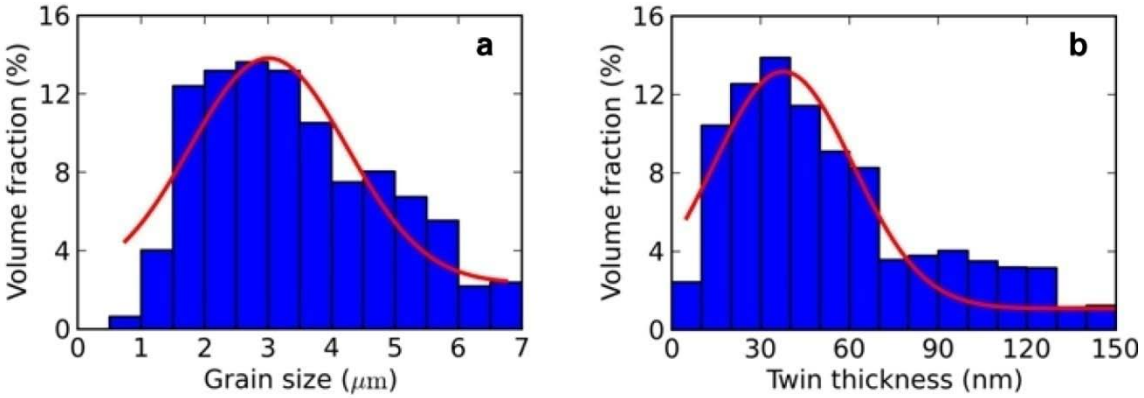

Figure 4.13. Characterization of the representative specimen used in the experiments [175]. (a) Histogram of grain sizes. (b) Histogram of twin thicknesses. The grain sizes in (a) are determined on the plane-view SEM images while the twin thicknesses in (b) from cross-section TEM observations. (Courtesy of Prof. Lei Lu and Dr. Zesheng You)

After successfully synthesizing NT columnar-grained Cu, Lu et al. [175] conducted uniaxial compression at strain rate of 1×10^{-3} s^{-1} along different directions oriented by 90°, 0° and 45° with respect to the TB. Figure 4.14a shows the stress-strain curves of columnar-grained NT Cu that exhibit a strong dependence on the loading directions. For Cu samples tested with the compression axis oriented at 90° and 0° with respect to the TBs, the measured yield stresses are 598 ± 31 MPa and 463 ± 16 MPa, respectively. Both samples exhibited only minor work hardening capacity. In contrast, compression tests with the loading axis oriented at 45° to TBs results in a much lower yield stress of 230 ± 19 MPa, but accompanied by substantial work hardening. Evidently, Cu samples with preferentially oriented twins show substantially anisotropic deformation behavior at different loading directions with respect to TBs. Figure 4.14a also shows the stress-strain curves from the crystal plasticity modeling (see details in [175]), which are in excellent agreement with experimental measurements.

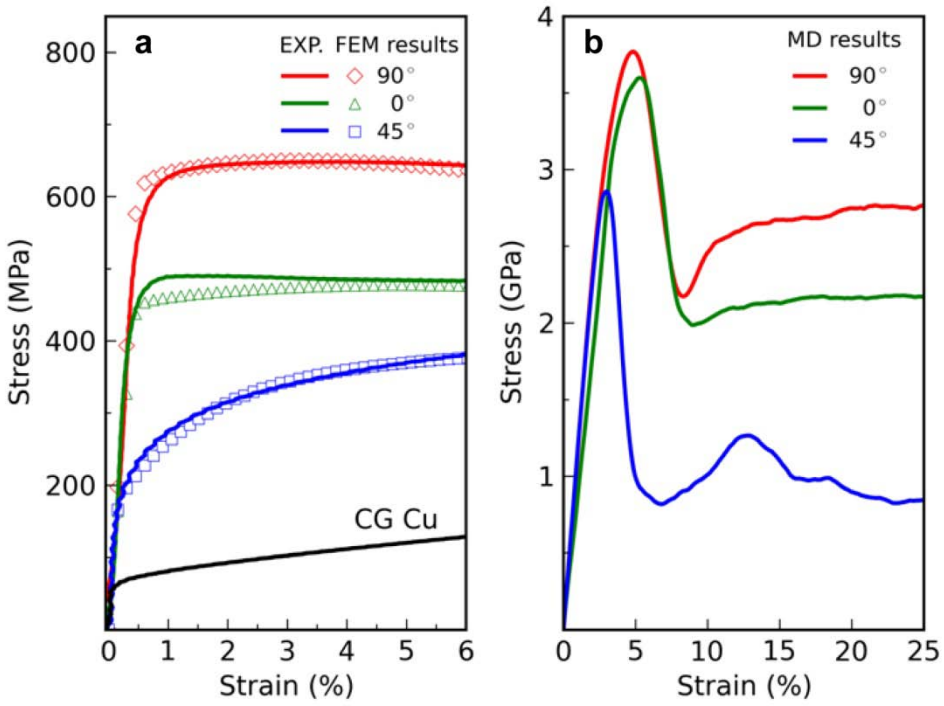

Figure 4.14. Stress-strain curves for columnar-grained NT Cu with compression axis oriented at 90°, 0° and 45° with respect to TBs [175]. (a) True stress–strain curves from experiment (line data) and crystal plasticity model (symbol data). (b) Stress-strain curves from MD simulations. (Courtesy of Prof. Lei Lu and Prof. Ting Zhu)

4.3.2. Atomistic simulations

To investigate the underlying deformation mechanism of columnar-grained NT bulk Cu, we carried out large-scale MD simulations for mimicing their uniaxial compression. The simulated sample consists of four columnar grains with high density of twins. The mean grain size is about 50 nm, and the sub-grain twins have a thickness of 5 nm. These characteristic sizes are directly scaled down from the experiments. The whole system contains 25.5 million atoms. The sample is $[1\,\bar{1}\,\bar{1}]$-textured, and four grains have in-plane orientations of 0°, 30°, 60° and 90° relative to a horizontal axis (i.e. x axis), so that all the GBs are of high-angle type. The system is initially equilibrated for 500 ps at 300 K and

then subjected to three kinds of loadings (illustrated in Fig. 4.15): (1) 0° compression, (2) 90° compression, and (3) 45° compression, respectively. These loading conditions are accomplished through stepwise straining [151] at a constant engineering strain rate of 2×10^{8} s^{-1}. Since the strain rate used in MD simulations is 10 orders of magnitude higher than that in experiments, the flow stresses from MD simulations are typically larger than those from experimental measurements.

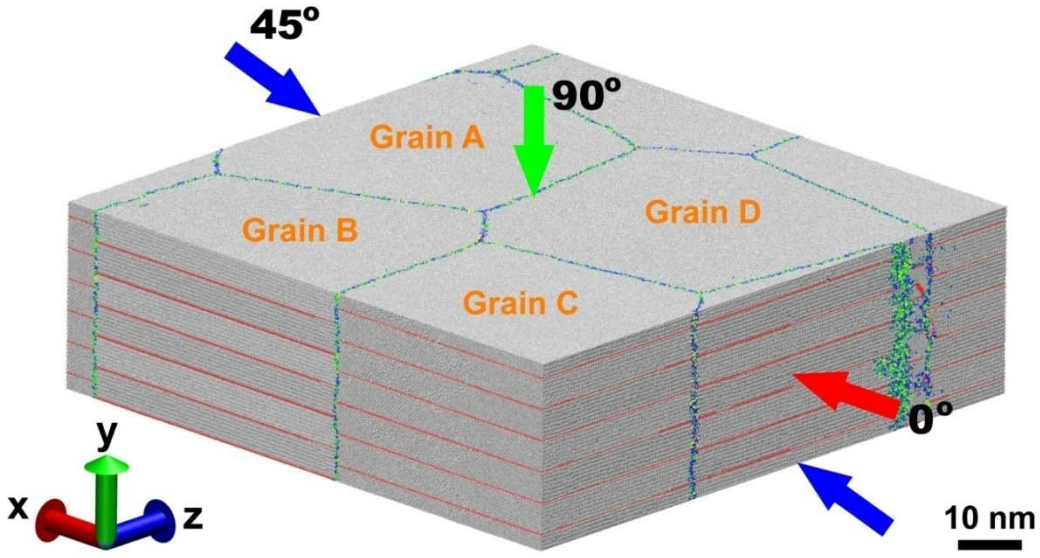

Figure 4.15. Atomic configuration of the simulated samples. The directions of three loading modes (90°, 0° and 45° compression) are indicated by the green, red and blue arrows, respectively. Each columnar grain is also labeled by an orange index. The x, y, z axes within the matrix of grain A are oriented in the crystallographic directions of [1-12], [1-1-1] and [110], respectively. Grains B, C and D are rotated counter-clockwise along the [1-1-1] direction (y axis) by 30°, 60° and 90°, respectively.

For the 0° and 90° compression cases, the uniaxial loading conditions are realized by relaxing the simulation cell size in two other directions using Berendsen barostat [139]. The 45° compression case is regarded as a combination of bi-axial compression and pure shear. Throughout simulations, periodic boundary conditions are applied in all three

directions. During simulations, we used the EAM potential [124] to compute the interatomic forces, the Nose-Hoover thermostat [140] to maintain constant temperature, and multiple-time-step algorithm [128] for time integration. To visualize and identify defects during plastic deformation, we used the local crystalline order method [156]. In addition, another coloring scheme (referred to as the position-based coloring) is used to generate 3D effects, where the colors represent the distance of atoms from the centre of the simulated grain.

Figure 4.14b shows the stress-strain curves from MD simulations of columnar grained NT Cu with mean grain size of 50 nm and twin thickness of 5 nm. The peaks of these stress-strain curves correspond to dislocation nucleation in the initially dislocation free samples. Once there are enough dislocations to accommodate the imposed deformation, the stress drops to a characteristic lower level associated with the operative deformation mechanisms. Accordingly, we define the flow stress as the average stress beyond 7.5% strain, a level that sufficiently bypasses the initial stage of deformation controlled by dislocation nucleation. Clearly, the MD simulation results also confirm the significant anisotropic plastic deformation behavior of columnar-grained NT Cu under different loading directions. The ratios of flow stress in Fig. 4.14b in 90° compression (σ_{90}) to that in 0° compression (σ_0) and in 45° compression (σ_{45}) are 1.23 and 2.65, respectively, which are quantitatively consistent with experimental values in Fig. Fig. 4.14a (σ_{90}/σ_0 = 1.29, σ_{90}/σ_{45} = 2.6).

4.3.3. Anisotropic mechanical behaviors

The anisotropic mechanical behavior of metals and alloys has been previously observed; various causes have been proposed, such as crystallographic texture [176],

precipitates [177], latent hardening [178] and deformation-induced dislocation boundaries [179],[71304484]. Specially, during 1990s, the similar phenomenon was also observed in poly-synthetically twinned (PST) TiAl alloys. It was found that the flow behaviors of PST TiAl alloys with twin lamella are strongly dependent on the orientation (i.e. the angle between TBs and the loading axis) of the lamellar structures [181]-[188]. Such plastic anisotropy is attributed to the activation of dislocations with different slip modes. For the as-deposited NT pure Cu without prior strain history, one possible explanation is the pre-existing {111} out-of-plane texture. However, the conventional Taylor model [189], which is useful in describing textural anisotropy [176], reveals a Taylor factor of 3.338 for 90° compression, 3.169 for 0° compression, and 2.987 for 45° compression based on the measured texture. This corresponds to stress ratios of σ_{90}/σ_0 = 1.05 and σ_{90}/σ_{45} = 1.12, which are much smaller than the experimental and simulation values. Therefore, the substantial anisotropy in the yield stress and strain hardening in NT Cu must be caused by other factors.

To understand the origin of the anisotropic yield stress and strain hardening, Prof. Zhu et al. [175] conducted crystal plasticity modeling for determining the dominant active slip systems for each loading direction. They employed a rate-dependent crystal plasticity formulation that explicitly accounts for plastic shearing rates on all the {111}<110> slip systems. The dominant slip mode is then determined by the slip system with the largest plastic shearing rate. Further, the measured stress-strain data for three loading orientations are used to fit the slip resistances as a function of shear strain on all the slip systems. These results show that the slip systems in NT Cu can be classified into three categories: hard mode I (Fig. 4.16a-1, both slip plane and slip direction of the active

slip systems, i.e., Burgers vector, are inclined to TBs), hard mode II (Fig. 4.16a-2, the slip plane is inclined to TBs but the slip direction parallel to TBs), and soft mode (Fig. 4.16a-3, both the slip plane and slip direction are parallel to TBs). The slip resistances in both hard modes I and II are large, owing to the constraints of small twin spacing on dislocation glide. In contrast, the slip resistance in the soft mode is much lower, because of the less constraint imposed by the relatively large grain size. Interestingly, each slip mode (i.e., slip systems) dominates in one loading direction with respect to the TBs. That is, when the compression axis is perpendicular to the TBs (90° compression), the slip systems of hard mode I dominate. When the loading axis is parallel to the TBs (0° compression), the predominant slip systems belong to hard mode II. In the case of TBs aligned with the largest resolved shear stress (45° compression), the favorable slip systems are coplanar with the TBs and hence the soft mode with the least TB blocking prevails, leading to a low yield stress in the measured stress-strain curve.

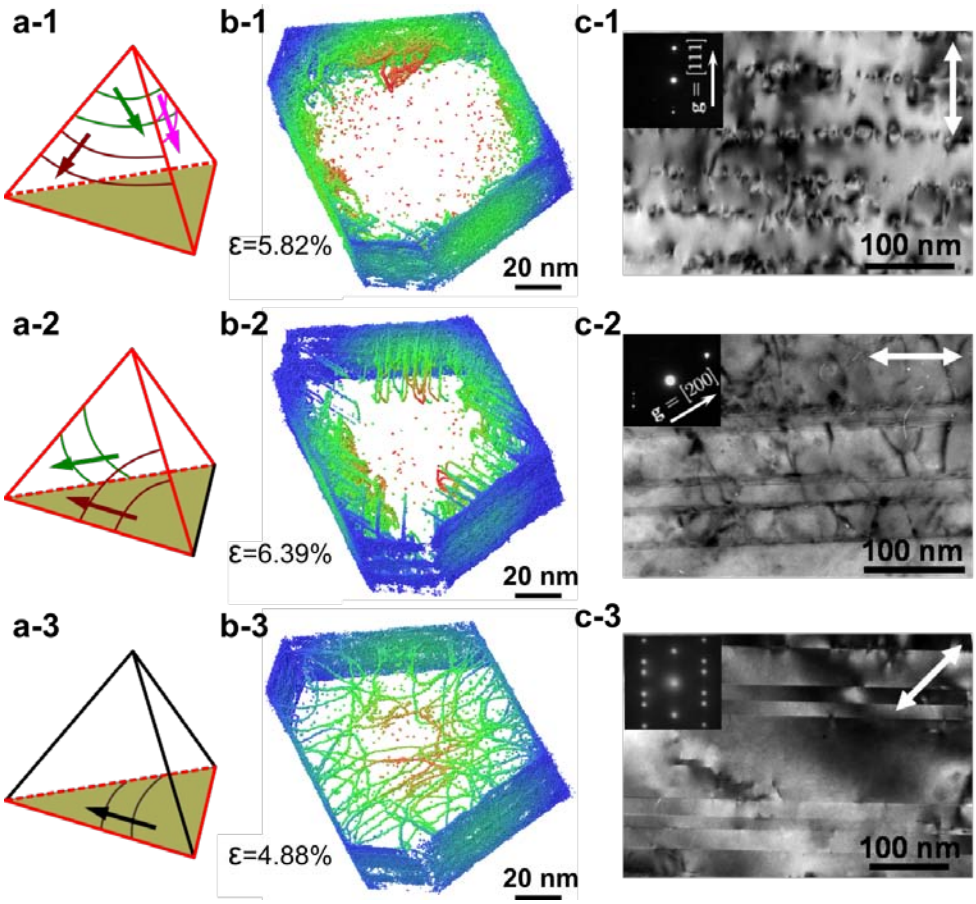

Figure 4.16. Characteristic deformation process in the columnar-grained NT Cu with compression axis oriented at 90°, 0° and 45° with respect to TBs. (a) Schematic diagrams illustrating the active slip systems for the three compression directions: a-1, 90°; a-2, 0°; a-3, 45°. (b) Dislocation microstructures revealed by MD simulation: b-1, dislocation pile-up and slip across TBs at a strain of 5.82% under 90° compression; b-2, threading dislocations nucleated from GBs and gliding in the twin/matrix lamellae at a strain 6.39% under 0° compression; b-3, partial dislocation gliding parallel to TBs and the induced TB migration at a strain of 4.88% under 45° compression. Dislocation structures are rendered in the position-based coloring. (c) TEM observations of the microstructure of samples in different loading directions: c-1, 90° compression with a strain of ~5%; c-2, 0° compression with a strain of ~6%; c-3, 45° compression with a strain of ~7%. To reveal the dislocation types more clearly, tilting experiments were carried out, and c-1 and c-2 are bright-field images under two-beam conditions with **g**=[111] (normal to TBs) and **g**=$[200]_M$, respectively. (Courtesy of Prof. Lei Lu, Dr. Zesheng You and Prof. Ting Zhu)

Moreover, the loading orientation dependence of strain hardening can also be understood in terms of the hard and soft modes of slip. In the 45° compression case, the soft mode dominates. Hence, the work hardening capacity is controlled by the grain size that is relatively large, providing enough space within the grain to facilitate strain hardening through gradual accumulation of dislocations during deformation. On the other hand, the hard modes dominate for both 0° and 90° compression. In these cases, the strain hardening is largely suppressed due to the narrow space between adjacent TBs that limits the buildup of a high density of dislocations.

MD simulations were used to probe the atomic level dislocation activities related to the orientation dependence. The active slip systems (including the slip plane and the Burgers vector) are identified in the matrix of four grains under 90^o compression, 0^o compression as well as 45^o compression (see Table 4.1), which are consistent with results from the crystal plasticity modeling. Fig. 4.16b-1 shows the dislocation structures with a compressive strain of 5.82% normal to TBs. In this loading direction, most dislocations are nucleated from the GBs in the initial stage and glide on the inclined {111} slip planes until they finally pileup against TBs, indicating that TBs are strong barriers for dislocation motion. Compared to dislocation structures in Figs. 4.16b-2 and Fig. 4.16b-3, dislocation lines in Fig. 4.16b-1 are more entangled. As the deformation proceeds, the dislocations start to cut through the TBs when the shear stress driving the incident dislocations is sufficiently large (see Figs. 4.17a and 4.18a), which were also verified by the previous MD simulations that dislocation pileup against and interaction with TBs [73],[76],[90] are the dominant deformation mechanism under straining perpendicular to TBs. Postmortem TEM observation of the sample with 90^o compression in Fig. 4.16c-1

displays a high density of dislocations accumulated along the TBs, presumably being the remnant dislocation components produced by dislocation cutting of TBs. This is consistent with the dynamic processes revealed by the MD simulation. These results provide direct evidence of TB obstruction to dislocation glide as a major strengthening mechanism, as designated by hard mode I (Fig. 4.16a-1).

Table 4.1. Activated slip systems, including full and partial dislocations in each grain in MD simulations under different loading modes. Slip system is identified via Thompson tetrahedron representation shown in Fig. 2.13.

Grain Index	Rotation Angle (°)	Slip plane, Burgers vector (Schmid factor)		
		90° Compression	0° Compression	45° Compression
Grain A	0	ABC, BA (0.272)	ABC, AC (0.408)	ACD_T,βA_T (0.500)
x:		ABC, BC (0.272)	ABD, AD (0.408)	
y:		ABD, BA (0.272)	ABC, δC (0.314)	
z:		ABD, BD (0.272)	ABD, γD (0.314)	
		BCD, BC (0.272)	BCD, αB (0.314)	
		BCD, BD (0.272)		
Grain B	30	ABC, BA (0.272)	ABD, AD (0.408)	BCD, αD (0.437)
x:		ABC, BC (0.272)	ABD, AB (0.408)	ACD_T, βC_T (0.433)
y:		ABD, BA (0.272)	BCD, CB (0.408)	ABD, γD (0.437)
z:		ABD, BD (0.272)	BCD, CD (0.408)	ACD_T, βA_T (0.433)
		BCD, BC (0.272)	ABD, γD (0.236)	
		BCD, BD (0.272)	ABD, γB (0.236)	
			BCD, αD (0.236)	
			BCD, αB (0.236)	
Grain C	60	ABC, BA (0.272)	ABC, CA (0.408)	ACD, βC (0.500)
x:		ABC, BC (0.272)	BCD, CD (0.408)	
y:		ABD, BA (0.272)	ABC, δA (0.314)	
z:		ABD, BD (0.272)	ABD, γB (0.314)	
		BCD, BC (0.272)	BCD, αD (0.314)	
		BCD, BD (0.272)		
Grain D	90	ABC, BA (0.272)	ABC, CB (0.408)	ABC, δA (0.437)
x:		ABC, BC (0.272)	ABC, CA (0.408)	ACD, βC (0.433)

y:		ABD, BA (0.272)	ABD, DB (0.408)	ABD_T, γD_T (0.437)
z:		ABD, BD (0.272)	ABD, DA (0.408)	ACD_T, βD_T (0.433)
		BCD, BC (0.272)	ABC, δB (0.236)	
		BCD, BD (0.272)	ABC, δA (0.236)	
			ABD, γA (0.236)	
			ABD, γB (0.236)	

When the loading direction was changed to be parallel to the TBs, MD simulations revealed that the GBs were still the favorable dislocation nucleation sites. However, in contrast to the 90° compression, much less dislocation pileup and slip transfer across TBs were observed. Instead, the dominant plastic deformation mechanism became propagation of individual dislocations along the inclined slip planes under the constraint by adjacent TBs, as shown in Figs. 4.17b and 4.18b. This resulted in threading segments spanning individual twin or matrix lamella with misfit segments lying in the TBs. These dislocations have hairpin-like loop configurations, as shown in Fig. 4.16b-2 from simulations. Such dislocation structure was also observed in postmortem TEM observations, as given in Fig. 4.16c-2. Detailed analysis shows that the Burgers vectors of the threading dislocations are parallel to the TBs, corresponding to the active slip systems of hard mode II (Fig. 4.16a-2). In the initial stage, the dislocations traveled far into the grain interior. As the applied strain increases, more dislocations gradually accumulate in the vicinity of GBs, and the GB regimes would take much larger plastic strain than that sustained by grain interiors [174].

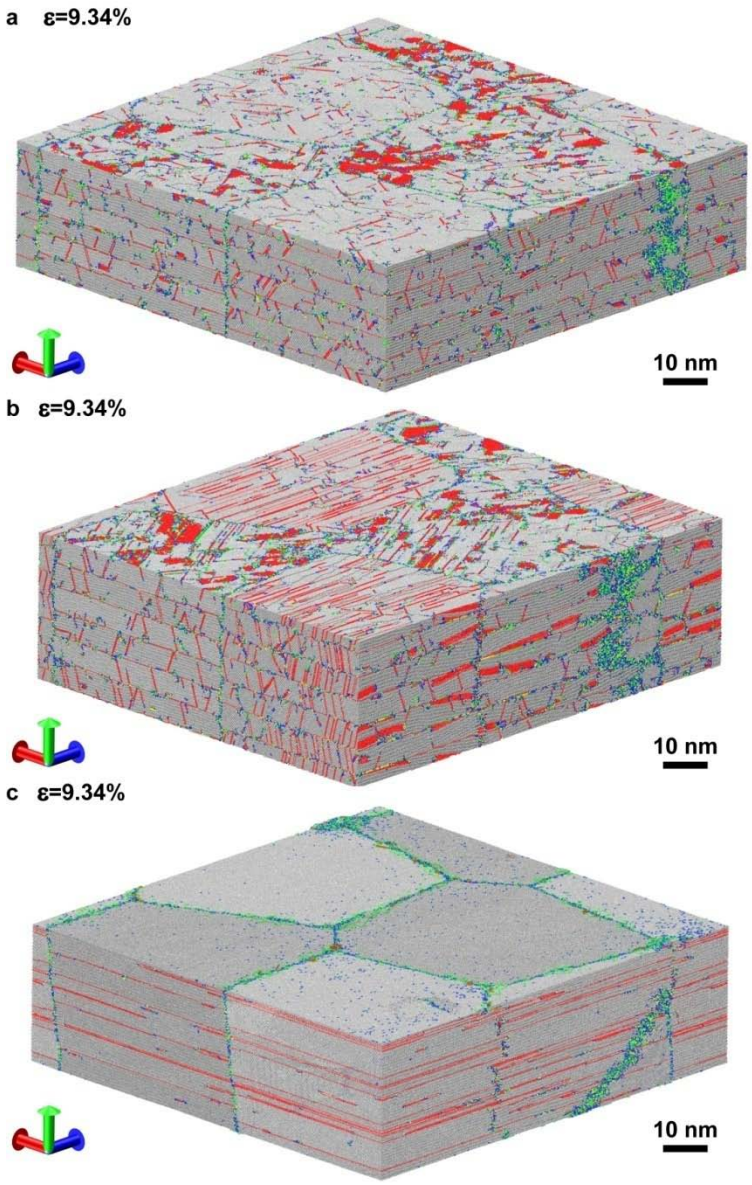

Figure 4.17. Strained atomic configurations of the simulated sample under different loading modes. a, 90° compression; b, 0° compression; and c, 45° compression. In (a), dislocations cut through TBs. Their traces remain short due to the blocking effects of TBs. In (b), threading dislocations are fully confined in the twin or matrix lamellae. Threading segments span over the whole twin or matrix regions, while leaving behind long traces of misfit segments on TBs. In (c), dislocations are nucleated at TB-GB intersections and then glide on twin planes, leading to TB migration which changes the twin lamella thickness. Here we use the coloring scheme based on the local crystalline order method.

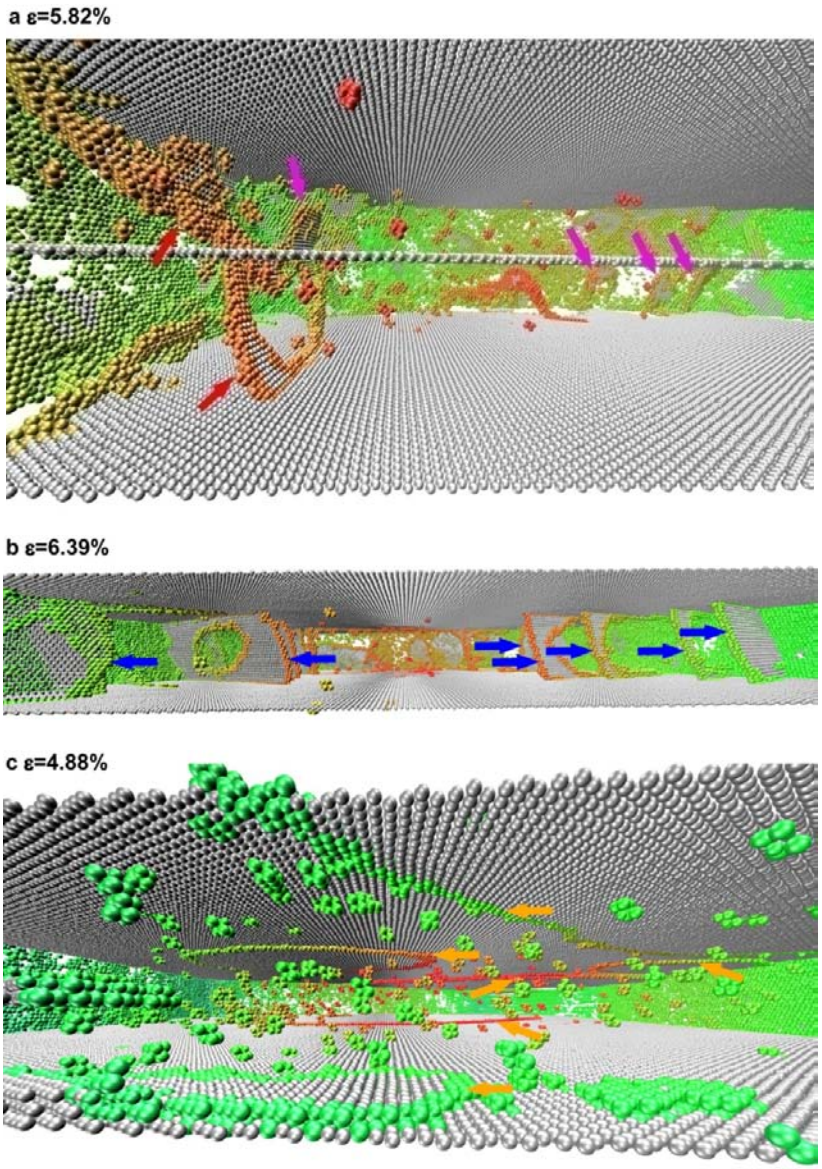

Figure 4.18. Dislocation patterns in the representative grains under different loading modes. a, 90° compression; b, 0° compression; and c, 45° compression. Herein atoms are painted by the position-based coloring. The silver atoms have hcp order, so single silver layers represent TBs, and double silver layers stand for the staking faults. In (a), dislocations nucleate at the TB-GB intersections and glide on the slip planes inclined to TBs, as pointed out by purple arrows. Dislocation cutting through the TB is marked by red arrows. In (b), threading dislocations nucleate from GBs, and then slip in the confined twin/matrix, as pointed by blue arrows. In (c), partial dislocations marked by orange arrows nucleate at the TB-GB junctions, and slip on the TBs.

For the case of 45° compression, the resolved shear stress is maximized on the twin plane, facilitating the activation of the soft mode slip. Shockley partial dislocations, nucleated predominantly from the intersection lines between TBs and GBs, glide on the twin planes, as shown by MD simulations in Fig. 4.16b-3 (and also see Figs. 4.17c and 4.18c). The successive motions of these partial dislocations lead to TB migration, which thicken or narrow the twin lamellae depending on the direction of the partial dislocation in the twin plane. TEM observations revealed that a higher density of TB ledges (debris of the partial dislocations in twin planes in Fig. 4.16c-3), in contrast to a high density of dislocations in the 90° and 0° cases. The coupled partial dislocation motion and TB migration have also been demonstrated to play a key role in the plastic deformation of NT metals in experiments [166],[190] and simulations [75],[76],[94], especially when the TBs are oriented along the planes with high Schmid factors [90],[95].

The combination of experimental, modeling and simulation studies at different scales revealed a number of new insights into the strengthening/deformation mechanisms of NT metals: Firstly, there are three distinct dislocation-based deformation mechanisms in highly oriented NT Cu. These three mechanisms, in conjunction with the conventional dislocation-dislocation interaction, constitute the deformation-based deformation mechanism map in terms of the loading direction (θ) with respect to TBs and the average twin thickness (λ), as schematically shown in Fig. 4.19. When λ is larger than 100 nm, the intra-twin dislocation-dislocation interaction, which is insensitive to the loading direction, controls the deformation. However, as λ is reduced below 100 nm, the dislocation nucleation process and the enhanced interactions between dislocations and TBs make possible the active operation of different dislocation mechanisms under

different loading directions. Secondly, it is clear from Fig.4.19 that the three deformation mechanisms can be controllably switched by adjusting the loading direction with respect to the twin planes. The intrinsic deformation process strongly influences the efficiency of TB strengthening, anisotropic yield stress and strain hardening. For the case of 90° compression, TBs provide the most effective barriers since most dislocations are hindered by TBs in their propagation paths.

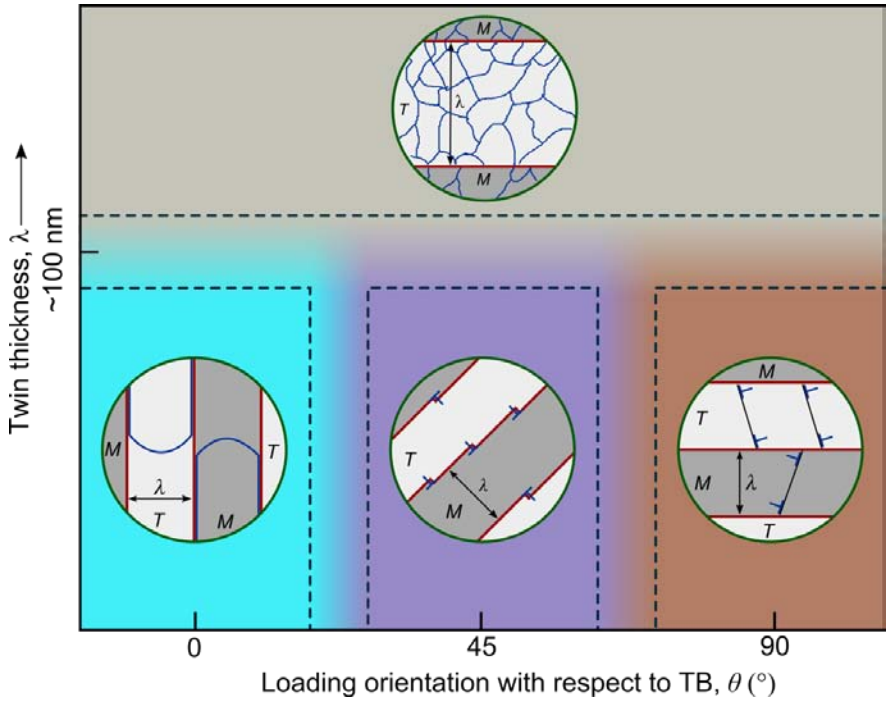

Figure 4.19. Schematic illustration of a deformation-mechanism map for NT Cu in terms of twin thickness (λ) and loading direction (θ) with respect to TBs. There are one region corresponding to intra-twin dislocation interaction when λ>~100 nm and three distinct regions when λ<~100 nm: confined threading dislocation slip (θ=0°), partial dislocation motion induced TB migration (θ=45°), and dislocation pile-up and cutting through TBs (θ=90°). (Courtesy of Prof. Lei Lu and Dr. Zesheng You)

4.4. Twin size effect of nanotwinned bulk metals

4.4.1. Hall-Petch strengthening

Based on earlier experimental [29] and computational [75] results, the yield strengths of NT Cu follow the Hall-Petch law as $\sigma_y=\sigma_0+k\,\lambda^{-1/2}$, where λ is the average TB spacing. We fitted the Hall-Petch relationship of NT and NC Cu, and obtained the fitting parameters listed in Table 4.2. The relevant data are plotted in Fig. 4.20. Two fitting parameters from experiments of NT Cu are very close to those obtained from NC Cu. It implies that the strengthening in NT Cu indeed follows the Hall-Petch law, similar to NC Cu. The material constants k from MD simulations agree with those from experiments. However, the friction stresses σ_0 from MD simulations are one order of magnitude higher than those fitted by experiments. Such high resistance to dislocations in MD simulations is due to high strain rate, small length scale and high-energy configuration. MD simulations have shown that the stresses required for screw [105] and non-screw [106] dislocations transmission through the TB are about 0.5 GPa or 1.2 GPa, respectively.

Table 4.2. Fitting parameters of Hall-Petch relationship based on the experimental and computational results.

Data source	**(GPa)**	**(GPa·nm$^{1/2}$)**
NT Cu (Exp., Ref. [29])	0.1278	3.266
NC Cu (Exp., Ref. [1])	0.1210	3.366
NT Cu (MD, Ref. [75])	1.0528	3.085
NC Cu (MD, Ref. [17])	1.2689	4.067

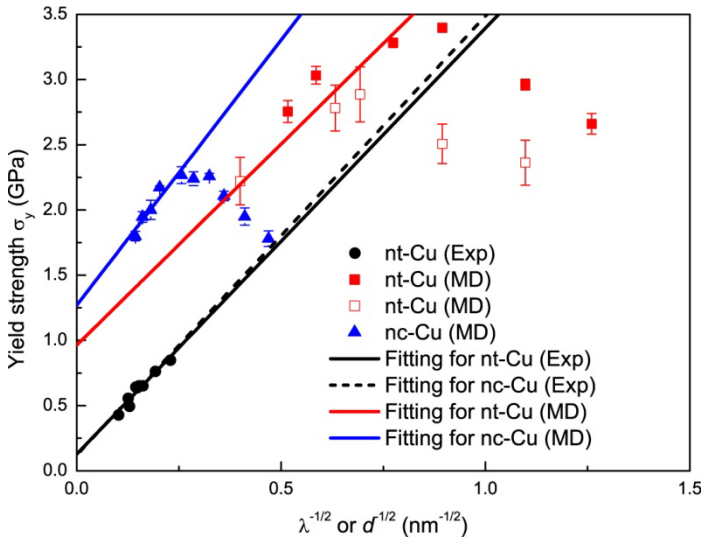

Figure 4.20. Hall-Petch relationship based on the experimental and computational results for NT-Cu (λ is the twin thickness) and NC-Cu (d is the mean grain size). Black dots come from Ref. [29], red solid and open squares from Ref. [75], and blue triangles from Ref. [17]. Black dash line is fitting curve for NC Cu in Ref. [1]

4.4.2. Confined layer slip model

In the thin films or multilayer metallic materials, where the planar interfaces provide effective barriers for dislocation motion, it has been demonstrated that there exists significant length scale dependences of the plastic deformation and interface strengthening. When the layer thickness falls below a critical value of ~100 nm, the hair-pin like threading dislocation propagation under the constraint of neighboring interfaces dominates the plastic deformation. In the present study, it is noted that the TBs perform in a manner analogous to the interfaces in multilayer metals, i.e., confine the dislocation slipping between the adjacent TBs, when compressed parallel to TBs (0° compression).

It is expected that the length scale dependence of the flow stress in NT Cu under 0° compression can also be described by the confined layer slip (CLS) model previously proposed for multilayer metals [191],[192]:

$$\sigma_y = \sigma_0 + \beta \frac{\mu b}{\lambda} \ln\left(\frac{\alpha\lambda}{b}\right) \tag{4.9}$$

where μ is the shear modulus (45 GPa for Cu), b is the Burgers vector (0.256 nm for Cu), α represents the dislocation core cutoff parameter, β is a constant combing the contributions from crystal orientation and dislocation character, σ_0 represents resistance stress without influence of interfaces ($\lambda \to \infty$), which may arise from lattice friction stress or resistance from preexisting dislocations and grain boundaries.

The data from experiments [30]-[32],[54],[174],[175] were used to get the unknown parameters σ_0, α and β. Fig. 4.20 shows that the CLS model with σ_0=72 MPa, α=0.157 and β=0.404 can well describe the variation of the yield strength with the average twin thickness ranging from 4.5 nm to ~70 nm in the NT Cu tested parallel to TB. Here σ_0 is reasonably close to the yield stress of CG Cu (~50 MPa), $\alpha \ll 1$ implies a significant dislocation core spreading or dislocation decomposition when the dislocations are deposited in the TBs after their propagation. Since most Burgers vectors of the activated dislocations are parallel to TBs, the dislocation segments deposited in the TBs are screw dislocations; therefore β can be expressed as $M \sin\theta / 2\pi$ where M is the orientation factor changing the shear stress in a activated slip system to the normal stress under uniaxial test and θ the dihedral angle between the inclined slip plane and twin plane. Using θ=70.5° and M=2.65 determined based on the orientation data from EBSD measurement, β=0.398 is very close to the fitting value.

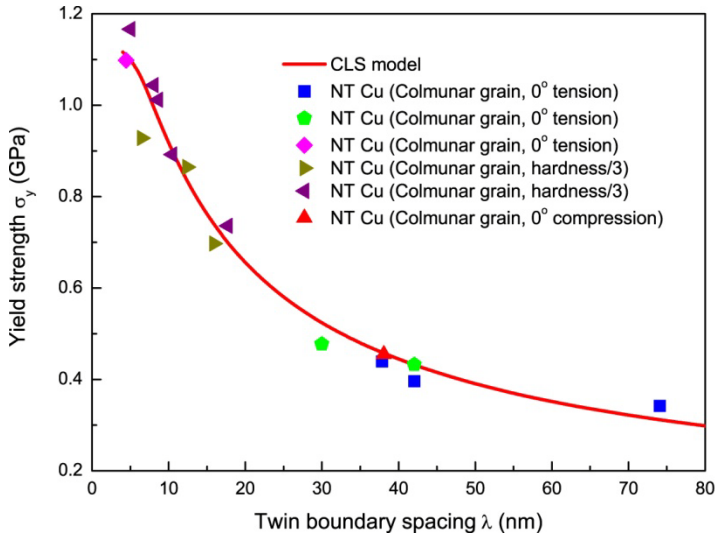

Figure 4.21. Variation of yield strength σ_y as a function of average twin thickness λ for columnar-grained Cu with preferentially oriented nanoscale twins. Blue, green, magenta, dark yellow, purple and red data come from Refs. [174],[54],[30],[31],[32],[175], respectively.

4.4.3. Twin size effect on yield strength

Figure 4.22 shows that the yield strength of columnar-grained NT Cu under 90° compression fits well to the Hall-Petch curve established by the experimental data obtained from equiaxed-grained NT Cu [29] where dislocation pile-up also dominates (see Section 4.4.1). This means that Hall-Petch strengthening ($\sigma \propto \lambda^{-1/2}$) plays a crucial role in the 90° compression. In contrast, the strength under 0° compression in this study, together with results from 0° tensile tests [54],[55] and micro-hardness measurements [31],[32] in the literature, all fall below the Hall-Petch curves as shown in Fig. 4.22. Considering the observation that the controlling deformation mechanism is switched to individual threading dislocation motion under 0° compression, the CLS model, as frequently used to model the flow stress of nanoscale thin films or multilayered materials [191],[192], is adopted. Figure 4.22 demonstrates that the CLS model can well capture

the variation of yield strength of NT Cu with twin thickness ranging from ~4.5 nm to ~70 nm for loading direction parallel to TBs (see Section 4.2.3). In the case of 45° compression, partial dislocations on the twin planes would be preferentially activated and there is almost no TB obstruction to their propagation. The flow stress in this case is expected to be controlled by dislocation nucleation at the intersections between TBs and GBs [75], with a much lower yield stress compared to the other two loading directions.

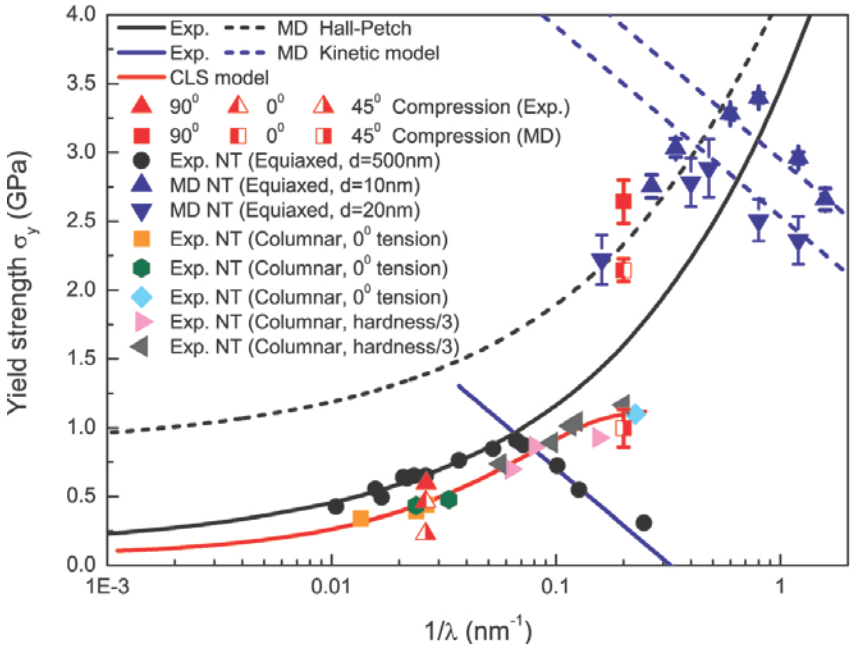

Figure 4.22. Yield stress of NT Cu (σ_y) as a function of inverse twin thickness ($1/\lambda$) showing the influence of loading direction on the efficiency of TB strengthening. For equiaxed-grained NT Cu [29],[75] with λ larger than some critical value and columnar-grained NT Cu loaded perpendicular to TBs (θ=90°), the yield stress follows the conventional Hall-Petch relationship. In contrast, when the NT Cu was tested parallel to TBs (θ=0°) [54],[55] or under nanoindentation [31],[32], the yield stress can be well described by the CLS model. For the case with θ=45°, the yield stress is much lower than the other two cases. The data [29],[75] corresponding to TB softening in equiaxed-grained NT Cu when λ smaller than some critical value is also included.

4.5. Summary

For NT bulk Cu with equiaxed grains, we have identified a dislocation nucleation governed softening mechanism in NT metals in which dislocation nucleation and storage are highly organized by the existing twins. Both the increased source density and increased TBs as storage are key to the observed strength softening in NT metals. Such softening mechanism can happen in samples with or without pre-existing dislocations. We have developed a kinetic model about dislocation nucleation from TB-GB intersections and obtained a scaling law which reveals the dependence of yield strength on two microstructural length scales (grain size and TB spacing). The simulations and the kinetic theory show that the critical TB spacing for the dislocation nucleation governed mechanism depends on grain sizes: the smaller the grain size, the smaller the critical twin spacing, and the higher the maximum strength of the material. The scaling law described by Eq. (4.4), combined with the Hall-Petch relation, predicts the critical TB spacing for the onset of softening in NT metals. Since both the Hall-Petch relation and Eq. (4.4) are non-specific to particular metals, the conclusion should be generally applicable to equiaxed-grained NT fcc metals.

During plastic deformation of the columnar-grained NT bulk Cu, we have observed three distinct dislocation-based deformation mechanisms, namely dislocation pileup and slip transfer across TBs, threading dislocation motion in the confined twin/matrix layers, and TB migration mediated by partial dislocation motion parallel to TBs. It has been demonstrated that one can switch among these deformation mechanisms by changing the loading orientation with respect to the twin planes. These results are of great interest from both fundamental and application points of view, and point to the possible means of

tailoring the nanostructure and loading for optimizing the mechanical properties of engineering materials.

Chapter 5 Deformation and Failure in Nanotwinned Copper Thin Films

5.1. Failure mechanisms of nanotwinned metals

So far, there have been only a few studies on the effects of twin size on the fracture toughness of NT metals. Recent experiments [80]-[83] have demonstrated that the twin lamellar structures can significantly enhance the fracture toughness of NT Cu. Qin et al. [80] observed ductile fracture characterized by dimple-dominated fracture surfaces. It was found that the dimple structures are produced by voids nucleating ahead of a principal crack when the overall strain reaches a critical value [80]. In fracture of NT metals, a unique feature is that the typical dimples are coarser and deeper than those appearing on the fracture surfaces of NC metals. These coarser/deeper dimples are created near the slender nanoscale twins, indicating that the highly anisotropic twin structures are effective in energy absorption and arresting crack propagation [80]. Shan et al. [193] have conducted in-situ straining experiments on NT Cu, and found that when TB spacing is larger than 30 nm, the crack path is always along a specific crystallographic plane, implying a brittle-like behavior; however, when TB spacing is reduced to below 30 nm, the fracture path no longer follows the crystallographic plane. They concluded that such transition is attributed to full dislocation slip (for λ>30 nm) switching to partial dislocation slip on TBs (for λ<30 nm).

Zhou et al. [194],[195] have performed Q3D CMD simulations of NT Ni with a pre-crack under uniaxial tension. They varied TB spacing in the simulated samples, and found that the fracture toughness dramatically increases with decreasing TB spacing [194]. During simulations, four toughening mechanisms due to the presence of TBs were observed [195]: (1) crack blunting through dislocation accommodation along TBs; (2) crack deflection in intragranular propagation; (3) daughter crack formation along TBs; and (4) curved TB planes owing to an excessive pile-up of geometrically necessary dislocations.

The above studies have indicated that the mechanisms of crack-nanotwin interactions can be beneficial to toughness. In this chapter, we therefore conduct a series of MD simulations to study interaction between a crack and TBs in NT Cu thin films, and further explore the influence of nanoscale twins on deformation and fracture of NT Cu thin films by coupling the recent experiments done by Prof. Sharvan Kumar and Prof. Seong-woong Kim.

5.2. Experimental studies

5.2.1. Characterization of fabricated thin films

So far, experiments have been limited by the lack of adequate electron-transparent area coupled with variable thickness of specimens prepared from bulk samples. Recently, the research group of Prof. Sharvan Kumar proposed a novel approach (Fig. 5.1a) to produce electron transparent metal films of uniform thickness that enable unhindered examination in the TEM of crack interaction with nanoscale twins and other microstructural features. Using such approach, they have produced NC Cu films that have uniform thickness of about 100 nm and with significant electron-transparent regions (Fig.

5.1b); the resulting grain size is in the NC regime (around 50 nm) with a fairly narrow distribution (see inset in Fig. 5.1b). They heat-treated such films in-situ in the TEM using a heating-straining single tilt specimen holder to grow the grains to 500-700 nm and to produce annealing twins in these grains, with median TB spacing less than 80 nm (Fig. 5.1c). After annealing, the individual grains and the annealing twins typically traverse the entire film thickness. They then deformed the specimen in-situ in the TEM at room temperature to produce a crack in the film, and observed how the advancing crack tip interacts with the annealing twins. The details in experimental preparation and tensile testing are described in the literature [196].

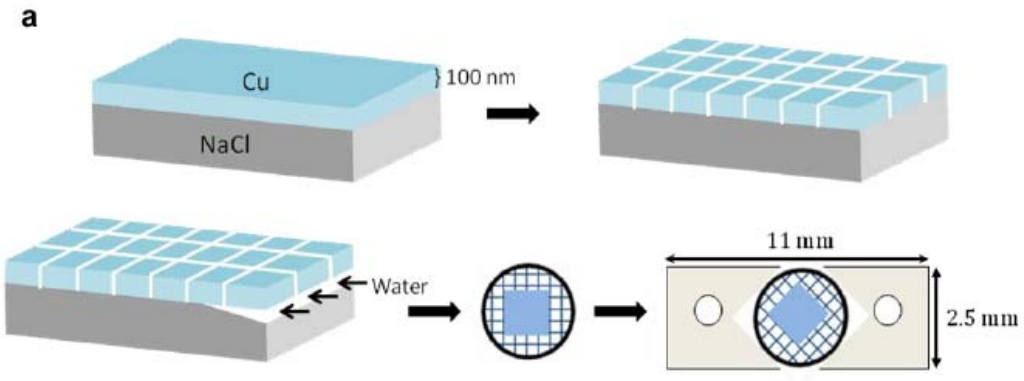

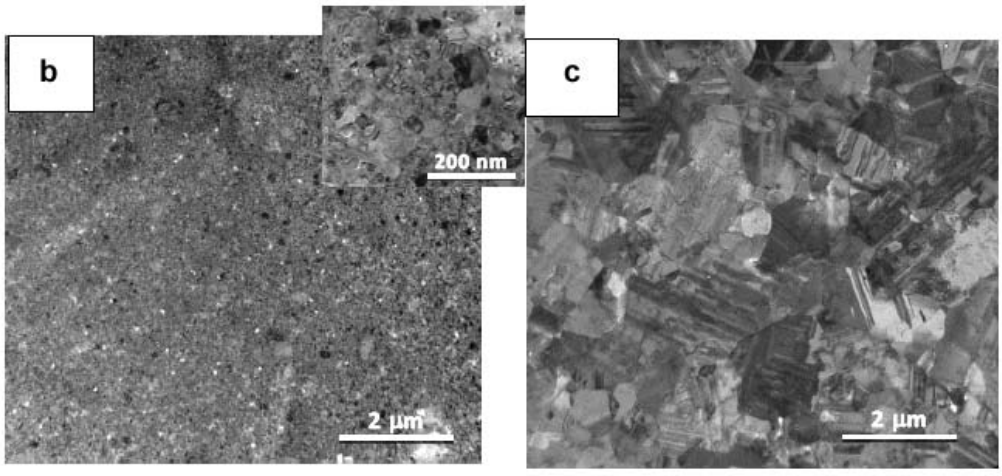

Figure 5.1. Electron-transparent samples prepared in current experiments. (a) Schematic illustration of the fabrication process of an electron-transparent, free-standing, uniform-thickness thin film utilizing a cleaved NaCl substrate. (b) A low magnification TEM micrograph showing the NC grains and the large electron-transparent area; inset shows the grains at a higher magnification. (c) The film microstructure after annealing in the TEM at 600^{o}C revealing grain growth and the presence of nanoscale twins. (Courtesy of Prof. Sharvan Kumar and Prof. Seong-woong Kim)

Before the tensile testing, the surface topology of the annealed film was examined in the SEM and surface roughness was measured using the atomic force microscope (AFM). Representative images are shown in Figs. 5.2a and 5.2b, where the GB grooves can be observed by both techniques and groove roughness can be measured by AFM, twin intersection with film surface can be seen by SEM but not well in the AFM. Therefore variation in roughness between two successive GBs is thought to relate to twins intersecting the surface but cannot be confirmed. These AFM scans across these film surfaces between two grain boundaries showed the surface roughness to have an RMS value of 3 nm.

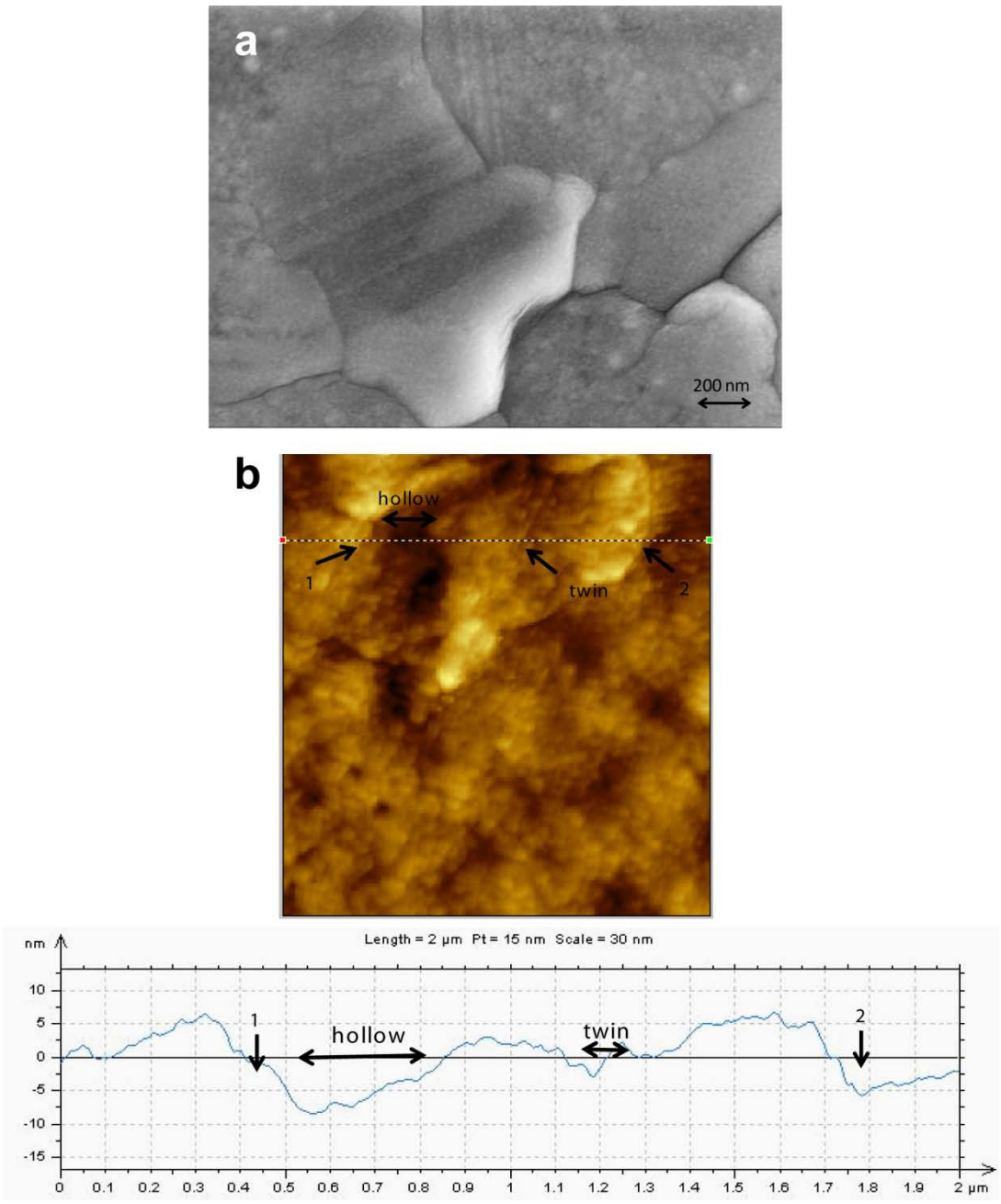

Figure 5.2. (a) Film surface topography observed by SEM after annealing the film in the TEM at 600^{o}C. Note that GB grooves are pronounced but not the TB-film surface intersections do not appear to produce pronounced steps. In (b), An AFM image of the annealed film surface and the horizontal line reflects the line scan obtained across a grain and between two adjacent GBs. A possible twin intersection with the surface is identified. The depth profile is shown and it is seen within the grains, the surface roughness has an RMS value of 3 nm.

5.2.2. In-situ observations

A sequence of snapshots obtained during the course of a crack interacting with a set of twins within a grain is shown in Figs. 5.3a-d. The primary crack is located at the top left hand corner in Fig. 5.3a. In the early stages, dislocations emitted from the crack tip interact with the first TB on the left (Fig. 5.3a) as the crack approaches the set of twins; simultaneously, the original crack tip is substantially blunted. In this early stage, dislocations are activated within the twins and as they traverse the twins, plastic deformation occurs within the twins. In the meanwhile, new cracks are nucleated at the twin/matrix interfaces on both sides of the thick leftmost twin, which are marked as interface cracks (IC) in Fig. 5.3b. These cracks are not caused by the presence of grooves on the free surfaces, but arise from the emission and slip of dislocations at TB ledges or steps [115]. In this regard, as previously noted, AFM scans showed that the surface roughness of the film has a root mean square value of 3 nm within the grains. In contrast, typical ledges have heights of 5-10 nm along the TBs in these samples, and a secondary crack was confirmed to originate at one such ledge obtained during the test, which is in agreement with previous experimental observations [115]. The newly nucleated crack trapped in the matrix between the thick twin and the adjacent thin twin to the right grows as the TBs slide (compare Figs. 5.3b and 5.3c). Simultaneously, the second twin, the thinner twin, stretches and fails in shear and the crack advances across the matrix to the right of it and then into the rightmost thick twin. Effectively, the advancing crack has jumped over the first twin which now serves as a bridging ligament. In the meanwhile, the geometry of the original crack changes due to blunting and resharpening (the location of the current crack tip, which is different from the original crack tip, is tracked in Figs.

5.3b-d with a white arrow). Further applied displacement is accommodated by plastic deformation of the unconstrained portion of the first twin (Fig. 5.3c) that then eventually shears and ruptures (Fig. 5.3d). Slip traces are evident on the surface of the failed leftmost twin in Fig. 5.3d. The crack-bridging behavior described above prevails in the present experiments on 100 nm-thick Cu films. Therefore, annealing twins in the path of an advancing crack are effective microstructural features in enhancing the toughness of the material by bridging and shielding the crack, as well as by dissipating energy through plastic deformation in the unconstrained twin bridges.

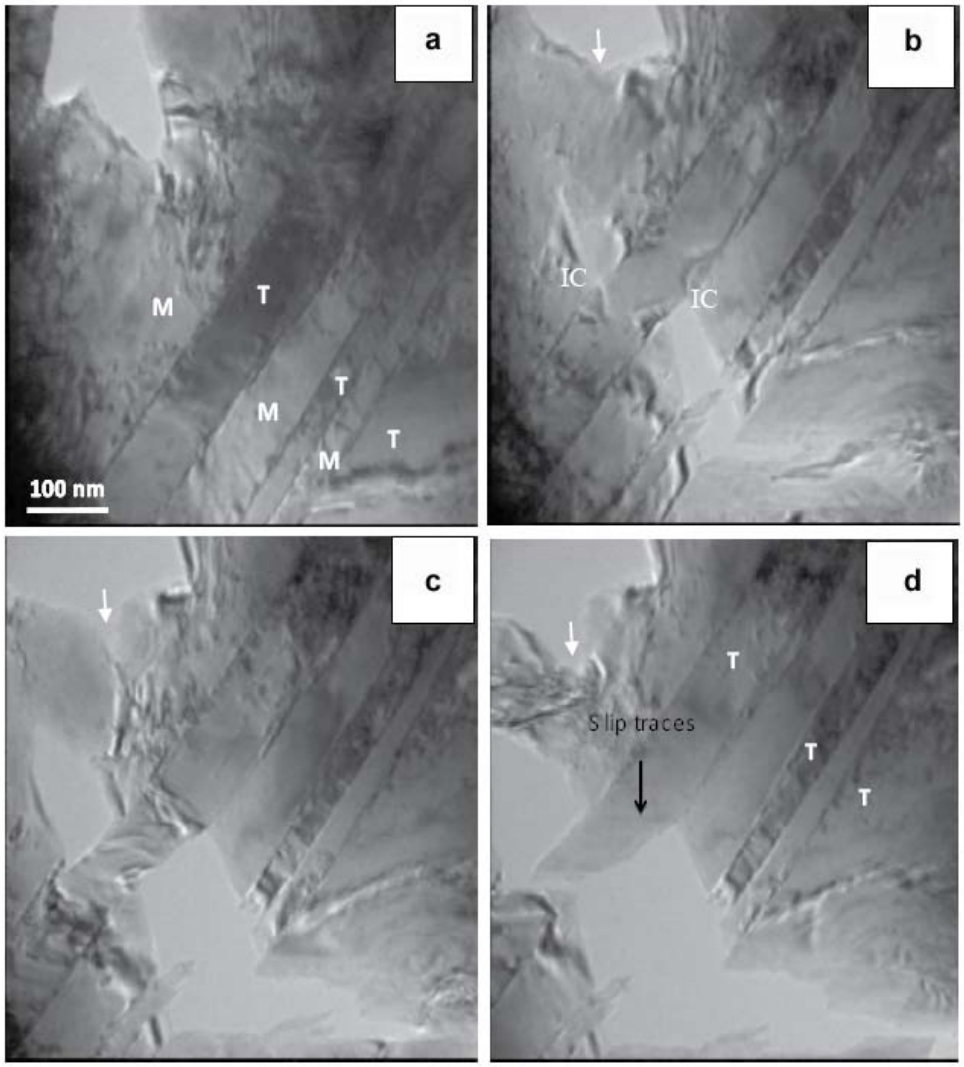

Figure 5.3. A sequence of images showing crack tip field interaction with a set of nanotwins within a grain of sample under in-situ tension. (a) The crack is at the top left hand corner and becomes substantially blunted as dislocations are emitted from the crack tip and arrive at the matrix/twin interface (see boxed region). (b) A new crack is observed on either side of the leftmost twin; the crack to the right of the first twin has grown through the middle thin twin and the matrix to the right of it and entered the third twin. (c) The crack continues to extend through the rightmost twin but the first twin remains intact and plastically deforms as it is free of constraint, becoming essentially a nanoscale single crystal ligament. (d) Finally, after considerable slip, the first twin breaks and slip traces are evident parallel to the fracture edge. (Courtesy of Prof. Sharvan Kumar and Prof. Seong-woong Kim)

5.3. Atomistic simulations

5.3.1. Simulation methodology

We performed large-scale atomistic simulations to study the interaction of dislocations emitted from the crack tip with a TB. These atomistic simulations complement the experiments (introduced in Section 5.2) by providing insights into how crack tip fields interact with twins at the nanoscale level. The details of atomistic simulations are described below.

The simulated sample has a bi-crystal configuration with both length (x) and width (y) equal to 30 nm. The thickness (z) of the samples, corresponding to the film thickness, varies from 5 nm to 100 nm, and consequently the simulated sample contains from 0.39 to 8.05 million atoms. A perfect TB is located in the middle of the bi-crystal sample. As a reliable source of dislocations, a 5 nm-length crack is created in front of the TB, with its tip located 10 nm away from the TB. The crack surface is on the $(\bar{1}12)$ plane. During the simulations, the EAM potential for Cu [124] is used to calculate the atomic force, and the Nose-Hoover thermostat [140] is used to maintain a constant temperature. To speed up the computation, a multiple time-step integrator [128] is adopted with shorter and longer time steps of 1 and 3 fs, respectively. Periodic boundary condition is imposed along the y direction, while boundaries in the x and z directions are kept free throughout the simulation. The sample is first relaxed and equilibrated at 300 K for 300 ps. Uniaxial tensile straining is then applied in the y direction via a stepwise straining method [151] at a constant strain rate of 10^8/s.

To identify the defects during plastic deformation, we painted atoms in different colors using the local crystalline order method [156]. In addition, another coloring scheme (called the position-based coloring method) is used to produce 3D effects: grey atoms are on TB, purple ones on the crack surface, and other colors represent the distance of atoms from the centre of the simulated sample.

5.3.2. Simulation results

Large-scale MD simulations were conducted to understand the process of a crack interacting with a CTB in Cu and for isolating scientific reasons for why the advancing crack jumped across the first twin it encountered rather than penetrate it and propagate across it. At the early stage of deformation, a large number of dislocations emit from the crack tip, resulting in crack blunting, as shown in Figs. 5.4 and 5.5. When these dislocations impact on the TB, complex reactions occur: these include (i) trapping of dislocations by TB, (ii) slip transfer through TB via cross-slip, and (iii) dissociation followed by one dislocation transmission through TB and another residual in the TB. As illustrated in Fig. 5.6, the reactions marked by orange and black circles describe the cross-slip of dislocations transmission through TB. The grey and blue circles show that dislocation segments on a (111) plane in the matrix arrive and interact with the TB, producing a residual dislocation remaining in TB and a transmission dislocation through TB, which further dissociates into Shockley partials in the twin. The dislocation segment circled by the purple ellipse is fully trapped by the TB. These processes primarily depend on the Burgers vector of the incoming dislocations [197]. As a result, plenty of dislocation debris resides on the TB after reaction.

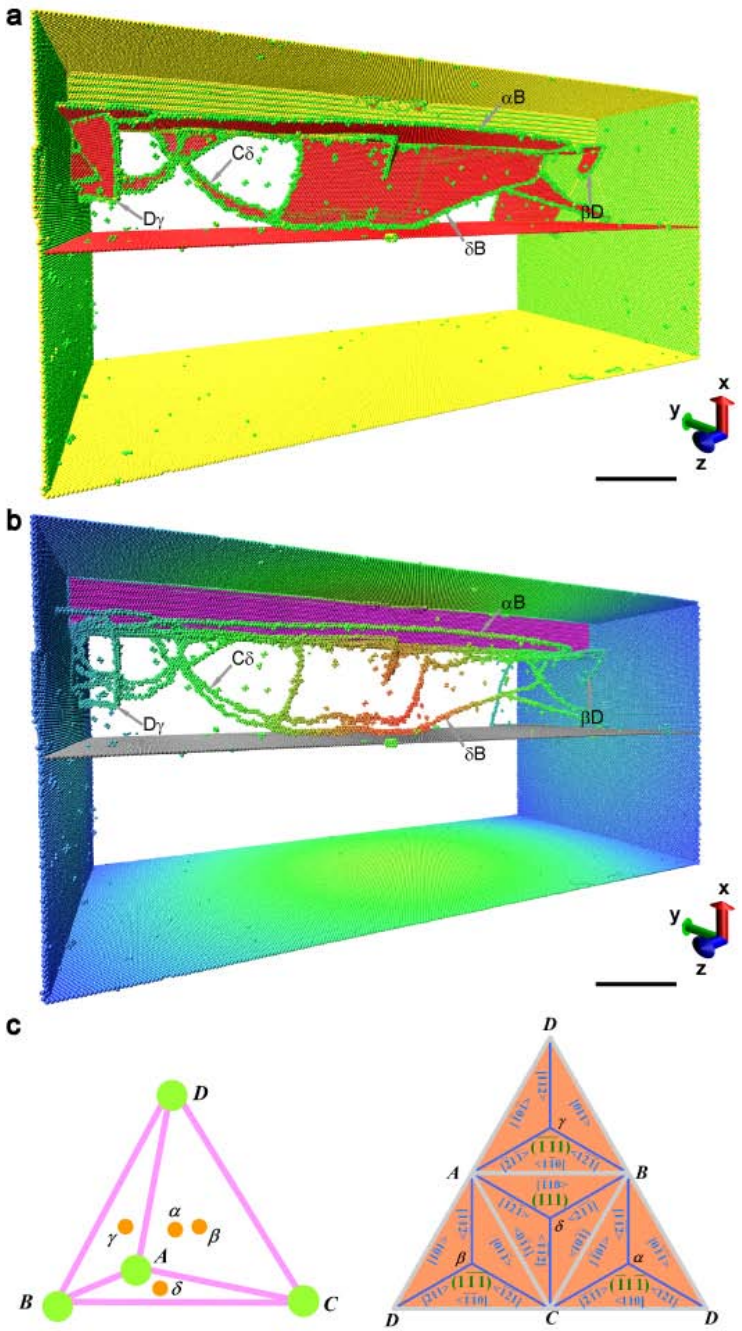

Figure 5.4. 3D dislocation structures emitted from a crack in the 60 nm-thick sample at the strain of 4.29%. All the scale bars are 5 nm. The atomic structures are revealed via (a) the local crystalline order and (b) the position coloring methods. In (a) and (b), the Burgers vector of dislocation lines are labeled based on the Thompson tetrahedron depicted in (c). It is observed that various partial dislocation lines emit from the crack tip under the applied stress.

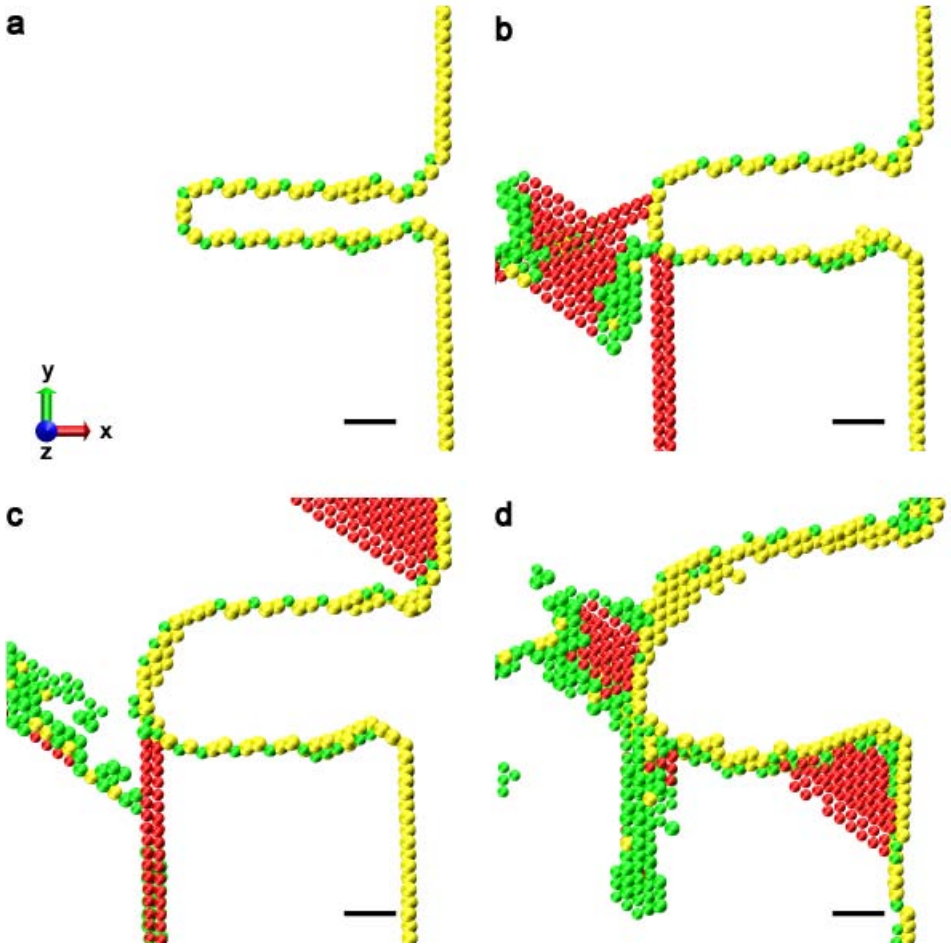

Figure 5.5. Crack morphology at the central section of the 60 nm-thick sample at different strains. (a) ε=0%. (b) ε=4.29%. (c) ε=10.5%. (d) ε=35.0%. All the scale bars are 1 nm. The crack tip becomes blunted due to dislocation emission shown in Fig. 5.4, indicating that the sample is intrinsically ductile.

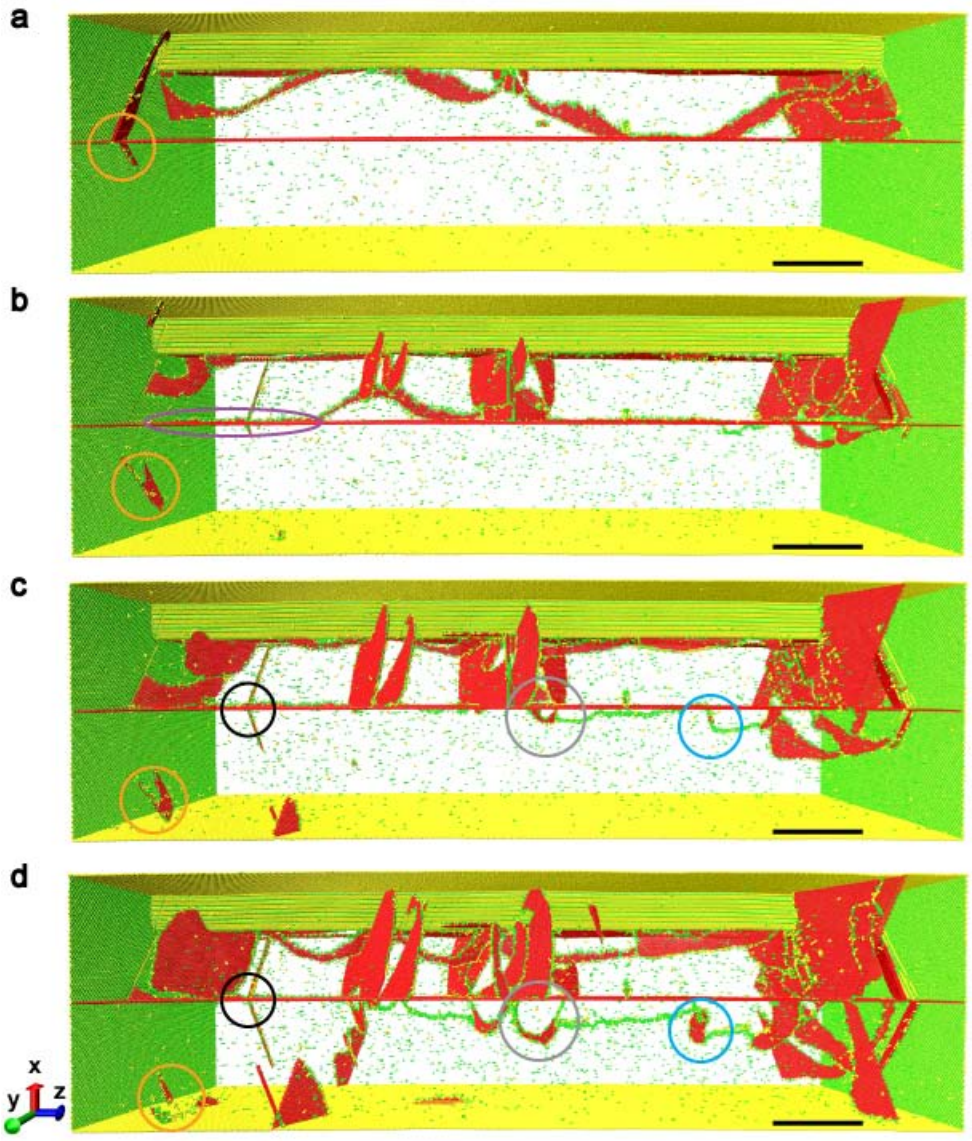

Figure 5.6. Snapshots of dislocations reacting with the TB in the 100 nm-thick sample at different strains. (a) ε=4.71%. (b) ε=5.13%. (c) ε=5.34%. (d) ε=5.55%. All the scale bars are 10 nm.

Figures 5.7a shows dislocations impinging on the TB at the strain of 10.5%, and Figs. 5.7b-d display the resulting dislocation patterns on TB after different applied strains. It is observed that the residual dislocations remain straight at the early stage of dislocation-TB interaction, while they become curved as the strain increases. These curved dislocations arise from complex dislocation reactions and constitute a dense network of dislocations

which can substantially affect the character (low energy and high symmetry) of an initially clean TB. As the plastic strain increases, dislocations accumulate to saturation on the TB. A distinct domain of high dislocation density forms on both sides of the TB, and span 14~20 lattice constants (around 5~7 nm), which is reminiscent of the experimentally observed TB affected dislocation zones [84]. Such a domain serves as a dislocation wall that blocks further dislocation activity and resists crack propagation. Figure 5.8a gives a quantitative estimation of dislocation density within the TB dislocation wall up to 10^{16}~10^{17}/m^2, which is one order of magnitude higher than the average value in grain interiors. During dislocation accumulation, the residual dislocations on TB might escape from free surfaces or experience various reactions including annihilation. Figure 5.8b indicates that while dislocation density on TB gradually rises as sample thickness increases, there exists a transitional thickness between 30 nm and 60 nm. When the film thickness is greater than 60 nm, the dislocation accumulation rate on the TB is much larger than the annihilation rate so that an initially clean TB transforms into a dislocation wall as the plastic strain increases. However, if the thickness is less than 30 nm, the accumulation rate is close to the annihilation rate, and then the TB is incapable of effectively trapping dislocations because of the low dislocation densities on the TB. In this case dislocations easily penetrate through TB and trigger fracture of the sample due to persistent slip, as evident in Fig. 5.9. During plastic deformation, no dislocation wall forms so that dislocations easily slip across the TB. The whole sample eventually fails due to strain localization in the persistent slip band.

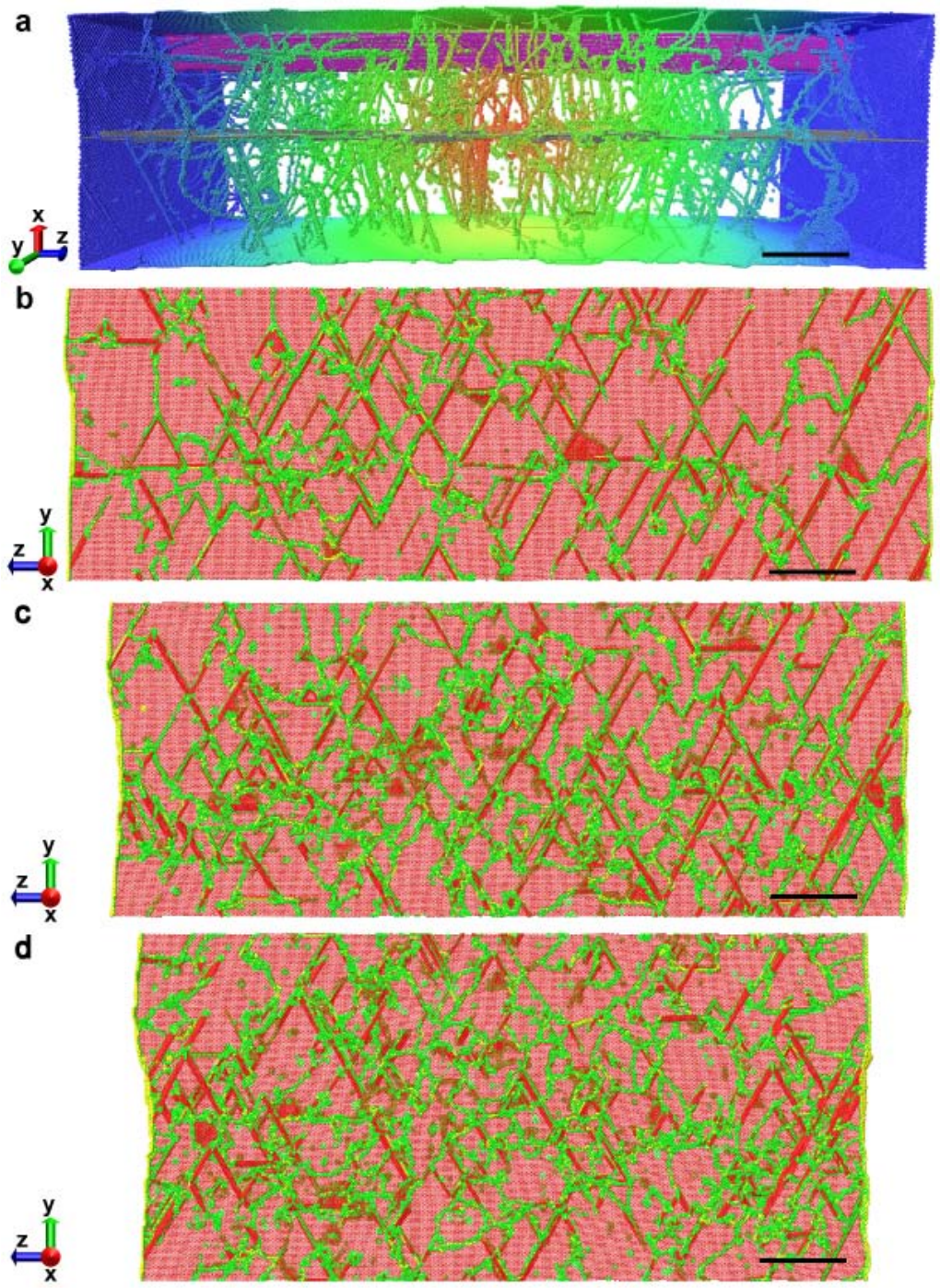

Figure 5.7. TB transforming into a dislocation wall in a 100 nm-thick sample from MD simulations. (a) 3D dislocation structures at a total strain of 10.5%; herein atoms are painted in the position coloring scheme. (b-d) Patterns of dislocation structures remaining on TB at the stain of 10.5%, 22.1% and 35.0%, respectively. Herein each atom is colored based on the local crystalline order method. All of the scale bars are 10 nm.

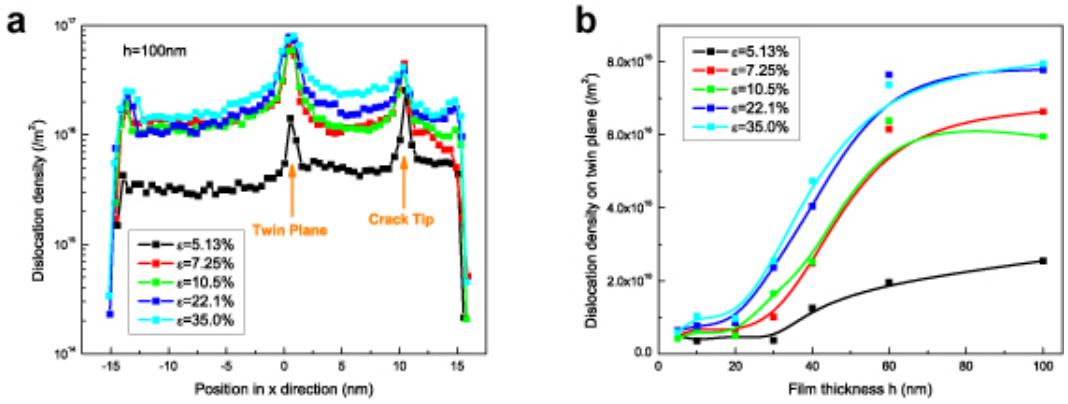

Figure 5.8. (a) Typical dislocation density distribution along the x axis under different strains. (b) Dislocation density on twin plane as a function of film thickness. The curves are based on B-spline for guidance.

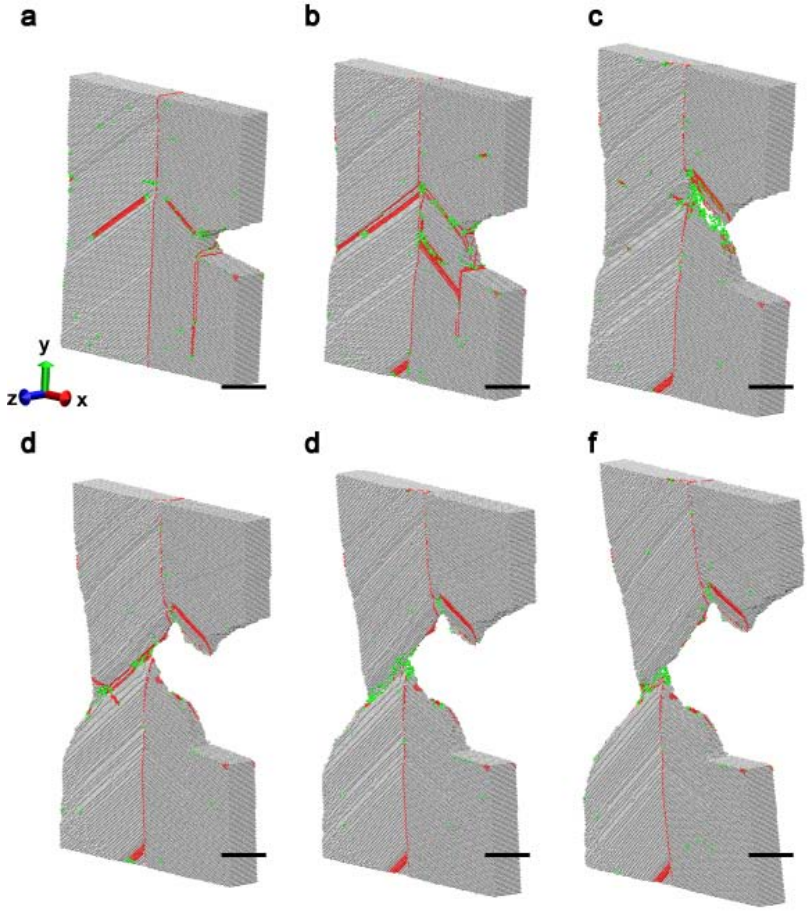

Figure 5.9. Successive snapshots of a 5 nm-thick sample at different strains. (a) ε=10.5%. (b) ε=22.1%. (c) ε=35.0%. (d) ε=49.2%. (e) ε=56.8%. (f) ε=64.9%. All the scale bars are 5 nm. Herein atoms on the free surface are set transparent for clarity.

5.4. Comparisons between experiments and atomistic simulations

Atomistic simulations in this study indicates that once a dislocation wall comes into being, TBs become effective in blocking dislocation activity and resisting crack propagation, thereby confining crack propagation to the matrix. Microcracks first initiate in the matrix near the matrix/twin interface because of favorable Schmid factor and the presence of ledges. When the single-crystal bridging twins fail due to local shear, macroscopic separation is complete. Moreover, our experimental studies showed that when the film thickness is reduced to 40 nm, the specimens failed by brittle intergranular fracture at relatively small strains, as shown in Fig. 5.10. Coupled with the analysis from atomistic simulations, these results imply that there exists a critical thickness corresponding to brittle-to-ductile transition in polycrystalline Cu thin films with nanoscale twins. When the film thickness is beyond the critical value, TBs can transform into dislocation walls which significantly improve their resistance against dislocation transmission and crack propagation. In this case, the sample exhibits a ductile failure mode via shear localization in bridging twins. However, if the sample thickness is below some critical value (40 nm in our study), the crack nucleates and grows along grain boundaries, leading to brittle fracture, even if nanoscale twins are present within the grains. Such size-dependent ductile-brittle transition should be further investigated in future work.

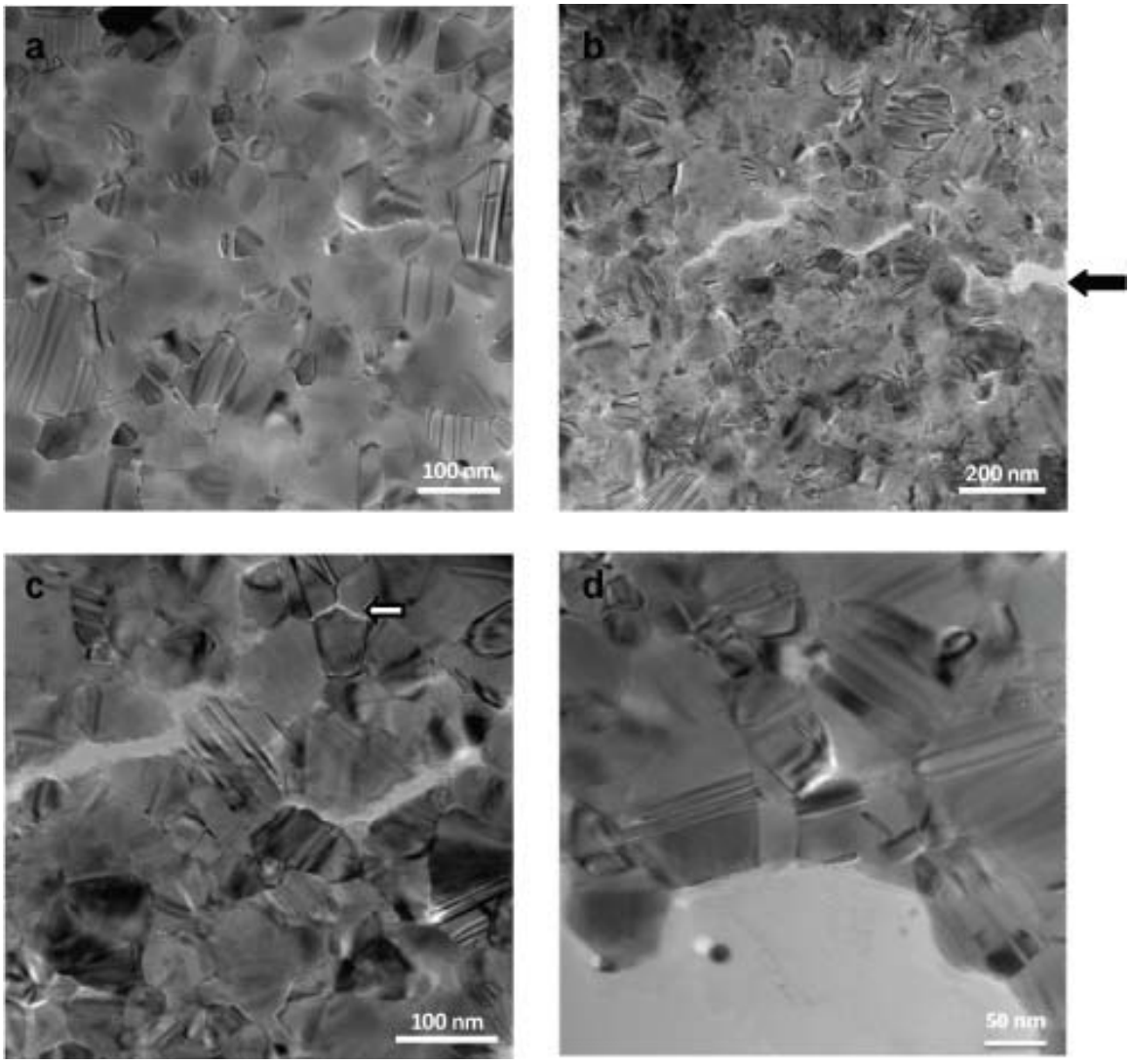

Figure 5.10. Crack growth behavior in a 40 nm-thick Cu film. (a) Columnar grains with a grain size less than 100 nm and internally twinned after heat-treatment in-situ in the TEM at 600^{o}C prior to in-situ straining testing. (b) A snapshot during in-situ straining showing the main crack on the right denoted by the black arrow and secondary intergranular cracks ahead of the main crack that will eventually link up. (c) A higher magnification image of the secondary cracks in (b) showing a single twinned grain momentarily bridging the two secondary cracks as well as a triple junction decohesion identified by a white arrow. (d) After film fracture, confirming an essentially brittle intergranular fracture path. (Courtesy of Prof. Sharvan Kumar and Prof. Seong-woong Kim)

Figure 5.11a-c show a comparison of TEM images of twins and twin/matrix interfaces located far away from the crack tip with those in the vicinity of the crack tip. Two noteworthy aspects of twins far away from the crack tip are revealed: (i) the interfaces denoted by the fringe contrast in Fig. 5.11a are devoid of dislocations and (ii) sharp ledges/steps are present on the twins that could serve as preferential sites for the interface crack nucleation observed in Fig. 5.3b. In contrast, those TBs just ahead of the crack (Fig. 5.11b; a zoom-in image of the region circled in Fig. 5.11b is shown in Fig. 5.11c) are highly dislocated and several dislocations actually span the twin and are tangled at both interfaces. Such observations are in remarkable agreement with that predicted by simulations.

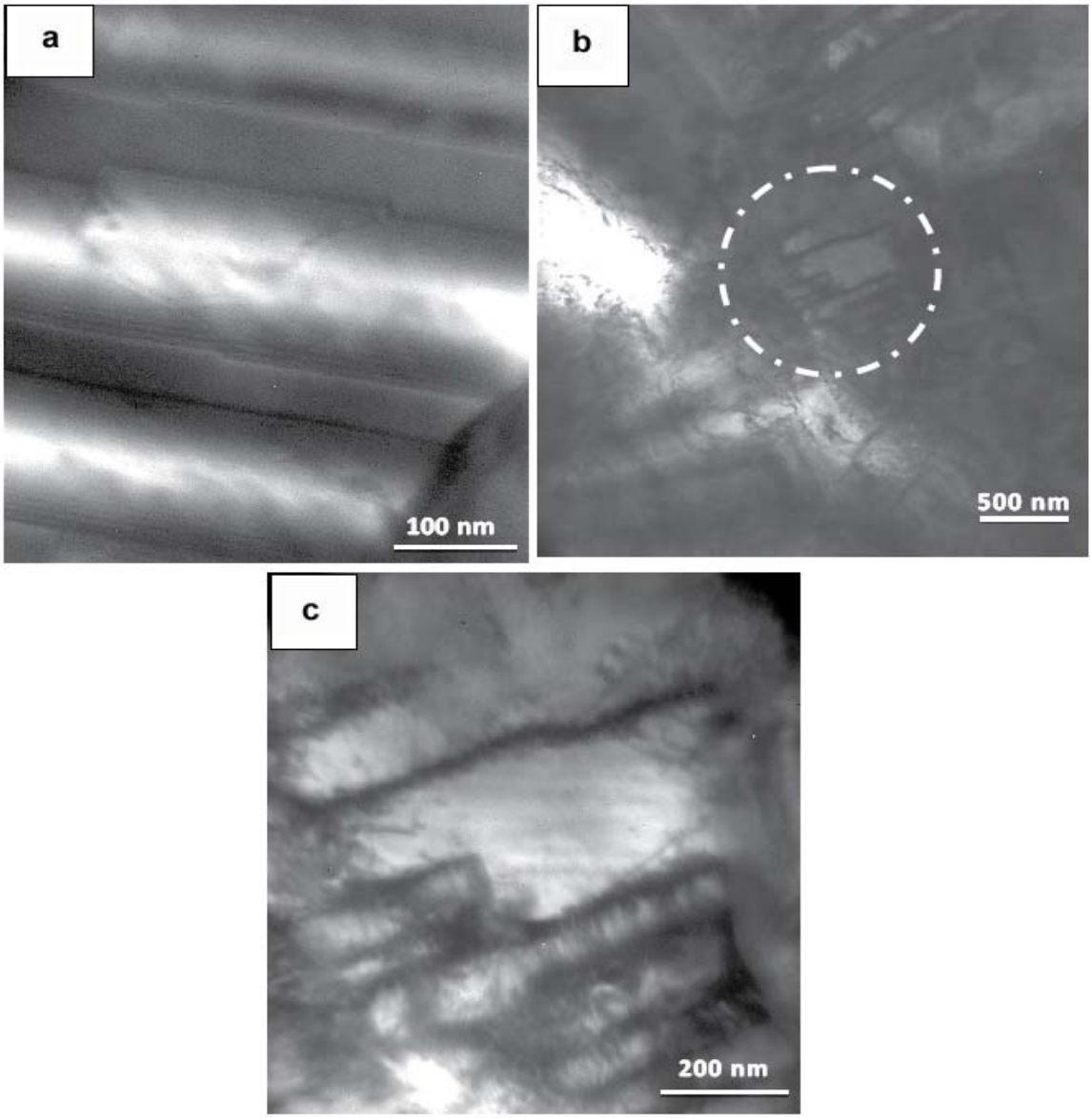

Figure 5.11. TEM images of dislocation structures on TBs in the film. (a) Matrix/twin interfaces far away from the crack tip are clean and devoid of dislocations. In addition, ledges a few nanometers wide are observed at the interfaces and can serve as dislocation emission sites as well as crack nucleation sites. (b) A low-magnification image showing the region ahead of a growing crack tip and TBs that appear highly dislocated. (c) A high-magnification multibeam bright field image of the region circled in (b) showing significant dislocation trapping at the twin/matrix interfaces. (Courtesy of Prof. Sharvan Kumar and Prof. Seong-woong Kim)

5.5. Discussions

As revealed by the in-situ observations (introduced in Section 5.2.2), nanoscale twins can resist crack propagation after transforming into dislocation walls, and also serve as bridging ligaments before materials fail due to shear strain localization. Crack bridging is known as a major toughening mechanism in ceramics and biological composites [198]-[201]. But this mechanism is rarely observed in pure metals and other homogeneous single-phase materials. Structurally, the samples synthesized in our studies are featured by a composite structure of high density of nanoscale twins embedded in the randomly oriented UFG matrix. It is also noted that all the twin structures are highly anisotropic and inherently inhomogeneous since they are very slender in shape [81]. Thus, the nanoscale twins act as hard “plates” embedded within soft matrices. In the thin film, fracture occurs due to persistent slip along a favorable slip system, followed by thinning of the film and material failure [193],[202], as seen in both matrix and twin in our experiments, leading to a zigzag crack path. This is distinct from bulk fracture which is usually characterized by microvoid nucleation, coalescence and dimpled rupture [80],[81],[203]. Such differences originate from the discrepancy of microstructures and stress states of specimens. It is therefore readily understandable that crack bridging occurs when the hard twins block dislocation activities in the film and span the wake zone of the main crack as uncracked ligaments.

An interesting aspect that needs consideration is whether the behavior of an interface arresting a crack and providing an opportunity for the crack to jump across a microstructural ligament is unique to coherent TBs or if other interfaces such as high-angle grain boundaries could provide similar resistance in a single-phase material.

When crack growth in a ductile thin film is preceded by slip and film thinning, and the slip systems of a nanoscale twin and its matrix cannot be oriented favorably with respect to the loading direction at the same time, the nanoscale twin does not experience plastic deformation as readily as the matrix and the crack tip stresses would enable thinning to proceed in the matrix across the twin. Simultaneously, dislocations impinging on the TB can be transmitted, decomposed or stopped at the interface as previously noted [197]. The resulting dislocation wall, as shown in the present paper, can hinder further slip transmission into the twin. These ideas suggest a range of twin thickness over which the twin can bridge a crack; too coarse twins will eventually rupture as would twins that are too fine. High-angle grain boundaries can behave in a similar manner and under suitable conditions can arrest cracks. An example is shown in Fig. 5.12 where a crack arrives at the grain boundary in a TEM specimen but does not readily cross it; instead, crack tip stresses are accommodated by grain-boundary sliding by dislocation motion along the boundary, resulting in a trapezoidal crack front and by the nucleation of a deformation twin some distance into the second grain. With further loading, the crack eventually enters the second grain and is arrested by the deformation twin.

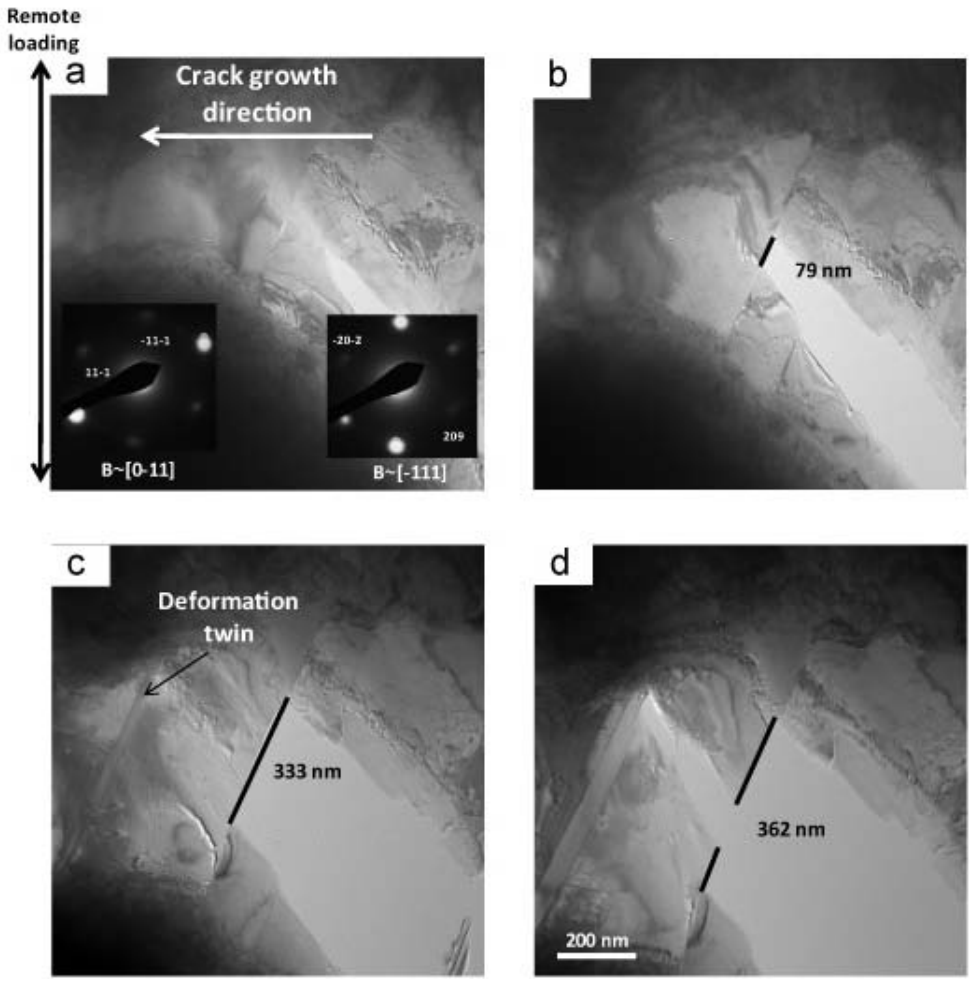

Figure 5.12. Crack Interaction with a high-angle grain boundary in a coarse-grained Cu specimen. (a) Crack advances toward the grain boundary from right to left and diffraction patterns confirm a significant misorientation of the slip systems across the boundary. (b) Crack arrests at the boundary and further applied remote displacement causes the crack tip to blunt due to grain boundary sliding. (c) The sliding continues, and a fairly significant displacement of the opposite faces of the cracks is noted; a deformation twin is generated in the adjacent grain. (d) Eventually, the crack penetrates the boundary and moves forward till it is stopped by the twin. (Courtesy of Prof. Sharvan Kumar and Prof. Seong-woong Kim)

In conventionally produced thin films (of the order of 100 nm in thickness) by either vapor deposition or electrodeposition, grains tend to be columnar and the in-plane grain

size is roughly the same as the film thickness. In such cases, triple junctions are spaced at distances of 50-60 nm. As locations of strain incompatibility, voids develop readily at triple junctions [204] and preclude boundaries from acting as effective barriers to crack growth. If the grains are coarser, then high-angle boundaries can under suitable conditions provide crack growth resistance, as shown in Fig. 5.12. Although the columnar grain boundary plane extends through the film thickness, it is important to note that twins still have the advantage of being bounded by parallel adjacent TBs and thus serving as crack bridging ligaments. When the grain size is very fine, accomplished by using very thin films, we believe triple junctions can dominate and make intergranular failure the preferred mode (as shown in Fig. 5.10) even in the presence of nanoscale twins within such grains.

5.6. Summary

The experimental study has shown a significant toughening mechanism – micro-crack bridging – in UFG Cu films with nanoscale twins as uncracked ligaments. To investigate the atomic mechanism of this rarely seen nanoscale crack bridging behavior, MD simulations were performed to show that during crack propagation, TBs are impinged upon by numerous dislocations from the plastically deforming matrix. These dislocations react at the interface, and evolve into substantially impenetrable dislocation walls that strongly confine crack nucleation and resist crack propagation, leading to the experimentally observed crack bridging behavior.

The combination of experimental and computational studies has indicated that the crack-bridging mechanism is essentially attributed to the intricate interactions between dislocations and TBs. The potency of this mechanism is likely related to the SF and TB

energies of the material, critical parameters known to influence the nature of the crack-TB interactions as well as the dislocation-TB reactions. The present study sheds light on the operative mechanisms in fracture of NT metals in free-standing thin film form. If the mechanisms do carry over to bulk metals, they could also provides a strategy for toughening polycrystalline metals that are prone to twinning and could explain the results in recent papers [80]-[83] that have experimentally confirmed that nanoscale twins enhance fracture toughness and monotonic and cyclic crack growth resistance in UFG Cu. Furthermore, the present results also raise an approach of significantly toughening polycrystalline thin films by incorporating nanoscale twin structures into individual grains that serve as crack-bridging ligaments.

Chapter 6 Deformation and Failure in Nanotwinned Copper Nanopillars

6.1. Introduction

When a high population of nanoscale twins is introduced into one-dimensional materials, such as nanowires and nanopillars, they will significantly alter the mechanical properties of materials. In this section, we review the recent experimental and computational studies on the influence of nanoscale twins on plastic deformation of metallic nanowires and nanopillars.

Deng and Sansoz [65]-[70] have conducted a series of atomistic simulations of NT Au nanowires under uniaxial tension, with TBs normal to the tensile direction. They observed that dislocations always nucleate from the intersections between TBs and free surfaces, and glide on the slip planes inclined to TBs. When dislocations approached TBs, the slip-transfer reaction occurred in the following steps [65],

(1) Shrinkage of leading Bγ and trailing γD partials: Bγ+γD→BD;

(2) Decomposition of BD into a transmission dislocation CD and a residual dislocation BC on TB: BD→BC+CD;

(3) Reaction of CD with the next TB, and its decomposition into a stair-rod dislocation Cγ on TB and a partial dislocation γD through TB: CD→Cγ+γD;

(4) Further dissociation of sessile stair-rod Cγ into full dislocation CB and partial dislocation Bγ: Cγ→CB+Bγ.

Based on these simulation results, Deng and Sansoz [65] concluded that the site-specific dislocation nucleation and the above slip-transfer reaction are controlling mechanisms in plastic deformation of NT nanowires. Considering site-specific surface dislocation emission and image forces due to the presence of TBs, they developed a model showing that the yield strength is inversely proportional to TB spacing [68], as described by Eq. (2.2). This model is consistent with results from CMD simulations, as shown in Fig. 2.7b.

Jang et al. [60] have conducted experiments on uniaxial compression of NT Cu nanopillars with diameter of 500 nm and TBs normal to the compressive axis. They found that the measured strength is much larger than that of twin-free single-crystalline pillars with the same diameter. Based on these observations, they concluded that TBs impeding dislocation slip are responsible for the strengthening of NT nanopillars. Recently, Brown and Ghoniem [74] have performed atomistic simulations of NT Cu nanopillars of diameter 9 nm under uniaxial tension and compression, with TBs inclined to the loading axis. Their simulation results showed tension-compression asymmetry, and a transition between reversible-irreversible plastic deformation: the plastic strain is found to be reversible when the resolve shear stress falls between 0.5 and 1.0 GPa and the axial strain is less than 3.3%; however, plastic irreversibility occurs at larger strains or stresses [74]. Such plastic reversible-irreversible transition has been attributed to competition between partial dislocations gliding on TBs (for reversible plasticity) and partial nucleation inclined to the free surface (for irreversible plasticity) [74].

In this chapter, we investigate deformation mechanisms in NT Cu nanopillars with orthogonal and slanted TBs, using large-scale MD simulations, and account for the TB orientation effect experimentally observed.

6.2. Experimental studies

By electroplating Cu into patterned polymethylmethacrylate templates, the research group of Prof. Julia Greer [205] have produced arrays of thousands of free-standing vertically-aligned Cu nanopillars. Each individual specimen consists of uniformly aligned nanoscale twins either perpendicular or inclined (by ~18°) to the pillar-axis with no grain-boundaries or any other features. They performed in-situ uniaxial tension tests on individual nanopillars with diameters of 50 and 100 nm in SEM and analyzed the evolved microstructure in deformed pillars via TEM analysis.

6.2.1. Characterization of fabricated nanopillars

Figure 6.1 shows SEM and TEM images, as well as an electron diffraction pattern of a representative electroplated NT Cu nanopillar. Figure 6.1a shows an as-fabricated sample with 50-nm diameter, which was intentionally over-plated to form a cap on top of the pillar to be used for tension experiments. Of note, the pillar section does not have any noticeable taper often associated with widely utilized top-down focused ion beam (FIB)-based technique for nanopillar creation [206]. Inset in Fig. 6.1a is a zoomed-out SEM image of the plated template showing a nanopillar array at 52° tilt. Figs. 6.1b and 6.1c show low and high magnification dark-field TEM images of 100-nm diameter nanopillars containing orthogonal TBs. Corresponding electron diffraction pattern is displayed in the inset of Fig. 6.1b. Incident electron beam is along [011] zone axis direction. Average twin thickness of the pillar shown in Figs. 6.1b and c is 4.3 nm. In Fig. 6.1c, the ~5 nm thick outer amorphous layer is likely native copper oxide. Fig. 6.1d shows a high resolution transmission electron microscopy (HRTEM) image. Electron beam direction in these images is also along [011] zone axis, which is perpendicular to the TB plane normal.

Solid lines in Fig. 6.1d are inserted to help identify (200), $(\bar{1}\bar{1}1)$, and $(1\bar{1}1)$ planes, which belong to the same [011] zone. It can be clearly seen that these planes are mirror-symmetric across TB. It is also evident in Fig. 6.1d that TBs are highly coherent as lattice planes do not lose crystallographic registry across boundary. No initial dislocations were found after carefully analyzing 50 TEM dark-field images over entire pillar length.

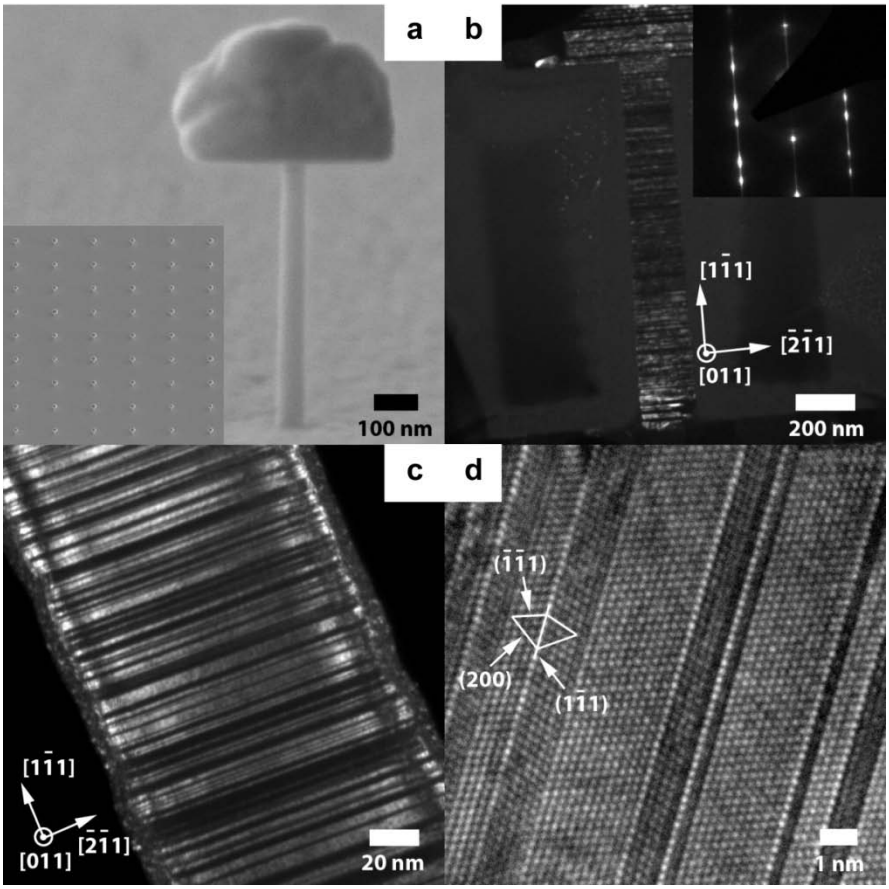

Figure 6.1. Characterization of NT Cu pillars fabricated. (a) SEM image of a typical as-fabricated NT Cu nanopillar with an intentionally overplated cap for tensile testing. The diameter of this pillar is 50nm. (b, c) Dark field TEM images and electron diffraction pattern (inset) of typical 150 and 100 nm diameter pillars with orthogonal TB, respectively. Images were taken from the [011] zone axis direction at different magnifications. (d) HREM image taken from [011] zone axis direction, showing several twin lamellae and TBs. (Courtesy of Prof. Julia Greer and Dr. Dongchan Jang)

6.2.2. Deformation and failure

Samples with three different internal/external geometries were tested experimentally. Specific characteristic length scales for each of these samples are listed in Table 6.1. Figure 6.2 shows engineering tensile stress-strain curves for (A) D100A0, (B) D50A0, and (C) D50A18, respectively, and insets display post-deformation SEM images (a,c) and bright-field TEM image (b). Intriguingly, 100 nm-diameter pillars with perpendicular TBs appear to exhibit characteristics of brittle fracture, i.e. linear elastic loading followed by sudden failure without any noticeable plasticity. Tensile stresses at fracture range from 1.8 to 2.5 GPa, with average of 2.1 GPa, a value on the order of ~40% of ideal strength of Cu [207] and 1.5 times higher than ultimate tensile strength of single-crystalline Cu nanopillars with similar diameters tested by identical methodology [208]. Post-mortem SEM image presented in the inset of Fig. 6.2a reveals no evidence of necking or shape change, suggesting that failure is of brittle nature. This is further supported by the fact that the fracture surface in Fig. 6.2a is nearly perpendicular to the loading axis as opposed to being slanted at a 45° angle. In contrast, 50 nm-diameter samples (D50A0 and D50A18) with both orthogonal and slanted TBs show enhanced plasticity rather than brittle fracture shown in 100 nm-diameter sample (D100A0). Engineering stress-strain curves in Fig. 6.2b and c show an extended plastic regime without any appreciable work-hardening. Insets in Figs. 6.2b and 6.2c show clear neck formation, further supporting observation of localized plasticity in these nanopillars. It was found that the average tensile strengths of 50 nm diameter nanopillars are 1.35 GPa for orthogonal TBs (D50A0) and 0.95GPa for slanted TBs (D50A18), respectively. This ~30% difference in yield strength is likely due to distinct dislocation behavior in these samples. In the former, TB

planes do not experience any resolved shear stress and, therefore, there is no driving force for dislocation glide along the boundaries, as is the case in tilted-boundaries samples. In addition, MD simulations have revealed that inclination angle of TBs greatly affects contribution of image stress on dislocation nucleation [70]. While image force produced by TBs generates a repulsive stress field for dislocation activities inside the pillar at TB-surface intersection for samples with orthogonal TBs [70], its influence to those with slanted TBs is nearly negligible. As a result, orthogonal samples require additional applied stress to overcome the repulsive image stress imposed by TBs while this is not the case for slanted samples. This effect of TB inclination angle is discussed in more detail in subsequent sections in conjunction with our atomistic simulation results. It should be noted that the slope of the elastic regime in Fig. 6.2 of ~60 GPa is significantly lower than Young's modulus of Cu along [111] direction, 191 GPa [209]. This discrepancy is likely due to a slight misalignment between pillar and loading axes during experiment. In addition, the wavy signature near the origin of stress-strain curves in Figs. 6.2b and c is because of instrumental artifacts, which occurred when the tension grip made contacts with samples. This does not appear to carry any effect into the mechanical behavior thereafter.

Table 6.1. List of experimentally tested samples

Specimen name	Diameter *D* (nm)	Mean TB spacing λ (nm)	TB angle
D50A0	50	1.2	orthogonal
D50A18	50	1.2	inclined by 18°
D100A0	100	4.3	orthogonal

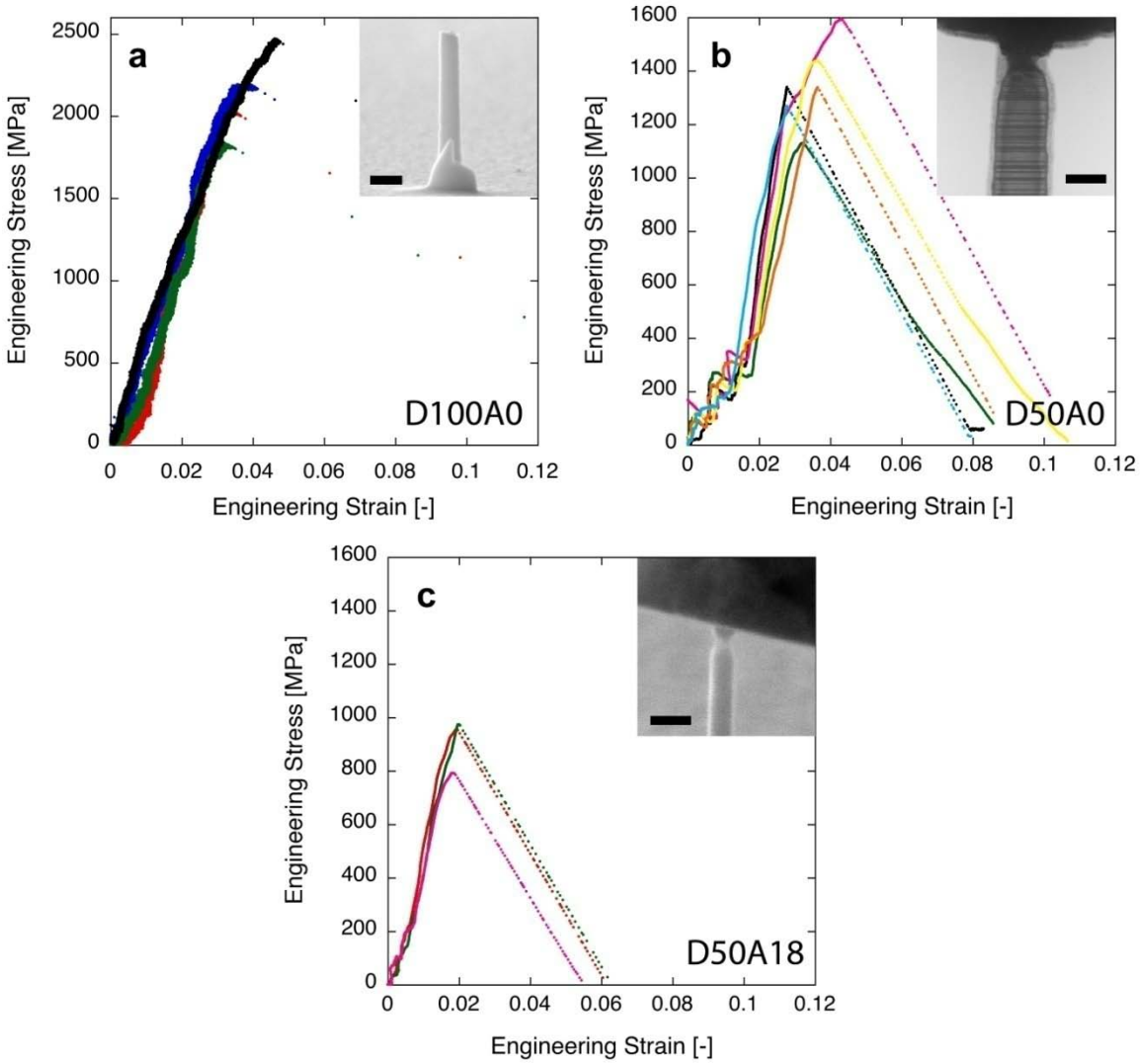

Figure 6.2. Stress-strain curves and failure behaviors of NT pillars. (a, b, c) Engineering stress-strain curves of D100A0, D50A0, and D50A18, respectively. The insets are post-deformation SEM (a, c) and bright field TEM (b) images. Scale bars of each inset indicate 200 nm, 100 nm and 50 nm, respectively. (Courtesy of Prof. Julia Greer and Dr. Dongchan Jang)

6.2.3. Deformation mechanisms

Figure 6.3 presents TEM analysis of deformation-induced microstructural changes for nanopillars with diameter of 50 nm. To conduct this rigorous analysis, it was necessary to tilt the sample such that the direction where [110] zone axis contained within the TB was

aligned with incident electron beam. Figures 6.3a and c schematically illustrate this orientation, where the circle (a) or ellipse (c) indicate TB planes and arrows within them point at the [110] zone axis direction. Interestingly, while D50A0 and D50A18 differ only by TB inclination angle with all the other dimensions same, they exhibit drastically different microstructural evolution. When TBs are perpendicular to the loading axis (D50A0), deformation is highly localized in the neck periphery, with all other region remaining virtually unaffected. The dark-field TEM image on the left in Fig. 6.3b displays this behavior, where necking is highlighted by the square box. The dark field image in the top right corner of this figure shows evidence of intense dislocation activity. Here, multiple parallel dark lines (indicated by arrows in Fig. 6.3b) were evidently formed across the twin lamellae, suggesting that they are traces of dislocations, which were likely nucleated at TB-surface intersections and subsequently glided in several different slip planes, leading to entanglement and multiplication. Interestingly, thickness of twin lamellae in the heavily deformed region appears to be unchanged since it is comparable with that in the undeformed lower part of the pillar, where no evidence of deformation can be found. In stark contrast to this deformation behavior, pillars with slanted TBs (D50A18) exhibit clear growth of twin lamellae thickness, also known as detwinning, after plastic deformation. In Fig. 6.3d, it can be clearly seen that twin lamella thickness increased up to about 15 nm after deformation (left image) as compared with the pre-deformation image (inset). Moreover, the surface of each twin lamella became faceted as can be seen in Fig. 6.3d, further suggesting that each lamella was actually deformed by shear and that detwinning was the result of deformation. Detwinning occurs by sequential nucleation of Shockley partial dislocations at TB-surface intersections and

their subsequent relatively unimpeded glide along the TB planes. Atomistic simulations in the subsequent section corroborate both of these deformation mechanisms.

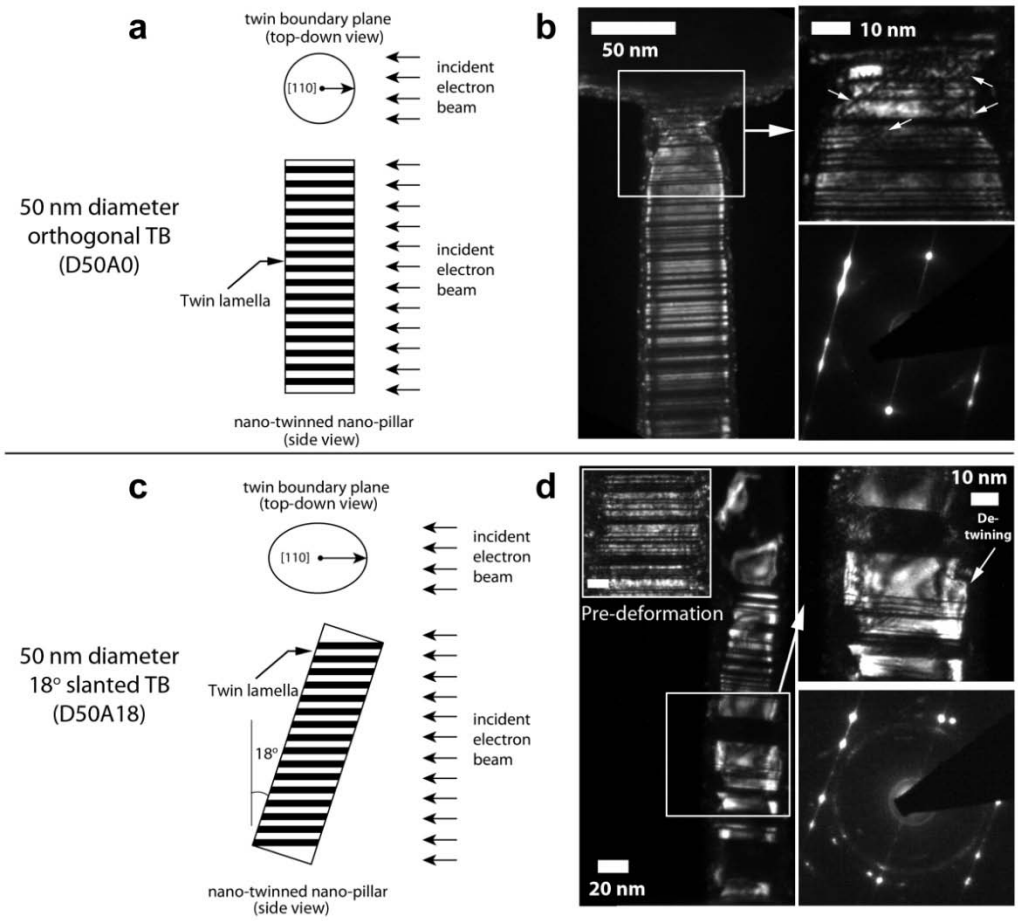

Figure 6.3. Comparison of deformation mechanisms of NT pillars with orthogonal TB and 18° slanted TB. (a, c) Schematic illustrations describing orientation of [110] zone axis lying on the TB aligned with incident electron beams in the TEM. (b) TEM dark-field images (left and top-right) and electron diffraction pattern (bottom-right) of a deformed D50A0 pillar showing neck formation and evidences of inter-TB dislocation activities. (d) TEM dark-field images (left and top-right) and electron diffraction pattern (bottom-right) of a deformed D50A18 pillar showing detwinning. The inset in the left image shows typical undeformed pillar (scale bar is 10 nm). (Courtesy of Prof. Julia Greer and Dr. Dongchan Jang)

6.3. Atomistic simulations

To investigate plasticity mechanisms in sub-100nm NT Cu pillars, we carried out MD simulations of uniaxial tension of pillars with diameter of 50 nm. Such large scale simulations complement the experiments by providing fundamental microstructural deformation mechanisms in NT pillars.

6.3.1. Simulation methodology

Large-scale atomistic simulations were performed on NT Cu pillars under uniaxial tension. The simulated samples were 50 nm in diameter and 150 nm in height, with uniform TB spacing of 1.05 nm. These size parameters are closely matched with those in the experiments. The height of the pillar was three times the diameter, which enables to exclude the end constraints from the deformation in the middle part. The sample contained about 25.05 million atoms. Similar to the experiments, two samples with different orientations were studied: one that has orthogonally-oriented twins, i.e. TB orientation is perpendicular to the pillar axis, while the other had slanted twins at 18° with respect to the axial direction. At the beginning of simulations, the samples were relaxed and equilibrated at 300 K for 300 ps using a Nose-Hoover thermostat [140] and a Beredsen barostat [139]. Then the simulated samples were stretched in the axial direction under a constant engineering strain rate of 2×10^{8} s^{-1}. This tensile loading was accomplished by the following stepwise straining method [151]. In each loading step, an incremental tensile strain of 0.02% is applied via rescaling atomic positions and followed by a system relaxation for 1 ps, while three layers of atoms at both ends of the pillar were maintained fixed. Such loading process was repeated for 1750 steps, so that the final strain was 35%. Throughout the simulations, the temperature was kept constant via the

Nose-Hoover thermostat. The EAM potential [124] was adopted to calculate interatomic forces. A multiple time step algorithm [128] was used to speed up the computation, with the short and long time steps taken as 0.001 and 0.003 ps, respectively. To identify the defects during deformation of the samples, we painted atoms in different colors using the local crystal order analysis [156]. In addition, another coloring scheme (referred to as the position-based coloring) was used to generate 3D effects, where colors represent the distance of atoms to the centre of the simulated pillar.

6.3.2. Simulation results

Atomic configurations along the middle longitudinal section of the deformed sample with orthogonal and slanted TBs are illustrated in Figs. 6.4a-c and 6.5a-d, respectively. Figure 6.4a shows that in orthogonal-TB samples, where TBs do not experience any resolved shear force, a large number of dislocations is nucleated at TB-surface intersections or near fixed ends, and then glide on slip planes inclined to TBs. When these dislocations arrive at TBs, three types of dislocation reactions were observed: (1) full trapping of dislocations by a TB, (2) cross-slip through a TB, and (3) dissociation followed by one dislocation transmitted through a TB and another residual on a TB. These types of reactions have been previously reported in experiments on NT bulk Cu [108],[113], as well as atomistic simulations on NT bulk Cu [100],[102],[108], Cu thin films [196], Au nanowires [64],[73] and nanopillars [65]. As a result of these reactions, TBs are decorated by many dislocations, some of which are mobile Shockley partials capable of slipping on TBs in the presence of a resolved shear stress. We also find that dislocation-TB interactions lead to formation of neck and resultant shear bands which gradually broaden as the applied strain increases, as shown in Figs. 6.4b and c as well as

in the experimental results in Figs. 6.2 and 6.3. During growth of shear bands, some of the original TBs are completely destroyed, as indicated by arrows in Fig. 6.4b. Shear bands can be identified in yet another manner (Fig. 6.4c). In the initial sample, we assign atoms in different twin lamella (a total amount of 143) using different colors. All twin lamellae are initially orthogonal to the loading direction. Once a shear band arises due to dislocation penetration through TBs, the twin lamella will be locally dislocated. In the regions surrounded by the black lines in Fig. 6.4c, twin lamellae are severely distorted along the shear direction, indicating that those regions are indeed well-developed shear bands. In addition, it is noted that a void is nucleated near the right end from stress-driven aggregation of vacancies. During plastic deformation, this void does not seem to grow. The shear band is a manifestation of shear strain localization, which is a common deformation mode in ductile materials. Such deformation mode has been reported in experimental studies [210] on NT Cu-Al alloy processed by DPD as well as atomistic simulations [92] of NT bulk Cu under uniaxial tension.

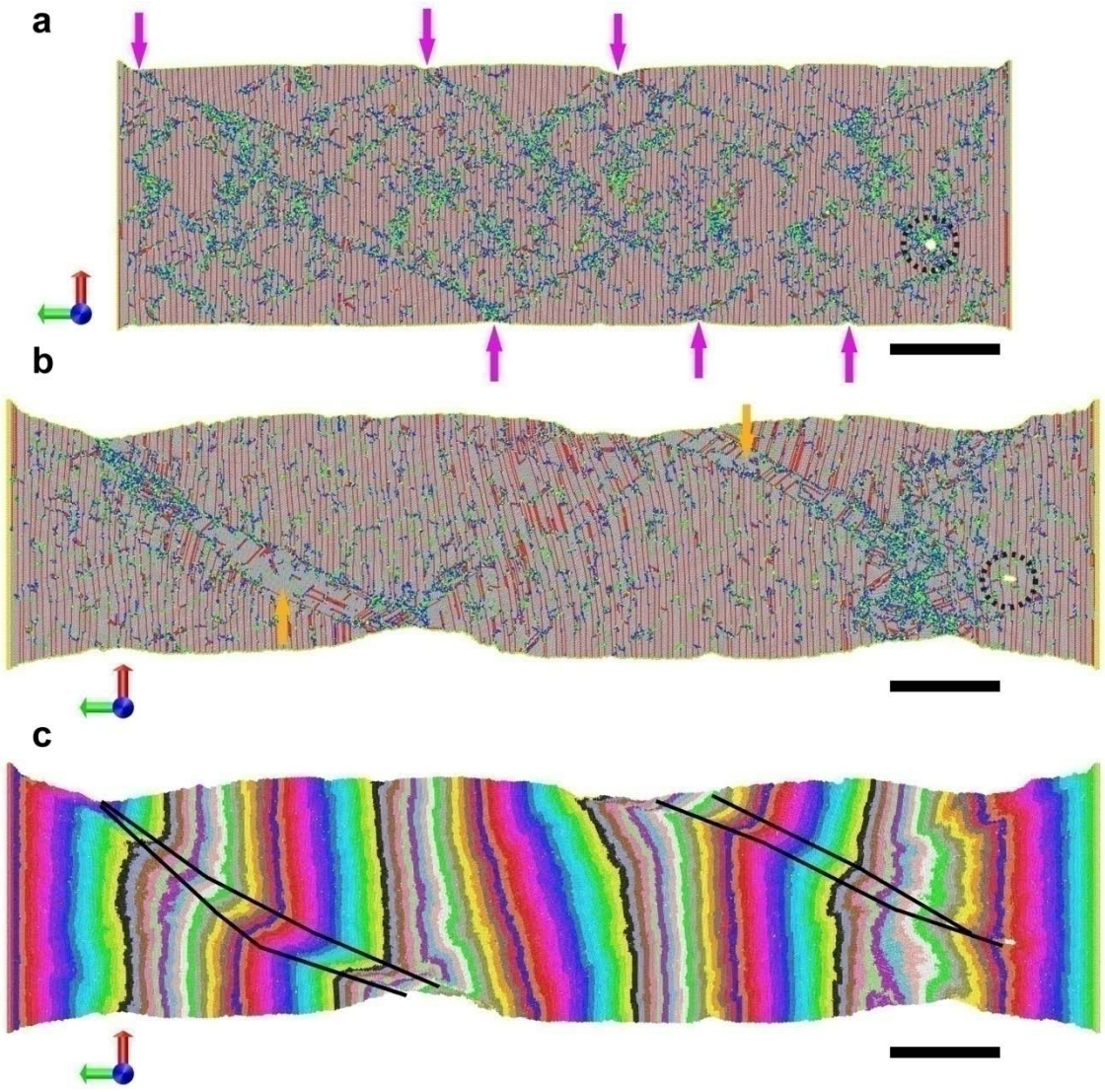

Figure 6.4. Deformation characteristics of the simulated samples with orthogonal TBs. (a) Atomic structures along the middle longitudinal section of the deformed sample at strain of ε=10.52%. (b, c) Atomic structures along the middle longitudinal section of the deformed sample at strain of ε=34.98%. Note that the microstructures pointed by the orange arrows in (b) are in well-developed shear bands where the original TBs have been completely destroyed. The regions surrounded by the black lines in (c) represent shear bands where the lattice structures are severely distorted. All the scale bars are 20 nm. Atoms in (a) and (b) are rendered in the local crystal order method.

Figures 6.5a-d show atomic structures of half of pillars with tilted TBs (inclination angle of 18°) extended to different strains. Here, it can be seen that massive dislocation slip on TBs leads to TB migration and even disappearance of some twin lamellae. This detwinning exactly coincides with our experimental results shown in Fig. 6.3d. Such phenomenon has also been observed in large-scale MD simulations [211] for uniaxial tension of NT nanowires with tilted TBs (inclination angle of 30°). Depletion of twins leads to formation of multiple surface steps because of dislocations escaping from the free surface. Subsequently, these surface steps serve as sources of new dislocation for further plastic deformation. After the middle part of the sample becomes twin-free, dislocations glide on other non-twin slip planes. As shown in Fig. 6.5b, numerous dislocations are nucleated from surface steps and travel through the interior, leading to the dislocation tangle shown in Fig. 6.5d. Compared to the entangled dislocation structure in Fig. 6.5d, Figure 6.5c shows more ordered dislocation lines gliding on TBs during the detwinning process.

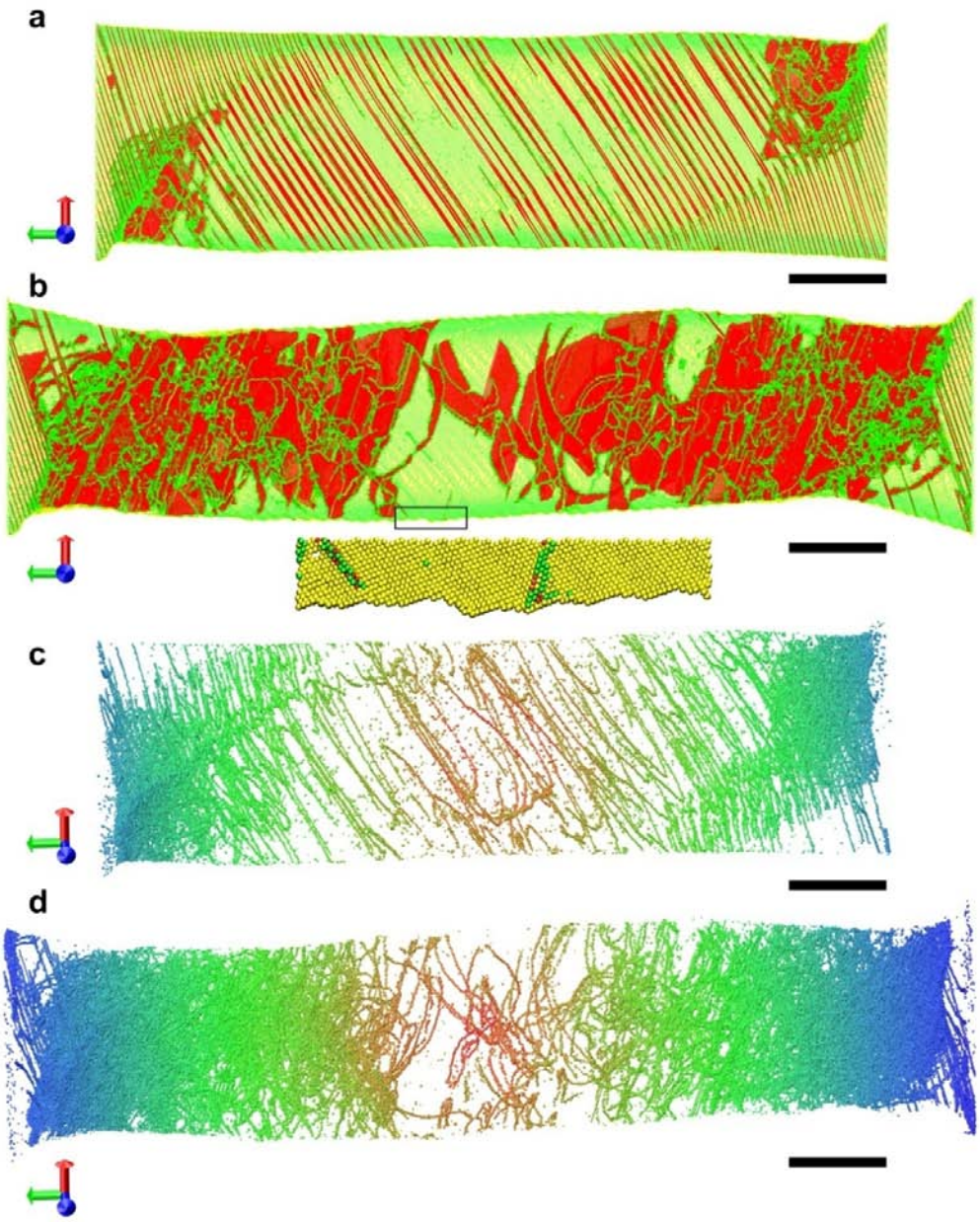

Figure 6.5. Deformation characteristics of the simulated samples with slanted TBs. (a, b) Sectional view at the strain of ε=10.52% (a) and ε=34.98% (b). The region marked by the black rectangle is magnified on the bottom. This inset shows two dislocations being nucleated from surface steps due to the early detwinning. (c, d) Dislocation structures at the strain of ε=10.52% and ε=34.98%, respectively. Compared to (d), dislocation structure in (c) is more ordered. All the scale bars are 20 nm. Atoms in (a) and (b) are rendered in the local crystal order method, while atoms in (c) and (d) are rendered in position-based coloring.

Figure 6.6a shows stress-strain curves obtained by MD simulations for uniaxial tension of NT pillars with orthogonal and tilted TBs. Since all samples were initially dislocation free, peak stresses shown in Fig. 6.6 should largely reflect the stress required for either full or partial dislocation nucleation. Samples with orthogonal TBs generally have higher stresses, especially the peak stress, than those with tilted ones, and these stress-strain curves are comparable with the experimental data (Fig. 6.2). This implies that dislocation nucleation and propagation in samples with orthogonal TBs are harder to activate or maintain than those in the samples with tilted TBs. Subsequent drop in the stress is caused by dislocation propagation immediately after nucleation. Once enough mobile dislocations have been generated to accommodate the imposed deformation, the stress drops down to a lower level, and dislocation density rises up to a higher level. As deformation proceeds, new dislocations continue to nucleate and/or multiply while existing mobile dislocations tend to annihilate due to dislocation reactions or escape from the free surface. Dislocation density saturates as the annihilation rate is balanced by the nucleation rate. Such evolution of dislocation density corresponds to the black curve in Fig. 6.6b for the sample with orthogonal TBs. For the sample with tilted TBs, on the other hand, dislocation density rises only slightly after initial yielding, as dislocation slip is activated again after detwinning. Figure 6.6c shows a reduction in the number of hcp atoms in the course of deformation, providing strong evidence for the detwinning process. In NT metals, detwinning involves successive TB migration via partial dislocation slip along pre-existing TBs. Such processes eventually lead to vanishing of twins and reduction in hcp atoms. For the sample with tilted TBs, the detwinning process lasts from 7% to 24.5% strain. Contrary to this mechanism, in the sample with orthogonal

TBs, reduction in hcp atoms is mainly caused by TBs being destroyed by dislocation-TB interactions, which results in loss of their coherency. Here detwinning plays only a minor role (if at all) in decreasing of number of hcp atoms.

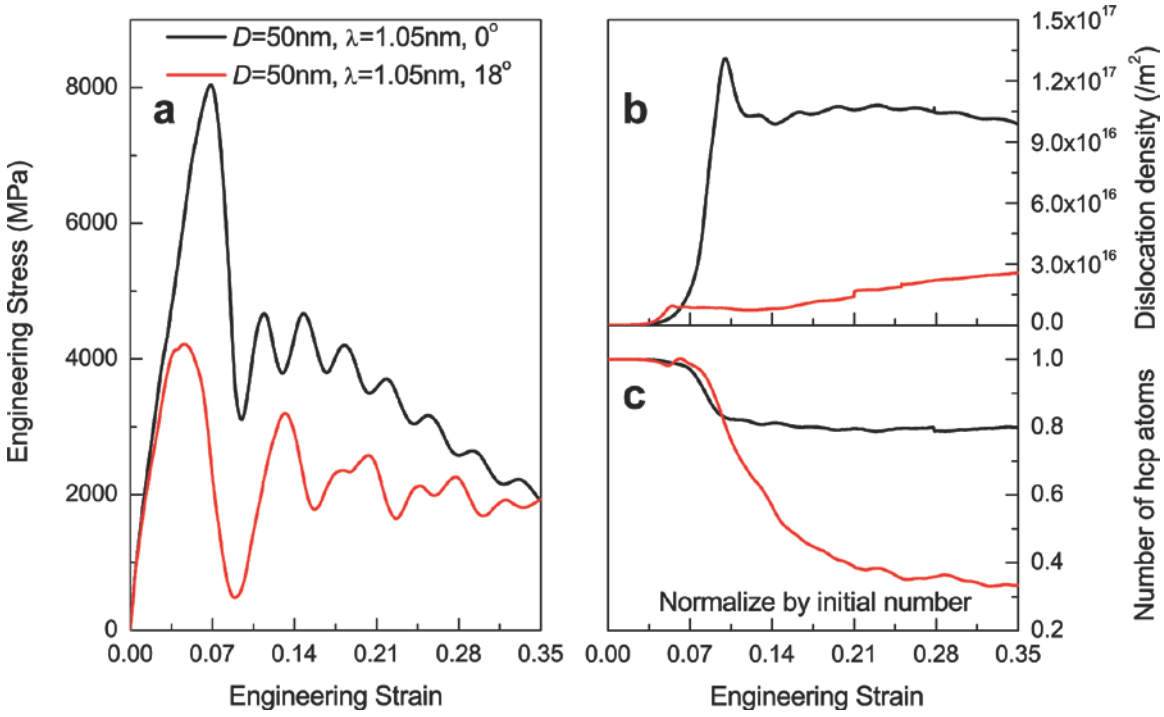

Figure 6.6. MD simulations of NT Cu nanopillars under uniaxial tension. (a) Stress-strain curves. (b) Evolution of dislocation density with the applied strain. (c) Variation of the normalized number of hcp atoms with the applied strain.

6.4. Summary

Experimental results have indicated that 50-nm diameter nanopillars containing orthogonally-oriented, 1.2 nm-spaced TBs attain very high strengths of 1.35 GPa and deform via necking while those with slanted TBs deform at lower stresses of 0.95 GPa. Both samples fail via necking upon tensile loading. Remarkably, both site-specific pre- and post-mortem TEM analysis reveal that the orthogonal-TB samples were extended via surface nucleation and extensive activity of multiple, randomly oriented dislocations,

which led to their severe entanglement and multiplication. This is caused by lack of resolved shear force along the crystallographic planes containing TBs, which therefore block dislocation glide, leading to necking. In contrast, while tilted-TB samples also deformed via dislocation nucleation at the TB-surface interface, dislocations in this case glided unimpeded along the TBs until their annihilation at the opposite surface. This resulted in reduced strengths, twin lamellae growth (i.e. detwinning), and no dislocation storage.

To complement the experiments, we preformed the large-scale atomistic simulations for uniaxial tension of NT Cu nanopillars. The diameter of simulated samples is comparable to that of samples used in experiments, and their TB orientations are the same as those in experiment. From simulations, it was observed that shear localization caused by TB-dislocation interaction dominates plastic deformation in orthogonal-TB samples, while partial dislocation glide along inclined TBs followed by detwinning controls deformation in slanted-TB samples. Such distinction in deformation mechanisms leads to difference in their strengths. Despite these differences, deformation in both types of structures is accommodated by dislocation nucleation at TB-surface intersections, with their subsequent activity dictated by the resolved shear force acting along TBs. These results from simulations are in excellent consistent with those from experiments.

The combination of experiments and simulations discerns the specific role TBs play on the deformation of small-scale structures and sheds further light on dislocation nucleation-governed plasticity in nanosized volumes.

Chapter 7 Conclusions and Perspective

7.1. Concluding remarks

Using the large-scale MD simulations, we have investigated the deformation and failure of NT Cu, in forms of bulk, thin films and nanopillars. The scientific findings for each chapter are summarized as follows.

In Chapter 4, three typical deformation mechanisms have been found during the plastic deformation of NT bulk metals. In the equiaxed-grained NT Cu, it was demonstrated that the strength increases with decreasing TB spacing, as predicted by the well-known Hall-Petch model based on dislocation pileup. However, when the TB spacing falls below a critical size, the strength softening controlled by nucleation and motion of partial dislocations parallel to the twin planes was observed in our MD simulations. In the columnar-grained NT Cu, a third possible deformation mechanism involving movement of threading dislocations confined inside the twin lamellae could dominate the plastic deformation when the tensile axis is parallel to the twin planes. These mechanisms are dislocation-based in nature. For the first mechanism, a large number of dislocations nucleate from GBs and glide on the slip planes inclined to TBs, leading to an apparent size-strengthening of NT metals. Such size effect can be described by the classical Hall-Petch model. For the second mechanism, many dislocations nucleate at the TB-GB intersections, and then slip along TBs, leading to TB migration. As partial dislocations successively glide on TBs, the twin domains will narrow and even vanish. We have developed the kinetic theory of dislocation nucleation and obtained a scaling

law (see Eq. (4.4)). Such scaling law reveals that the size-softening of NT metals is governed by dislocation nucleation. In the third mechanism, dislocations are nucleated from GBs and then bow out in the lamellar channels confined by neighboring TBs, in a similar to threading dislocations frequently observed in nanoscale thin films and multilayer materials. When such mechanism prevails, the material strength will increase as the TB spacing is decreased, which can be described by the CLS model (see Eq. (4.9)).

In Chapter 5, in-situ experiments have revealed a novel toughening mechanism in NT Cu thin films, i.e. micro-crack bridging with nanoscale twins as ligaments. Using large-scale atomistic simulations, we found that TB near crack can transform into a dislocation wall, due to the interaction between dislocations emitted from crack tip and TBs. Once the dislocation wall comes into being, it can effectively resist the crack propagation. On the other hand, in NT Cu thin films, twins have a slender shape. Combining the above two factors, we can further understand the observed phenomenon -- the nanoscale twins served as crack-bridging ligament. The present studies indicated that the nanoscale twins are effective in arresting cracking propagation during fracture.

In Chapter 6, both experiments and simulations revealed that NT nanopillars with orthogonal TB hold higher yield strength due to dislocation cutting through TBs, while NT nanopillars with slanted TB have lower yield strength because detwinning is a governing mechanism during plastic deformation. But their deformation mechanisms are dislocation-based, and dislocations in both nanopillars nucleate from the intersections between TB and free surface. Notably, dislocations can be stored in specimen with orthogonal TB during deformation, due to dislocation tangle. However, for specimen with slanted TB, a large number of dislocations escaped from free surface along TBs

during detwinning, leaving many surface steps, which become the dislocation source sites for the subsequent deformation. It is implied that free surface play a significant role in dislocation nucleation and storage.

7.2. Outlook of future research

In spite of the tremendous progresses made in recent years, our understanding of the mechanical and physical properties of NT hierarchical metals is still in an infant stage. There remain many open questions in the field, a few of which are listed below.

(1) NT metals have higher strain hardening rate, relative to UFG and NC metals, which leads to a good tensile ductility of NT metals. It is more amazing that the strain hardening exponent increase with decreasing TB spacing in NT metals. This trend is opposite to that in twin-free UFG and NC metals, as illustrated in Fig. 2.9. Such size effect of strain hardening is closely related to dislocation activities during plastic deformation. But what is the intrinsic mechanism/regime which determines the strain hardening exponent increasing with decreasing TB spacing in NT metals?

(2) There have been various synthesis methods to introduce twin structures into pure materials. Currently, the embedded twins principally originate from growth, annealing and deformation twinning. The fabrication and stability are two important issues all along in the researches of NT materials. Thus, two crucial questions are what kind of materials (metals or alloys) can be fabricated into a NT hierarchical material, and whether there is a lower limit of TB spacing for the stability of NT materials.

(3) For NT nanowires and nanopillars, the yield strengths depends on TB spacing and sample diameter, even TB orientation. Atomistic simulations have revealed that when the sample diameter is fixed and TB is normal to loading axis, the yield strengths of NT

nanowires and nanopillars inversely proportional to TB spacing. This quantitative relationship need to be verified by further experimental studies. A more important question is how the yield strengths of NT nanowires and nanopillars depends on a combination of sample diameter, TB spacing and orientation.

(4) For the studies NT Cu nanopillars in Chapter 6, there is still an unsolved question: why do NT Cu nanopillars with diameter of 100 nm exhibit the brittle fracture, while other specimens with diameter of 50 nm have the ductile fracture? Which factor or mechanism gives rise to such the brittle-to-ductile transition in NT Cu nanopillars?

(5) As a hierarchical material, NT metals have exhibited enhanced mechanical properties. In particular, NT metals have optimal strength corresponding to a certain grain size and TB spacing. The pursuit toward super-strong/strongest materials is always an untiring goal of researches in field of material science. Therefore, an urgent issue in NT metals is whether and how one could design the intrinsic structures of NT metals to control microscopic deformation mechanisms and/or the optimal strength.

(6) It is known that alloying is a powerful approach to control the strength and ductility of metals by controlling dislocation motion via various solute atoms. If one simultaneously introduces solute atoms and nanoscale twin to metallic materials, whether the mechanical properties of materials can be significantly enhanced?

Clearly, there are plenty of research opportunities to improve our understanding of NT hierarchical materials in the near future. There will be also urgent needs to perform further experimental and computational investigations on fabrication, thermal stability, mechanical testing, structural optimization and applications of various forms of NT materials including bulk materials, films, nanowires and nanopillars. These efforts will be

multidisciplinary and require the development of novel experimental and multiscale modeling techniques in the foreseeable future.

Bibliography

[1] Meyers MA, Mishra A, Benson DJ. Mechanical properties of nanocrystalline materials. *Prog. Mater. Sci.* 2006, 51, 427-556.

[2] Zehetbauer MJ, Zhu YT. Bulk nanostructured materials. Wiley-VCH Verlag Gmbh & Co. KGaA, Weinheim, 2009.

[3] Yamakov V, Wolf D, Phillpot SR, Mukherjee AK, Gleiter H. Deformation-mechanism map for nanocrystalline metals by molecular dynamics simulation. *Nature Mater.* 2004, 3, 43-47.

[4] Yamakov V, Wolf D, Salazar M, Phillpot SR, Gleiter H. Length-scale effects in the nucleation of extended dislocations in nanocrystalline Al by molecular-dynamics simulation. *Acta Mater.* 2001, 49, 2713-2722.

[5] Yamakov V, Wolf D, Salazar M, Phillpot SR, Gleiter H. Dislocation processes in the deformation of nanocrystalline aluminium by molecular-dynamics simulation. *Nature Mater.* 2002, 1, 1-5.

[6] Van Swygenhoven H, Derlet PM, Froseth AG. Stacking fault energies and slip in nanocrystalline metals. *Nature Mater*. 2004, 3, 399-403.

[7] Van Swygenhoven H, Derlet PM, Froseth AG. Nucleation and propagation of dislocations in nanocrystalline fcc metals. *Acta Mater.* 2006, 54, 1975-1983.

[8] Christian JW, Mahajan S. Deformation twinning. *Prog. Mater. Sci.* 1995, 39, 1-157.

[9] Yamakov V, Wolf D, Phillpot SR, Gleiter H. Deformation twinning in nanocrystalline Al by molecular-dynamics simulation. *Acta Mater.* 2002, 50, 5005-5020.

[10] Liao XZ, Zhou F, Lavernia EJ, He DW, Zhu YT. Deformation twins in nanocrystalline Al. *Appl. Phys. Lett.* 2003, 83, 5062-5064.

[11] Chen M, Ma E, Hemker KJ, Sheng H, Wang Y, Cheng X. Deformation twinning in nanocrystalline Aluminum. *Science* 2003, 300, 1275-1277.

[12] Zhu YT, Liao XZ, Srinivasan SG, Lavernia EJ. Nucleation of deformation twins in nanocrystalline face-centered-cubic metals processed by severe plastic deformation. *J. Appl. Phys.* 2005, 98, 034319.

[13] Zhu YT, Li XZ, Wu XL. Deformation twinning in nanocrystalline materials. *Prog. Mater. Sci.* 2011, 57, 1-62.

[14] Chokshi AH, Rosen A, Karch J, Gleiter H. On the validity of the Hall-Petch relationship in nanocrystalline materials. *Scripta Metall. Mater.* 1989, 23, 1679-1684.

[15] Lu L, Sui ML, Lu K. Superplastic extensibility of nanocrystalline Copper at room temperature. *Science* 2000, 287, 1463-1466.

[16] Schiøtz J, Di Tolla FD, Jacobsen KW. Softening of nanocrystalline metals at very small grain sizes. *Nature* 1998, 391, 561-563.

[17] Schiøtz J, Jacobsen KW. A maximum in the strength of nanocrystalline Copper. *Science* 2003, 301, 1357-1359.

[18] Kumar KS, Suresh S, Chisholm MF, Horton JA, Wang P. Deformation of electrodeposited nanocrystalline nickel. *Acta Mater.* 2003, 51, 387-405.

[19] Yamakov V, Wolf D, Phillpot SR, Gleiter H. Grain-boundary diffusion creep in nanocrystalline palladium by molecular-dynamics simulation. *Acta Mater.* 2002, 50, 61-73.

[20] Van Swygenhoven H, Spaczer M, Caro A, Farkas D. Competing plastic deformation mechanisms in nanophase metals. *Phys. Rev. B* 1999, 60, 22-25.

[21] Shan ZW, Stach EA, Wiezorek JMK, Knapp JA, Follstaedt DM, Mao SX. Grain boundary-mediated plasticity in nanocrystalline nickel. *Science* 2004, 305, 654-657.

[22] Lu K, Lu L, Suresh S. Strengthening materials by engineering coherent internal boundaries at the nanoscale. *Science* 2009, 324, 349-352.

[23] Wang YM, Chen MW, Zhou FH, Ma E. High tensile ductility in a nanostructured maetal. *Nature* 2002, 419, 912-915.

[24] Han BQ, Lee, Z, Witkin D, Nutt S, Lavernia EJ. Deformation behavior of bimodal nanostructured 5083 Al alloys. *Metall. Mater. Trans. A* 2005, 36, 957-965.

[25] Horita Z, Ohashi K, Fujita T, Kaneko K, Langdon TG. Achieving high strength and high ductility in precipitation-hardened alloys. *Adv. Mater.* 2005, 17, 1599-1602.

[26] Zhao YH, Liao XZ, Cheng S, Ma E, Zhu YT. Simultaneously increasing the ductility and strength of nanostructured alloys. *Adv. Mater.* 2006, 18, 2280-2283.

[27] Zhao YH, Zhu YT, Lavernia EJ. Strategies for improving tensile ductility of bulk nanostructured materials. *Adv. Eng. Mater.* 2010, 12, 769-778.

[28] Lu L, Shen Y, Chen X, Qian L, Lu K. Ultrahigh strength and high electrical conductivity in copper. *Science* 2004, 304, 422-426.

[29] Lu L, Chen X, Huang X, Lu K. Revealing the maximum strength in nanotwinned copper. *Science* 2009, 323, 607-610.

[30] Zhang X, Wang H, Chen XH, Lu L, Lu K, Hoagland RG, Misra A. High-strength sputter-deposited Cu foils with preferred orientation of nanoscale growth twins. *Appl. Phys. Lett.* 2006, 88, 173116.

[31] Anderoglu O, Misra A, Wang H, Ronning F, Hundley MF, Zhang X. Epitaxial nanotwinned Cu films with high strength and high conductivity. *Appl. Phys. Lett.* 2008, 93, 083108.

[32] Anderoglu O, Misra A, Ronning F, Wang H, Zhang X. Significant enhancement of the strength-to-resistivity ratio by nanotwins in epitaxial Cu films. *J. Appl. Phys.* 2009, 106, 024313.

[33] Bufford D, Wang H, Zhang X. High strength, epitaxial nanotwinned Ag films. *Acta Mater.* 2011, 59, 93-101.

[34] Ma E, Wang YM, Lu QH, Sui ML, Lu L, Lu K. Strain hardening and large tensile elongation in ultrahigh-strength NT copper. *Appl. Phys. Lett.* 2004, 85, 4932-4934.

[35] Wang G, Li G, Zhao L, Lian J, Jiang Z, Jiang Q. The origin of the ultrahigh strength and good ductility in nanotwinned copper. *Mater. Sci. Eng. A* 2010, 527, 4270-4274.

[36] Idrissi H, Wang B, Colla MS, Raskin JP. Ultrahigh strain hardening in thin Palladium films with nanoscale twins. *Advanced Mater.* 2011, 23, 2119-2122.

[37] Algra RE, Verheijen MA, Borgstrom MT, Feiner L, Immink G, Van Enckevort WJO, Vlieg E, Bakkers EPAM. Twinning superlattices in indium phosphide nanowires. *Nature* 2008, 456, 369-372.

[38] Caroff P, Dick KA, Johansson J, Messing ME, Deppert K, Samuelson L. Controlled polytypic and twin-plane superlattices in III-V nanowires. *Nature Nanotech.* 2008, 4, 50-55.

[39] Arbiol J, Estrad S, Prades JD, Cirera A, Furtmayr F, Stark C, Laufer A, Stutzmann M, Eickhoff M, Gass MH, Bleloch AL, Peir F, Morante JR. Triple-twin domains in Mg doped GaN wurtzite nanowires: structural and electronic properties of this zinc-blende-like stacking. *Nanotech.* 2009, 20, 145704.

[40] Spirkoska D, Arbiol J, Gustafsson A, Conesa-Boj S, Glas F, Zardo I, Heigoldt M, Gass MH, Bleloch AL, Estrade S, Kaniber M, Rossler J, Peiro F, Morante JR, Abstreiter G, Samuelson L, Morral1 AF. Structural and optical properties of high quality zinc-blende/wurtzite GaAs nanowire heterostructures. *Phys. Rev. B* 2009, 80, 245325.

[41] Barg AI, Rabkin E, Gust W. Faceting transformation and energy of a Σ3 grain boundary in silver. *Acta Metall. Mater.* 1995, 43, 4067-4074.

[42] Hofmeister H. Forty years study of fivefold twinned structures in small particles and twin films. *Cryst. Res. Technol.* 1998, 33, 3-25.

[43] Huang JY, Wu YK, Ye HQ. Allotropic transformation of cobalt induced by ball milling. *Acta Mater.* 1996, 44, 1201-1209.

[44] Liao XZ, Zhao YH, Srinivasan SG, Zhu YT, Valiev RZ, Gunderov V. Deformation twinning in nanocrystalline copper at room temperature and low strain rate. *Appl. Phys. Lett.* 2004, 84, 592-594.

[45] Liao XZ, Zhao YH, Zhu YT, Valiev RZ, Gunderov V. Grain-size effect on the deformation mechanisms of nanostructured copper processed by high-pressure torsion. *J. Appl. Phys.* 2004, 96, 636-640.

[46] Zhu YT, Liao XZ, Valiev RZ. Formation mechanism of fivefold deformation twins in nanocrystalline face-centered-cubic metals. *Appl. Phys. Lett.* 2005, 86, 103112.

[47] Huang P, Dai GQ, Wang D, Xu KW, Li YH. Fivefold annealing twin in nanocrystalline Cu. *Appl. Phys. Lett.* 2009, 95, 203101.

[48] Cao AJ, Wei YG. Formation of fivefold deformation twins in nanocrystalline face-centered-cubic copper based on molecular dynamics simulations. *Appl. Phys. Lett.* 2006, 89, 041919.

[49] Bringa EM, Farkas D, Caro A, Wang YM, McNaney J, Smith R. Fivefold twin formation during annealing of nanocrystalline Cu. *Scirpta Mater.* 2008, 59, 1267-1270.

[50] Wu XL, Zhu YT. Inverse grain-size effect on twinning in nanocrystalline Ni *Phys. Rev. Lett.* 2008, 101, 025503.

[51] Cheng S, Stoica AD, Wang XL, Ren Y, Almer J, Horton JA. Deformation crossover: From nano- to mesoscale *Phys. Rev. Lett.* 2009, 103, 035502.

[52] Zhang JY, Liu G, Wang RH, Li J, Sun J, Ma E. Double-inverse grain size dependence of deformation twinning in nanocrystalline Cu. *Phys. Rev. B* 2010, 81, 172104.

[53] Wang J, Li N, Anderoglu O, Zhang X, Misra A, Huang JY, Hirth JP. Detwinning mechanisms for growth twins in face-centered cubic metals. *Acta Mater.* 2010, 58, 2262-2270.

[54] Merz MD, Dahlgren SD. Tensile strength and work hardening of ultrafine-grained high-purity copper. *J. Appl. Phys.* 1975, 46, 3235-3237.

[55] Dahlgren SD, Nicholson WL, Merz MD, Bollmann W, Devlin JF, Wang R. Microstructural analysis and tensile properties of thick copper and nickel sputter deposits. *Thin Solid Films* 1977, 40, 345-353.

[56] Wang B, Fei GT, Zhou Y, Wu B, Zhu X, Zhang L. Controlled growth and phase transition of silver nanowires with dense lengthwise twins and stacking faults. *Cryst. Growth Des.* 2008, 8, 3073-3076.

[57] Bernardi M, Raja SN, Lim SK. Nanotwinned gold nanowires obtained by chemical synthesis. *Nanotech.* 2010, 21, 285607.

[58] Zhong S, Koch Y, Wang M, Scherer T, Walheim S, Hahn H, Schimmel T. Nanoscale twinned copper nanowire formation by direct electrodeposition. *Small* 2009, 20, 2265-2270.

[59] Burek MJ, Greer JR. Fabrication and microstructure control of nanoscale mechanical testing specimens via electron beam lithography and electroplating. *Nano Lett.* 2010, 10, 69-76.

[60] Jang D, Cai C, Greer JR. Influence of homogeneous interfaces on the strength of 500 nm diameter Cu nanopillars. *Nano Lett.* 2011, 11, 1743-1746.

[61] Qu S, Zhang P, Wu SD, Zang QS, Zhang ZF. Twin boundaries: Strong or weak? *Scripta Mater.* 2008, 59, 1131-1134.

[62] Hong S, Tao NR, Huang X, Lu K. Nucleation and thickening of shear bands in nano-scale twin/matrix lamellae of a Cu–Al alloy processed by dynamic plastic deformation. *Acta Mater.* 2010, 58, 3103-3116.

[63] Cao AJ, Wei YG, Mao S. Strengthening mechanisms and dislocation dynamics in twinned metal nanowires. *JOM* 2008, 60, 85-88.

[64] Zhang YF, Huang HC. Do twin boundaries always strengthen metal nanowires? *Nanoscale Res. Lett.* 2009, 4, 34-38.

[65] Deng C, Sansoz F. Enabling Ultrahigh plastic flow and work hardening in twinned gold nanowires. *Nano Lett.* 2009, 9, 1517-1522.

[66] Deng C, Sansoz F. Fundamental differences in the plasticity of periodically twinned nanowires in Au, Ag, Al, Cu, Pb and Ni. *Acta Mater.* 2009, 57, 6090-6101.

[67] Deng C, Sansoz F. Near-ideal strength in gold nanowires achieved through microstructural design. *ACS Nano* 2009, 3, 3001-3008.

[68] Deng C, Sansoz F. Size-dependent yield stress in twinned gold nanowires mediated by site-specific surface dislocation emission. *Appl. Phys. Lett.* 2009, 95, 091914.

[69] Deng C, Sansoz F. Effects of twin and surface facet on strain-rate sensitivity of gold nanowires at different temperatures. *Phys. Rev. B* 2010, 81 155430.

[70] Deng C, Sansoz F. Repulsive force of twin boundary on curved dislocations and its role on the yielding of twinned nanowires. *Scripta Mater.* 2010, 63, 50-53.

[71] Guo X, Xia YZ. Repulsive force vs. source number: Competing mechanisms in the yield of twinned gold nanowires of finite length. *Acta Mater.* 2011, 59, 2350-2357.

[72] Zhai YT, Gong XG. Understanding periodically twinned structure in nano-wires. *Phys. Lett. A* 2011, 375, 1889-1892.

[73] Afanasyev KA, Sansoz F. Strengthening in gold nanopillars with nanoscale twins. *Nano Lett.* 2007, 7, 2056-2062.

[74] Brown JA, Ghoniem NM. Reversible-irreversible plasticity transition in twinned copper nanopillars. *Acta Mater.* 2010, 58, 866-894.

[75] Li X, Wei Y, Lu L, Lu K, Gao H. Dislocation nucleation governed softening and maximum strength in NT metals. *Nature* 2010, 464, 877-880.

[76] Stukowski A, Albe K, Farkas D. Nanotwinned fcc metals: Strengthening versus softening mechanisms. *Phys. Rev. B* 2010, 82, 224103.

[77] Koch CC. Optimization of strength and ductility in nanocrystalline and ultrafine grained metals. *Scripta Mater.* 2003, 49, 657-662.

[78] Lu L, Schwaiger R, Shan ZW, Dao M, Lu K, Suresh S. Nano-sized twins induce high rate sensitivity of flow stress in pure copper. *Acta Mater.* 2005, 53, 2169-2179.

[79] Lu L, Dao M, Zhu T, Li J. Size dependence of rate-controlling deformation mechanisms in nanotwinned copper. *Scripta Mater.* 2009, 60, 1062-1066.

[80] Qin EW, Lu L, Tao NR, Lu K. Enhanced fracture toughness of bulk nanocrystalline Cu with embedded nanoscale twins. *Scripta Mater.* 2009, 60, 539-542.

[81] Qin EW, Lu L, Tao NR, J. Tan J, K. Lu K. Enhanced fracture toughness and strength in bulk nanocrystalline Cu with nanoscale twin bundles. *Acta Mater.* 2009, 57, 6215-6225.

[82] Singh A, Tang L, Dao M, Lu L, Suresh S. Fracture toughness and fatigue crack growth characteristics of nanotwinned copper. *Acta Mater.* 2011, 59, 2437-2446.

[83] Shute CJ, Myer BD, Xie S, Li SY, Barbee TW, Hodge AM, Weertman JR. Detwinning, damage and crack initiation during cyclic loading of Cu samples containing aligned nanotwins. *Acta Mater.* 2011, 59 4569-4577.

[84] Dao M, Lu L, Shen YF, Suresh S. Strength, strain-rate sensitivity and ductility of copper with nanoscale twins. *Acta Mater.* 2006, 54, 5421-5432.

[85] Jerusalem A, Dao M, Suresh S, Radovitzky R. Three-dimensional model of strength and ductility of polycrystalline copper containing nanoscale twins. *Acta Mater.* 2008, 56, 4647-4657.

[86] Shen F, Zhou J, Liu Y, Zhu R, Zhang S, Wang Y. Deformation twinning mechanism and its effects on the mechanical behaviors of ultrafine grained and nanocrystalline copper. *Comp. Mater. Sci.* 2010, 49, 226-235.

[87] Wu B, Zou N, Tan J, Wang J, Pang M, Hu D. Numerical simulation on size effect of copper with nano-scale twins. *Trans. Nonferrous Met. Soc. China* 2011, 21, 364-370.

[88] Cao AJ, Wei YG. Molecular dynamics simulation of plastic deformation of nanotwinned copper. *J. Appl. Phys.* 2007, 102, 083511.

[89] Shabib I, Miller RE. A molecular dynamics study of twin width, grain size and temperature effects on the toughness of 2D-columnar nanotwinned copper. *Modelling Simul. Mater. Sci. Eng.* 2009, 17, 055009.

[90] Shabib I, Miller RE. Deformation characteristics and stress-strain response of nanotwinned copper via molecular dynamics simulation. *Acta Mater.* 2009, 57, 4364-4373.

[91] Qu S, Zhou H. Atomistic mechanisms of microstructure evolution in nanotwinned polycrystals. *Scripta Mater.* 2011, 65, 265-268.

[92] Qu S, Zhou H, Huang Z. Shear band initiation induced by slip-twin boundary interactions. *Scripta Mater.* 2011, 65, 715-718.

[93] Froseth AG, Derlet PM, Van Swygenhoven H. Grown-in twin boundaries affecting deformation mechanisms in nc-metals. *Appl. Phys. Lett.* 2004, 85, 5863-5866.

[94] Froseth AG, Van Swygenhoven H, Derlet PM. The influence of twins on the mechanical properties of nc-Al. *Acta Mater.* 2004, 52, 2259-2268.

[95] Li L, Ghoniem NM. Twin-size effects on the deformation of nanotwinned copper. *Phys. Rev. B* 2009, 79, 075444.

[96] Kulkarni Y, Asaro RJ. Are some nanotwinned fcc metals optimal for strength, ductility and grain stability? *Acta Mater.* 2009, 57, 4835-4844.

[97] Kulkarni Y, Asaro RJ, Farkas D. Are nanotwinned structures in fcc metals optimal for strength, ductility and grain stability? *Scripta Mater.* 2009, 60, 532-535.

[98] Yue L, Zhang H, Li DY. Defect generation in NT, nano-grained and single crystal Cu systems caused by wear: A molecular dynamics study. *Scripta Mater.* 2010, 63, 1116-119.

[99] Qu S, Zhou H. Hardening by twin boundary during nanoindentation in nanocrystals. *Nanotech.* 2010, 21, 335704.

[100] Zhu T, Li J, Samanta A, Kim HG, Suresh S. Interfacial plasticity governs strain rate sensitivity and ductility in nanostructured metals. *Proc. Natl. Acad. Sci. USA* 2007, 104, 3031-3036.

[101] Chen Z, Jin Z, Gao H. Repulsive force between screw dislocation and coherent twin boundary in aluminum and copper. *Phys. Rev. B* 2007, 75, 212104.

[102] Wu ZX, Zhang YW, Srolovitz DJ. Dislocation-twin interaction mechanisms for ultrahigh strength and ductility in nanotwinned metals. *Acta Mater.* 2009, 57, 4508-4518.

[103] Zheng YG, Lu J, Zhang HW, Chen Z. Strengthening and toughening by interface-mediated slip transfer reaction in nanotwinned copper. *Scripta Mater.* 2009, 60, 508-511.

[104] Hu Q, Li L, Ghoniem NM. Stick-slip dynamics of coherent twin boundaries in copper. *Acta Mater.* 2009, 57, 4866-4873.

[105] Jin ZH, Gumbsch P, Ma E, Albe K, Lu K, Hahn H, Gleiter H. The interaction mechanism of screw dislocations with coherent twin boundaries in different face-centred cubic metals. *Scripta Mater.* 2006, 54, 1163-1168.

[106] Jin ZH, Gumbsch P, Albe K, Ma E, Lu K, Gleiter H, Hahn H. Interactions between non-screw lattice dislocations and coherent twin boundaries in face-centered cubic metals. *Acta Mater.* 2008, 56, 1126-1135.

[107] Ezaz T, Sangid MD, Sehitoglu H. Energy barriers associated with slip-twin interactions. *Phil. Mag.* 2011, 91, 1464-1488.

[108] Chassagne M, Legros M, Rodeny D. Atomic-scale simulation of screw dislocation/coherent twin boundary interaction in Al, Au, Cu and Ni. *Acta Mater.* 2011, 59, 1456-1463.

[109] Sleeswyk AW, Verbraak CA. Incorporation of slip dislocations in mechanical twins-I. *Acta Metall.* 1961, 9, 917-927.

[110] Mahajan S, Chin GY. Twin-slip, twin-twin and slip-twin interactions in Co-8wt.% Fe alloy single crystals. *Acta Metall. Mater.* 1973, 21, 173-179.

[111] Hartley CS, Blachon DLA. Reactions of slip dislocations at coherent twin boundaries in face-centered-cubic metals. *J. Appl. Phys.* 1978, 49, 4788-4796.

[112] Remy L. The interaction between slip and twinning systems and the influence of twinning on the mechanical behavior of fcc metals and alloys. *Metall. Mater. Trans. A* 1981, 12, 387-408.

[113] Wang YB, Sui ML. Atomic-scale in situ observation of lattice dislocations passing through twin boundaries. *Appl. Phys. Lett.* 2009, 94, 021909.

[114] Zhu YT, Wu XL, Liao XZ, Narayan J, Kecskes LJ, Mathaudhu SN. Dislocation-twin interactions in nanocrystalline fcc metals. *Acta Mater.* 2011, 59, 812-821.

[115] Wang YB, Wu B, Sui ML. Dynamical dislocation emission processes from twin boundaries. *Appl. Phys. Lett.* 2008, 93, 041906.

[116] Konopka K, Mizera J, Wyrzykowski JW. The generation of dislocations from twin boundaries and its effect upon the flow stresses in FCC metals. *J. Mater. Process. Technol.* 2000, 99, 255-259.

[117] Sennour M, Korinek SL, Champion Y, Hÿtch MJ. HRTEM study of defects in twin boundaries of ultra-fine grained copper. *Philos. Mag.* 2007, 87, 1465-1486.

[118] Li N, Wang J, Misra A, Zhang X, Huang JY, Lu, K. Twinning dislocation multiplication at a coherent twin boundary. *Acta Mater.* 2011, 59, 5989-5996.

[119] http://en.wikipedia.org/wiki/Molecular_dynamics.

[120] Car R, Parrinello M. Unified approach for molecular dynamics and density-functional theory. *Phys. Rev. Lett.* 1985, 55, 2471-2474.

[121] Wolf D, Yamakov V, Phillpot SR, Mukherjee A, Gleiter H. Deformation of nanocrystalline materials by molecular-dynamics simulation: relationship to experiments? *Acta Mater.* 2005, 53, 1-40.

[122] Raffi-Tabar H, Mansoori GA. Interatomic potential models for nanostructures. In "Encyclopedia of nanoscience and nanotechnology", edited by Nalwa HS. American Scientific Publishers, 2003.

[123] Daw MS, Baskes MI. Embedded-atom method: Derivation and application to impurities, surfaces and other defects in metals. *Phys. Rev B* 1984, 29, 6443-6453.

[124] Mishin Y, Mehl M, Papaconstantopoulos D, Voter A, Kress J Structural stability and lattice defects in copper: Ab initio, tight-binding, and embedded-atom calculations. *Phys. Rev. B* 2001, 63, 224106.

[125] Finis MW, Siniclair JE. A simple empirical N-body potential for transition-metals. *Phil. Mag. A* 1984, 50, 45-55.

[126] Sutton AP, Chen. Long-range Finnis-Sinlair potentials. *Phil. Mag. Lett.* 1990, 61, 139-146.

[127] Eggen BR, Johnston RL, Li S, Murrel JN. Potential energy functions for atomic solids. IV. Reproducing the properties of more than one solid phase. *Mol. Phys.* 1992, 76, 619-633.

[128] Tuckerman M, Berne BJ, Martyna GJ. Reversible multiple time scale molecular dynamics. *J. Chem. Phys.* 1992, 97, 1990-2001.

[129] Zhou RH, Berne BJ. A new molecular dynamics method combining the reference system propagator algorithm with a fast multipole method for simulating proteins and other complex systems. *J. Chem. Phys.* 1995, 103, 9444-9459.

[130] Humphreys DD, Friesner RA, Berne BJ. A multiple time step molecular dynamics algorithm for Macromolecules. *J. Phys. Chem.* 1994, 98, 6885-6892.

[131] Watanabe M, Karplus M. Simulation of macromolecules by multiple time-step methods. *J. Phys. Chem.* 1995, 99, 5680-5697.

[132] Procacci P, Marchi M. Taming the Ewald sum in molecular dynamics simulations of solvated proteins via a multiple time step algorithm. *J. Chem. Phys.* 1996, 104, 3003-3012.

[133] Rivera JL, McCabe C, Cummings PT. The oscillatory damped behaviour of incommensurate double-walled carbon nanotubes. *Nanotech.* 2005, 16, 186-198.

[134] Makeev MA, Kalia RK, Nakano A, Vashishta P, Madhukar A. Effect of geometry on stress relaxation in InAs/GaAs rectangular nanomesas: Multimillion-atom molecular dynamics simulations. *J. Appl. Phys.* 2005, 94, 114313.

[135] Li XF, Wang LL, Chen KQ, Luo Y. Nanomechanically induced molecular conductance switch. *Appl. Phys. Lett.* 2009, 95, 232118.

[136] Perrona A, Garrucheta S, Politanoa O, Aralb G, Vignala V. Oxidation of nanocrystalline aluminum by variable charge molecular dynamics. *J. Phys. Chem. Solids* 2010, 71, 119-124.

[137] Reich S. Multiple time scales in classical and quantum-classical molecular dynamics. *J. Comp. Phys.* 1999, 151, 49-73.

[138] http://en.wikipedia.org/wiki/Molecular_dynamics.

[139] Berendsen HJC, Postma JPM, Gunstern WF, DiNola A, Haak JR. Molecular dynamics with coupling to an external bath. *J. Chem. Phys.* 1984, 81, 3684-3690.

[140] Nose S. A unified formulation of the constant temperature molecular dynamics methods. *J. Chem. Phys.* 1984, 81, 511-519.

[141] Hoover WG. Canonical dynamics: Equilibrium phase-space distributions. *Phys. Rev. A* 1985, 31, 1695-1697.

[142] Esfarjani K, Mansoori GA. Statistical mechanical modeling and its application to aanosystems. In “Handbook of theoretical and computational nanotechnology”, edited by Rieth MR, Shommers W. American Scientific Publishers, 2005.

[143] Andersen, HC. Molecular dynamics simulations at constant pressure and/or temperature. *J. Chem. Phys.* 1980, 72, 2384-2393.

[144] Parrinello M, Rahman A. Polymorphic transitions in single crystals: A new molecular dynamics method. *J. Appl. Phys.* 1981, 52, 7182-7190.

[145] Trobec R, Jerebic I, Janezic D. Parallel algorithms for molecular dynamics integration. *Parallel Comp.* 1993, 19, 1029-1039.

[146] Smith W, Forester T R. Parallel Macromolecular simulations and the replicated data strategy. *Comp. Phys. Commun.* 1994; 79, 52-62.

[147] Plimpton S, Hendrickson B. A new parallel method for molecular dynamics simulation of macromolecular systems. *J. Comp. Chem.* 1996, 17, 326-335.

[148] Wang B, Shu J W, Chen M, et al. Optimization techniques for parallel force-decomposition algorithm in molecular dynamic simulations. *Comp. Phys. Commun.* 2003, 154, 121-130.

[149] Brown D, Clarke J H R, Okuda M, et al. A domain decomposition strategy for molecular dynamics simulations on distributed memory machines. *Comp. Phys. Commun.* 1993, 74, 67-80.

[150] Koradi R., Billeter M, Guntert P. Point-centered domain decomposition for parallel molecular dynamics simulation. *J. Comp. Phys.* 2000, 124, 139-147.

[151] Li X, Wei Y, Yang W, Gao H. Competing grain-boundary- and dislocation-mediated mechanisms in plastic strain recovery in nanocrystalline aluminum. *Proc. Natl. Acad. Sci. USA* 2009, 106, 16108-16113.

[152] Allen MP, Tildesley DJ. Computer simulation of liquid. Oxford, Clarendon Press, 1987.

[153] Schiotz J, Vegge T, DiTolla F D, Jacobsen KW. Atomic-scale simulations of the mechanical deformation of nanocrystalline metals. *Phys. Rev. B* 1999, 60, 11971.

[154] Kelchner CL, Plimpton SJ, Hamilton JC. Dislocation nucleation and defect structure during surface indentation. *Phys. Rev. B* 1998, 58, 11085-11088.

[155] Jonsson H, Andersen H. Icosahedral ordering in the Lennard-Jones liquid and glass. *Phys. Rev. Lett.* 1988, 60, 2295-2298.

[156] Van Swygenhoven H, Farkas D, Caro A. Grain-boundary structures in polycrystalline metals at the nanoscale. *Phys. Rev. B* 2000, 62, 831-838.

[157] Zimmerman JA, Kelchner CL, Klein PA, Hamilton JC, Foiles SM. Surface step effects on nanoindentation. *Phys. Rev. Lett.* 2001, 87, 165507.

[158] Bulatov V, Cai W. Nodal effects in dislocation mobility. *Phys. Rev. Lett.* 2002, 89, 115501.

[159] Li J, Ngan AHW, Gumbsch P. Atomistic modeling of mechanical behavior. *Acta Mater.* 2003, 51, 5711-5742.

[160] http://en.wikipedia.org/wiki/High-performance_computing.

[161] Zhu T, Li J. Ultra-strength materials. *Prog. Mater. Sci.* 2010, 55, 710-757.

[162] Uchic MD, Dimiduk DM, Florando JN, Nix WD. Sample Dimensions Influence Strength and Crystal Plasticity. *Science* 2004, 305, 986-989.

[163] Greer JR, Oliver WC, Nix WD. Size dependence of mechanical properties of gold at the micron scale in the absence of strain gradients. *Acta Mater.* 2005, 53, 1821-1830.

[164] Shan ZW, Mishra RK, Syed Asif SA, Warren OL, Minor AM. Mechanical annealing and source-limited deformation in submicrometre-diameter Ni crystals. *Nature Mater.* 2007, 7, 115-119.

[165] Hemker KJ, Nix WD. Nanoscale deformation: Seeing is believing. *Nature Mater.* 2008, 7, 97-98.

[166] Wang YB, Sui ML, Ma E. In situ observation of twin boundary migration in copper with nanoscale twins during tensile deformation. *Phil. Mag. Lett.* 2007, 87, 935-942.

[167] Bulatov VV, Hsiung LL, Tang M, Arsenlis A, Bartelt MC, Cai W, Florando JN, Hiratani M, Rhee M, Hommes G, Pierce TG, Rubia TD. Dislocation multi-junctions and strain hardening. *Nature* 2006, 440, 1174-1178.

[168] Xu L, Xu D, Tu KN, Cai Y, Wang N, Dixit P, Pang HL, Miao J. Structure and migration of (112) step on (111) twin boundaries in nanocrystalline copper. *J. Appl. Phys.* 2008, 104,113717.

[169] Zhu T, Li J, Samanta A, Leach A, Gall K. Temperature and strain-rate dependence of surface dislocation nucleation. *Phys. Rev. Lett.* 2008, 100, 025502.

[170] Asaro, R. J. & Suresh, S. Mechanistic models for the activation volume and rate sensitivity in metals with nanocrystalline grains and nano-scale twins. *Acta Mater.* 53, 3369-3382 (2005).

[171] Mirkhani H, Joshi SP. Crystal plasticity of nanotwinned microstructures: A discrete twin approach for copper. *Acta Mater.* 2011, 59, 5603-5617.

[172] Wei Y. The kinetics and energetics of dislocation mediated de-twinning in NT face-centered cubic metals. *Mater. Sci. Eng. A* 2011, 528, 1558-1566.

[173] Wei Y. Scaling of maximum strength with grain size in nanotwinned fcc metals. *Phys. Rev. B* 2011, 83, 132104.

[174] You Z, Lu L, Lu K. Tensile behavior of columnar grained Cu with preferentially oriented nanoscale twins. *Acta Mater.* 2011, 59, 6927-6937.

[175] You Z, Li X, Gui L, Lu Q, Zhu T, Gao H, Lu L. Switchable deformation mechanisms in columnar-grained nanotwinned metals. *Under Preparation* 2011.

[176] Bunge HJ, Roberts WT. Orientation distribution, elastic and plastic anisotropy in stabilized steel sheet. *J. Appl. Cryst.* 1969, 2, 116-128.

[177] Bate P, Roberts WT, Wilson DV. The plastic anisotropy of two-phase aluminium alloys-I. Anisotropy in unidirectional deformation. *Acta Metall.* 1981, 29, 1797-1814.

[178] Kocks UF, Franciosi P, Kawai M. A forest model of latent hardening and its application to polycrystal deformation. *Text. Microstruct.* 1991, 14-18, 1103-1114.

[179] Hansen N, Jensen DJ. Flow stress anisotropy caused by geometrically necessary boundaries. *Acta Metall. Mater.* 1992, 40, 3265-3275.

[180] Winther G, Jensen DJ, Hansen N. Modelling flow stress anisotropy caused by deformation induced dislocation boundaries. *Acta Mater.* 1997, 45, 2455-2465.

[181] Kim YW. Ordered intermetallic alloys, part III: gamma titanium aluminides. *JOM* 1994, 47, 30-39.

[182] Appel F, Wagner R. Microstructure and deformation of two-phase γ-titanium aluminides. *Mater. Sci. Eng. R* 1998, 22, 187-268.

[183] Kim YW. Strength and ductility in TiAl alloys. *Intermetallics* 1998, 6, 623-628.

[184] Yao KF, Inui H, Kishida K, Yamaguchi M. Plastic deformation of V- and Zr-alloyed PST TiAl in tension and compression at room temperature. *Acta Metal. Mater.* 1995, 43, 1075-1086.

[185] Umkoshi Y, Yasuda HY, Nakano T. Plastic anisotropy and fatigue of TiAl PST crystals: a review. *Intermetallics* 1996, 4, S65-S75.

[186] Umeda H, Kishida K, Inui H, Yamaguchi M. Effects of Al-concentration and lamellar spacing on the room-temperature strength and ductility of PST crystals of TiAl. *Mater. Sci. Eng. A* 1997, 239, 336-343.

[187] Parthasarathy TA, Mendiratta MG, Dimiduk DM. Strength Flow behavior of PST and fully lamellar polycrystals of Ti-48Al in the microstrain regime. *Acta Mater.* 1998, 46, 4005-4016.

[188] Parthasarathy TA, Subramanian PR, Mendiratta MG, Dimiduk DM. Phenomenological observations of lamellar orientation effects on the creep behavior of Ti-48at%Al PST crystals. *Acta Mater.* 2000, 48, 541-551.

[189] Taylor GI. Plastic strain in metals. *J. Inst. Metals* 1938, 62, 307-325.

[190] Field DP, True BW, Lillo TM, Flinn JE. Observation of twin boundary migration in copper during deformation. *Mater. Sci. Eng. A* 2004, 372, 173-179.

[191] Nix, W. Mechanical properties of thin films. *Metall. Mater. Trans. A* 1989, 20, 2217-2245.

[192] Misra A, Hirth JP, Hoagland RG. Length-scale-dependent deformation mechanisms in incoherent metallic multilayered composites. *Acta Mater.* 2005, 53, 4817-4824.

[193] Shan ZW, Lu L, Minor AM, Stach EA, Mao SX. The effect of twin plane spacing on the deformation of copper containing a high density of growth twins. *JOM* 2008, 60, 71-74.

[194] Zhou H, Qu S, Yang W. Toughening by nano-scaled twin boundaries in nanocrystals. *Modelling Simul. Mater. Sci. Eng.* 2010, 18, 065002.

[195] Zhou H, Qu S. The effect of nanoscale twin boundaries on fracture toughness in nanocrystalline Ni. *Nanotech.* 2010, 21, 035706.

[196] Kim S, Li X, Gao H, Kumar S. In-situ observations of crack arrest and bridging by nanoscale twins in Copper thin foils. *Under submission* 2011.

[197] Anderoglu O, Misra A, Wang J, Hoagland RG, Hirth JP, Zhang X. Plastic flow stability of nanotwinned Cu foils. *Inter. J. Plasticity* 2010, 26, 875-886.

[198] Budiansky B, Amazigo JC, Evans AG. Small-scale crack bridging and the fracture toughness of particulate-reinforced ceramics. *J. Mech. Phys. Solids* 1988, 36, 167-187.

[199] Nalla RK, Kinney JH, Ritchie RO. Mechanistic fracture criteria for the failure of human cortical bone. *Nature Mater.* 2003, 2, 164-168.

[200] Cox BN, Marshall DB. Concepts for bridged cracks in fracture and fatigue. *Acta Metall. Mater.* 1994, 42, 341-363.

[201] Bannister M, Shercliff H, Bao G, Zok F, Ashby MF (1992) Toughening in brittle systems by ductile bridging ligaments. *Acta Metall. Mater.* 1992, 40, 1531-1537.

[202] Keller RR, Phelps JM, Read DT. Tensile and fracture behavior of free-standing copper films. *Mater. Sci. Eng. A* 1996, 214, 42-52.

[203] Rogers HC. The tensile fracture of ductile metals. *Trans. Met. Soc. AIME* 1960, 218, 498-506.

[204] Ovid'ko IA, Sheinerman AG. Triple junction nanocracks in deformed nanocrystalline materials. *Acta Mater.* 2004, 52, 1201-1209.

[205] Jang DC, Li X, Gao H, Greer JR. Nanotwinned nanopillars: fabrication and deformation mechanisms. *Under submission* 2011.

[206] Zhang H, Schuster BE,Wei Q, Ramesh KT. The design of accurate micro-compression experiments. *Scripta Mater.* 2006, 54, 181-186.

[207] Ogata S, Li J, Yip S. Ideal pure shear strength of aluminum and copper. *Science* 2002, 298, 807-811.

[208] Jennings AT, Greer JR. Tensile deformation of electroplated copper nanopillars. *Phil. Mag.* 2011, 91, 1108-1120.

[209] Meyers, MA, Chawla KK. Mechanical behavior of materials. Prentice-Hall Inc., NewJersey, 1998, 1st edn.

[210] Hong C, Tao N, Huang X, Lu K. Nucleation and thickening of shear bands in nano-scale twin/matrix lamellae of a CuAl alloy processed by dynamic plastic deformation. *Acta Mater*. 2010, 58, 3103-3116.

[211] Wei Y. Anisotropic size effect in strength in coherent nanowires with tilted twins. *Phys. Rev. B* 2011, 84, 014107.